TAMPEREEN TEKNILLINEN YLIOPISTO
TAMPERE UNIVERSITY OF TECHNOLOGY

MAIJA RAUNIO

APPLICATION AND VALIDATION OF A NEW APPROACH FOR NOTCHED BAR CREEP TESTING OF NUCLEAR WASTE DISPOSAL CANISTER COPPER

Master of Science Thesis

Supervisor: Professor Helge Lemmetyinen
Supervisor and subject approved by the Chemistry and Biotechnology Council on 14 August 2013.

TIIVISTELMÄ

TAMPEREEN TEKNILLINEN YLIOPISTO
Materiaalitekniikan koulutusohjelma
RAUNIO, MAIJA: Application and validation of a new approach for notched bar creep testing of nuclear waste disposal canister copper
Diplomityö, 81 sivua, 9 liitesivua
Elokuu 2013
Pääaine: Materiaalikemia
Tarkastaja: professori Helge Lemmetyinen
Avainsanat: Ydinjätteen loppusijoitus, kuparikapseli, virumistestaus, Cu-OFP, moniaksiaalisuus, lovettu testisauva.

Aika ydinjätteen loppusijoittamiselle lähestyy. Suomalaisten ja ruotsalaisten konsepti loppusijoitukselle on seuraava: ydinjäte säilötään valurautaiseen lieriöön, joka suljetaan kuparikapselin sisälle, ja säilötty jäte sijoitetaan 400- 500 metrin syvyyteen peruskallioon. Kuparikapselin (valmistettu Cu-OFP:sta) tehtävä on suojella sen sisällä olevaa ydinjätettä pohjaveden ym. komponenttien korrodoivalta vaikutukselta. Kapseli altistuu peruskallion sisällä sekä hydrostaattiselle paineelle että radioaktiivisen hajoamisen synnyttämälle lämmölle, minkä seurauksena kapseli viruu. Jotta kapseli saadaan tarpeeksi turvalliseksi, on kuparikapselin virumisominaisuudet selvitettävä virumiskokein. Jos kupariset virumistestisauvat altistuvat ennen virumiskoetta mekaaniselle rasitukselle, kupariin kohdistuu kylmämuokkausta, mikä vaikuttaa saataviin virumistuloksiin. Tästä syystä olisi tärkeää, että testinäytteisiin kohdistuu mahdollisimman vähän kylmämuokkausta ennen testausta. Tässä työssä tutkitaan mahdollisuutta ottaa käyttöön moniaksiaaliseen testaukseen uusi testisauva, joka valmistetaan lankasahauksella, jolloin kylmämuokkauksen määrä olisi minimissään. Uusi sauvageometria sisältää neliönmuotoisen kaksoislovetun sauvan, jonka nettopoikkipinnat ovat kahdeksankulmion muotoiset, normaalin sorvaamalla valmistetun pyöreän kaksoislovetun sauvan sijasta. Tutkimuksen idea on selvittää, kuinka uusi geometria toimii moniaksiaalisessa virumistestauksessa ja ovatko tulokset realistisempia, jos kylmämuokkausta ei olisi tapahtunut.

Työ jakautuu kahteen osaan. Kirjallisuusosiossa keskitytään Cu-OFP:n virumisominaisuuksiin ja käydään läpi eri virumistestausmenetelmiä tutkimalla yksi- ja moniaksiaalisen virumisen ominaisuuksia sekä virumismallinnuksen perusteita. Tutkimuksessa käsitellään myös sulfaattipitoisen pohjaveden vaikutus moniaksiaalisiin virumisominaisuuksiin. Kokeellisessa osiossa suoritetaan kymmenen moniaksiaalisista virumiskoetta, joista neljä suoritetaan uudella neliö sauvalla ja kuusi sorvaamalla valmistetulla pyöreällä sauvalla. FE analyysi sekä testauksen jälkeinen metallurginen arviointi suoritetaan lopuksi testisauvoille, jotta saadaan perusteellisempi käsitys sauvan käyttäytymisestä. FEM:n avulla määritetään myös sekä pyöreän että neliösauvan rankapiste ja vastaavat rankajännitykset.

Tutkimus osoittaa, että kylmätyöstöä havaitaan neliösauvoissa vähemmän kuin pyöreissä sauvoissa, jos ollenkaan. Neliösauvatestejä tarvitaan lisää, jotta realistinen ja luotettava johtopäätös voidaan tehdä. Saadut tulokset näyttävät noudattavan hyvin tehtyjä ennusteita materiaalin virumiskäyttäytymisestä. Terävästi lovettujen sauvojen rankapisteiden määritys on haasteellista, mutta suuntaa-antava rankapistealue saatiin silti määritettyä. Tulevaisuudessa pyöreä sauvageometria, joka olisi valmistettu lankasahauksella, voisi olla hyvä ratkaisu moniaksiaaliseen virumistestaukseen.

ABSTRACT

TAMPERE UNIVERSITY OF TECHNOLOGY
Master's Degree Programme in Material Technology
RAUNIO, MAIJA: Application and validation of a new approach for notched bar creep testing of nuclear waste disposal canister copper
Master of Science Thesis, 81 pages, 9 Appendix pages
August 2013
Major: Material Chemistry
Supervisor: Professor Helge Lemmetyinen
Keywords: Nuclear waste disposal, disposal canister, creep testing, multiaxiality, notched bar, Cu-OFP.

Time for the disposal of the nuclear waste is shortly at hand. The concept for the disposal in Finland and Sweden is to store the nuclear waste deep into the bedrock for at least 100 000 years. The nuclear waste is first inserted to a cast iron canister and then the package is sealed inside a copper canister (made of oxygen free phosphorus doped copper Cu-OFP), main function of which is to protect the inner parts from corrosion caused by the groundwater. The copper canister will be subjected to hydrostatic pressure inside the bedrock, and therefore creep to some extent. To see how the copper canister behaves in the repository, multiaxial creep testing to Cu-OFP must be done. To get as realistic results as possible, the creep testing specimens shouldn't experience cold work before the actual testing. This thesis examines the possibility to use a new testing bar geometry manufactured by wire-erosion to minimize the amount of cold work, usually caused by specimen preparation (for example milling). The new testing approach involves a square shaped bar, which has circumferentially two sharp octagon shaped notches. The square bar is made by wire-erosion instead of the earlier used double notched round bar made by turn-milling. The main goal is to find out, how the new geometry suits for multiaxial creep testing and whether the results are more realistic if the effect of cold work could be minimized.

The thesis is divided into two parts. In the literature study part, issues related to creep properties of Cu-OFP are explored. Theory related to the creep testing methodologies is discussed: mainly uniaxial and multiaxial creep properties as well as creep modelling issues are being studied. Also the effects of sulphide rich groundwater on the creep properties of Cu-OFP are investigated. In the experimental research part, ten multiaxial Cu-OFP creep tests were performed from which four specimens were manufactured according to the new square geometry. The other six tests were carried out with the round geometry manufactured by turn-milling. FE analysis and post metallurgical evaluation is added in the end to get a better view of the processes taking place inside the specimen. Also the determination of skeletal point and corresponding skeletal stresses for square and round geometry is made by FEM.

The study indicates that the amount of cold work in square specimens seems to be lower than in the round specimens or non-existent. However, more tests by square specimens are needed for the final validation. The creep results seem to behave as the creep behaviour models predict. The determination of skeletal point for sharp notches is challenging, but a suitably small skeletal zone was possible to define. In the future a round geometry made completely by wire-erosion could be a good choice for multiaxial creep testing.

PREFACE

This Master of Science Thesis is a part of VTT research concerning the nuclear waste disposal (the KYT-programme). I would like to thank Helge Lemmetyinen, the thesis supervisor, and all the co-workers in VTT, especially Juhani Rantala, who acted as a thesis instructor in VTT. Many questions were answered and help was always given when needed. I would also like to thank Pertti Auerkari, Stefan Holmström, Rami Pohja, Sanni Yli-Olli, Satu Tuurna, Anssi Laukkanen, and Tom Andersson for their expertise and help with the thesis work. The general pleasant working atmosphere and attitude in VTT made the working very enjoyable. VTT offered also good facilities for making the thesis and the needed creep tests.

CONTENTS

TERMS AND DEFINITIONS

A	Dimensionless factor (in extended Norton law)
A	Area of the specimen cross section
A'	Characterise the shape of the uniaxial creep rupture curve
a	Radius of the specimen at the base of the notch position
a	Constant (in normalised skeletal stress conversion equations)
A_f	Minimum cross-sectional area after rupture across the notch throat
A_0	Original cross-sectional area across notch throat
B	Material constant (in Norton creep)
b	Burgers vector
b	Constant (in normalised skeletal stress conversion equations)
BM	Base material
BWR	Boiling water reactor
C	Constant (in MHG parameter)
C	Material constant (in Larson-Miller parameter)
C	Fitting factor (in LCSP model)
c	Constant (in normalised skeletal stress conversion equations)
CT	Compact tension
Cu-OF	Oxygen-free high conductivity copper
Cu-OFP	Oxygen-free phosphorous doped copper
D	Diameter of parallel portion of a notched testpiece of the circular cross-section
D	Diffusion coefficient (in extended Norton law)
d	Grain size
d_{no}	Initial diameter of the testpiece at notch plane (throat)
d_{no}/r_{no}	Notch acuity ratio
E	Elastic modulus
EBW	Electron beam welding
EDM	Electric discharge machining
EDS	Energy Dispersive X-ray Spectroscopy
FEM	Finite element method
FeS_2	Pyrite
FSW	Friction stir welding
$F(T,\sigma,\varepsilon)$	Multi-linear combination of temperature T, stress σ and strain ε (in MHG model)
Gy/h	Gray per hour (SI unit of absorbed radiation)

H	Ratio of maximum principal stress to the von Mises equivalent stress
h	Constraint parameter
HCO_3	Hydrogen carbonate
HS^-	Hydrogen sulphide
H.T. creep	High temperature creep
HV5	Vickers hardness scale 5N
IRB	Iron reducing bacteria
K	Material constant in the Monkman-Grant relationship
k	Boltzmann's constant
k	Constant obtained from the test data (in the Wilshire equations)
k_1 and k_2	Functions of time to strain (in LCSP model)
KBS-3	Swedish concept for nuclear waste disposal
L_{eo}	Original extensometer gauge length
L_{eu}	Final extensometer gauge length
LCSP	Logistic creep strain prediction model
LOM	Light optical microscopy
L.T. creep	Low temperature creep
MHG	Manson-Haferd-Grounes model
MOB	Methane oxidizing bacteria
MRB	Manganese reducing bacteria
n	Creep exponent
n	Number of data points (in Z-factor)
NB	Notched bar
NH_4^+	Ammonium ion
NO_2^-	Nitrite
OFHC	Oxygen-free high conductivity copper
OP-S	Colloidal silica suspension
P	Larson-Miller parameter
p	Fitting factor (in LCSP model)
p	Exponent for grain size dependence
ppm	Parts per million
PWR	Pressurized water reactor
Q_c	Activation energy of creep
Q_c*	Apparent activation energy of creep
R	Molar gas constant
CEEQ	Equivalent creep strain
r	Material constant in the Monkman-Grant relationship
r	Radial co-ordinate at notch plane
r_{no}	Initial notch root radius
RGW	Reference ground water

SCC	Stress corrosion cracking
SRF	Strength reduction factor
SEM	Scanning electron microscopy
SKB	Swedish Nuclear Fuel and Waste Management Co
SKI	Swedish nuclear power inspectorate
SO_4^{2-}	Sulfate ion
SRB	Sulphate reducing bacteria
T_m	Melting temperature
t_ε	Time to strain
t_r	Time to rupture
u	Constant obtained from the test data (in the Wilshire equations)
μ	Material constant
v'	Characterise the shape of the uniaxial creep rupture curve
VTT	Technical research centre of Finland
VVER-440	Russian version of PWR
WE-model	Wilshire model
x	Notch acuity ratio (in normalised skeletal stress conversion equation)
x_0	Fitting factor (in LCSP model)
y	Stress ratio or normalised skeletal stress (in normalised skeletal stress conversion equation)
Z	Scatter factor
σ	Stress
σ_1	Maximum principal stress
σ_1^*	Maximum principal stress at the skeletal point
σ_2	Intermediate principal stress
σ_3	Minimum principal stress
σ_m^*	Mean stress at the skeletal point
σ_{net}	Net section stress
σ_{ref}	Deformation mode dependent reference stress
σ_{rep}	Representative rupture stress
σ_{ss}	Constant true stress
σ_{UTS}	Ultimate tensile strength
σ_{VM}	Von Mises stress
σ_{VM}^*	Effective stress at the skeletal point
ε	Strain
$\varepsilon_1, \varepsilon_2, \varepsilon_3$	Principal strains
ε_f	Uniaxial failure strain
ε_{fmx}	Multiaxial failure strain
ε_p	Plastic strain
$\dot{\varepsilon}$	Strain rate

$\dot{\varepsilon}_1, \dot{\varepsilon}_2, \dot{\varepsilon}_3$	Principal strain rates
$\dot{\varepsilon}_m$	Minimum creep rate
$\dot{\varepsilon}_{ss}$	Constant strain rate
$\dot{\varepsilon}_{II}$	Strain rate during secondary creep
$\bar{\varepsilon}$	Effective strain
$\dot{\bar{\varepsilon}}$	Effective strain rate
12CrMoV 11-1 steel	Steel consisting of 12 % of chromium, 1 % of molybdenum and 0.3 % of vanadium

1 INTRODUCTION

Use of nuclear energy comes with a price: high radioactive fuel waste that needs to be taken care of. The time for the disposal of the nuclear waste is planned to begin in year 2020. Finland and Sweden have the same solution for the disposal: restore it in a safety package to the bedrock in 400-500 meter deep for at least 100 000 years. The whole disposal concept of nuclear fuel waste has to meet high safety requirements. The actual waste will be packed in cast iron canister that will be sealed inside a copper disposal canister. This copper canister is the barrier, which should keep the inner part unharmed and enable the storage for the long period inside the ground. [1]

In order to be sure that the disposal canister will last for the planned disposal time, the canister copper (Cu-OFP) needs a lot of careful mechanical testing. One of the most important mechanical testing methods for the copper is creep testing. The disposal canister copper will be exposed to multiaxial stress states and therefore creep inside the bedrock, thus the amount of creep transformation has to be investigated. The uniaxial and multiaxial creep testing gives valid information on the creep properties. Multiaxial creep testing has gained interest because of the possibility to perform shorter creep tests with equally informative data as with uniaxial testing. Different test specimen geometries can be used for uniaxial and multiaxial creep testing. Most common specimen geometries are plain round bars for uniaxial testing and CT or round double notched bars for multiaxial testing. When notched specimens are used, the notches should be as sharp as possible to achieve a high level of multiaxiality. Usually the round bars are manufactured by turn-milling, which bends the bar in some amount, and therefore the bars have experienced cold work before the actual creep testing begins. The main goal in this thesis is to try out a new multiaxial specimen geometry made completely by wire-erosion. The new geometry includes a square shaped test bar that has circumferentially two sharp octagonal shaped notches. Creep testing with a geometry, that hasn't experienced cold work during manufacturing is thought to receive more realistic information on the creep properties. [2,3,4,5]

This thesis work consists of theoretical and experimental sections. The theoretical part will go through the final disposal method of the nuclear fuel and some important facts concerning the disposal canister. The creep theory in general and the creep testing methodologies of the canister copper will be observed for both uniaxial and multiaxial situations. The theory of multiaxiality and creep modelling will be also discussed. For interest the impact of the sulphide rich groundwater on the creep properties is studied according to earlier research by VTT. The experimental part consists of ten tests at different stress and temperature. Four of the specimens are square

shaped (the new geometry) and six are round shaped. The square bars were manufactured by wire-erosion and the first three round bars were turn-milled. The last three round bars were gently turn-milled, as a try-out to see is it possible to minimize the amount of cold work by turn-milling or is the wire-erosion only possibility. Post-metallographic evaluation and the FE analysis are included to see the deformations and the amount of multiaxiality inside the specimen. The FE analysis is also used to determine the skeletal point and the corresponding skeletal stresses, which is challenging for sharp notches. In the end there will be discussion and conclusions about the results and also few thoughts about the needed future actions.

2 FINAL DISPOSAL OF NUCLEAR FUEL

Final disposal of the nuclear fuel waste is scheduled to start in year 2020. The main factor affecting the final disposal schedule is the cooling down period of the fuel. The nuclear plant fuel waste in Finland requires a cooling down period of approximately 40-60 years (depending on the nuclear power plant) before final disposal. Finland and Sweden have the same concept of restoring the nuclear fuel. The plan is to restore the fuel waste into a bedrock repository about 400-500 meters deep, so that the waste is isolated from living nature and people. In the next chapters the concept of the final disposal, the final disposal canister and the requirements and material needed for the canister will be presented in more detail. [1,6]

2.1 Concept of final disposal

The concept of the final disposal in Finland is based on a Swedish concept called the KBS-3, which is developed by SKB, the Swedish nuclear waste management company. The idea is to use multiple release barriers, where the possibilities of deficiencies in one barrier or geological changes in bedrock are taken into account. The first release barrier is that the nuclear fuel waste is in ceramic state itself. Other barriers are fuel cladding, final disposal canister, bentonite and bedrock (Figure 1). [6]

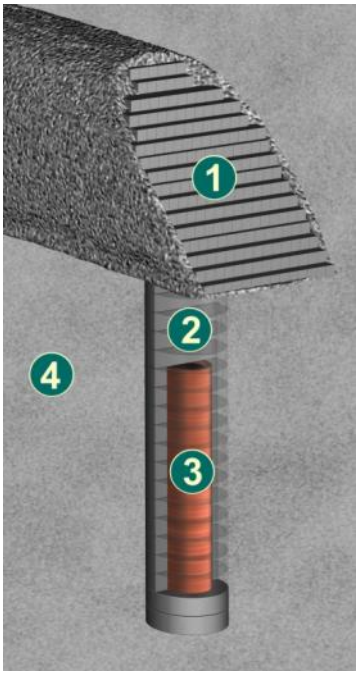

Figure 1.The principle for final disposal and the use of release barriers: 1) Tunnel backfill 2) Bentonite 3) Final disposal canister and 4) Bedrock. [6]

The final disposal canister consists of a copper outer shell and an inner nodular graphite cast iron canister. The main function of the copper outer shell is to protect the inner parts from corrosion caused by the groundwater. The inner part of the canister has to withstand the mechanical stress created by the bedrock surrounding. The inner part is also designed to endure extreme conditions, for example earthquakes or thick ice layers caused by glacial period. In Finland altogether 2800 canisters are needed eventually for the fuel waste. The examination of the canister materials has to be very thorough because the canister has to last at least 100 000 years in the bedrock without any leakage. More specific information about the outer disposal canister is found in the chapter 2.2. [6,7,8]

Bentonite barrier works as a buffer material in the disposal hole and its function is to isolate the disposal canister from the surroundings. When bentonite is in contact with water, it expands to seal the space between the canister and the bedrock. It also stops the possible radioactive leakage and protects the canister from movements of the rock. Backfill (Figure 1, number 1) is also one barrier stage. Backfill material consists of clay blocks and bentonite pellets, which are used to fill up the disposal tunnels after the disposal canister and bentonite are placed. The idea is to keep the disposal tunnel totally isolated, maintain the mechanical stability of the tunnels and also prevent the tunnels from turning into flow routes for groundwater. [6]

Bedrock works as the protective area for the nuclear waste: it protects the canisters from impacts, provides mechanically and chemically stable conditions and limits the amount of groundwater coming into contact with the final disposal canisters. Because groundwater in the 400 meter deep bedrock is almost oxygen-free and flows very slowly, the corroding effect of groundwater on the disposal canisters is very small. Finland's bedrock is very stable, and the probability for major ground movements inside the bedrock is low. The bedrock itself also blocks effectively direct nuclear radiation. [6]

2.2 Final disposal canister

As mentioned earlier the final disposal canister consists of an outer shell and an inner canister. The main interest in this thesis focuses on the copper outer canister. The copper canister is a 50 mm thick capsule surrounding the inner canister and protecting it from corrosion. The canister holds either 12 boiling water reactors (BWR) or VVER-440 (Russian version of pressurized water reactor) fuel assemblies or four pressurized water reactor (PWR) fuel assemblies. As an example the measurements and the total weight of the BWR canister are represented in Figure 2. [9]

Calculated Weight (kg):	
Copper Canister	7 400
Cast Insert	13 600
Fuel Assemblies (BWR)	3 600
In Total	24 600

Figure 2. Copper canister with cast iron insert for BWR fuel. Calculated weight in total is also presented. [9]

There are mainly three ways to manufacture the copper shell: 1) roll forming of tube halves that are welded together or seamless tubes produced by extrusion, 2) pierce and draw processing or 3) forging. The copper shell can have an integral flat bottom and a welded lid on top (method 2 for example) or a separated bottom which is joined later on with a weld. The top lids have a shoulder by which the canister can be gripped using a gripping device during lifting operations. The welding of tube halves and copper bottoms and lids can be done by electron beam welding (EBW) or by friction stir welding (FSW). The difference between EBW and FSW is that EBW is a fusion welding technique and the FSW joints are produced at a temperature of 700-900°C, which is below the melting point of copper. A picture of the canister components is found in Figure 3. During manufacturing some amount of cold work may appear in the material. The cold work may increase the creep strength and reduce ductility and thereby jeopardise the long term safety of the canisters. [3,7,8,9,10]

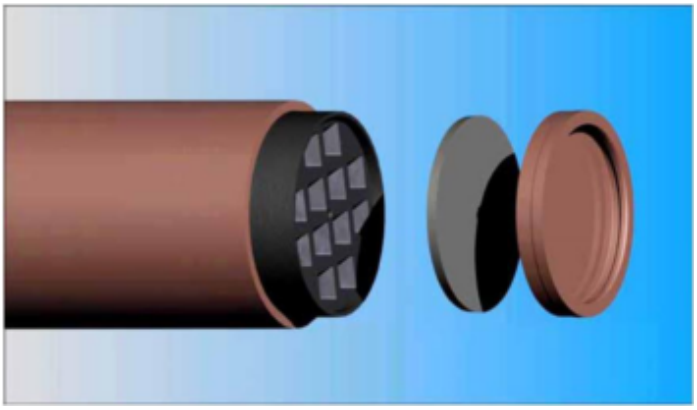

Figure 3. The final disposal canister for BWR. Components from the left: copper outer shell, iron insert, steel lid and copper lid. [7]

2.2.1 Requirements for canister

The copper canister has to last at least 100 000 years inside the bedrock without chemical, mechanical or thermal failure. [2] To be able to estimate the different requirements the copper canister should meet, the repository environments influences have to be taken into account. In the next chapters some of the effects are discussed from mechanical and chemical perspectives.

2.2.1.1 Mechanical requirements

The main mechanical processes for the canister are deformations due to thermo-mechanical loads and isostatic load. The thermo-mechanical load is due to the temperature changes inside the bimetallic structure of the canister. When the temperature increases, the copper shell will expand more than the iron insert because of its higher thermal expansion coefficient. The canister will be exposed to multiaxial stress states when the external hydrostatic pressure and the swelling pressure from the bentonite are developed. It has been predicted that during glacial period groundwater pressure, swelling pressure and the pressure caused by the thick ice layers create at maximum an isotatic load of 45 MPa to the canister. In “normal operation condition” (without ice layers) the load is expected to be around 15 MPa. Some additional loads might appear during handling in the facilities or during transportation to the final repository. The maximum radioactive dose rate at the outer surface of the canister should be less than 1 Gy/h. Higher rates might cause more radiolysis of groundwater and alteration of the bentonite buffer. [3,11,12]

Initially there is a 1.7-3.1 mm axial gap between the iron inner canister and the copper shell. After 200 years this gap will close due to the hydrostatic pressure from the groundwater. The copper should be able to withstand this deformation without any crack formation. Temperature during these 200 years is approximately 80-90 °C and after 1000 years the temperature will slowly decrease to 11 °C, which is the temperature of the surrounding bedrock. In 80-90 °C creep in the copper becomes significant and the gap between inner part and shell will close. To avoid cracks in the copper material

during this closing process, the ductility of the copper has to be high enough. The proper ductility of the welded parts in the canister needs special notice, because they are most likely weaker than the base material in the canister. In this study the main interest is focused on the base material properties. [2,3,8]

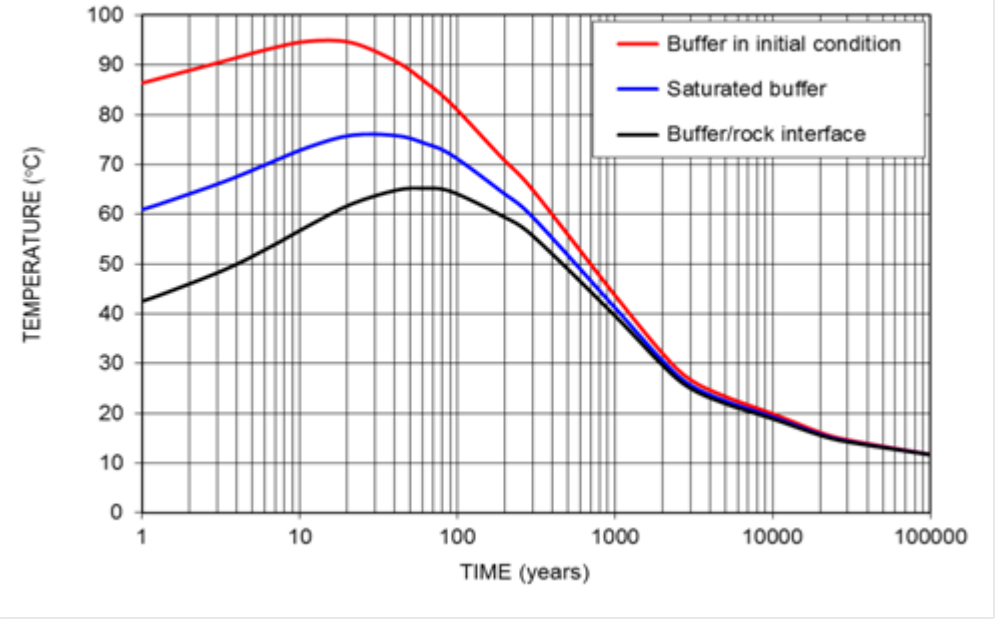

Figure 4.Predicted time dependence of temperature for buffer in initial condition, saturated buffer and buffer/rock interface.[4]

The temperature of the disposal canister is caused by the radioactive decay of the spent fuel inside the canister. The heat is generated in the fuel pellets and is transported by conduction and radiation to the canister insert, to the canister overpack, bentonite buffer and to the near and far field. Elevated temperatures will continue to persist for thousands of years, but the maximum temperature will be reached between 10 and 30 years after disposal. The temperature on the surface of the canister shouldn't increase above 100 °C, because higher temperatures might decrease the chemical stability of the bentonite in the disposal hole. Figure 4 shows the temperature change according to time for buffer material at initial and saturated states and for buffer/rock interfaces. [4,11,13]

2.2.1.2 Chemical requirements

The chemical environment in the repository may cause different kind of reactions in the copper canister. Factors that affect the stability of copper in repository are microbial activity, availability of oxidants in the repository environment, the thermodynamic stability of copper in aqueous solutions, availability of sulphide in the groundwater, different kind of corrosion reactions and the structural stability of the canister. Trapped oxygen inside the repository is involved in many of the reactions mentioned above, for example microbially induced reactions near the bentonite/host rock interface, corrosion of the copper canister and inorganic reactions with minerals (especially pyrite) in the bentonite. Also the radiation from a spent fuel canister could affect the chemical

conditions in the near field. The ionizing radiation will produce both molecular and radical oxidants and reductants through radiolysis. [13]

Corrosion is the biggest threat to the canister in the repository. The first oxidizing period is considered the most harmful, especially when considering the risk of localization of the corrosion attack. The main corrosion reactions for the canister are considered to be general (uniform) corrosion, metal (galvanic) corrosion, localised corrosion (pitting, crevice corrosion), stress corrosion cracking (SCC) and microbial corrosion (initiating uniform corrosion and SCC). Copper is unstable in water in the presence of sulphide ions. In the Finnish Olkiluoto repository, hydrogen sulphide HS^- (or, rather, H_2O/H^+ in the presence of HS^-) is considered the most prevalent oxidant. Corrosion reaction due to sulphide (accompanied by the evolution of H_2) is predicted to cause more than 95% of the total wall loss of the canister during the canisters lifetime. The main sources of sulphide are the groundwater and the dissolution of pyrite (FeS_2) impurities in the bentonite. Microbial activity may also release some sulphide. In the presence of oxygen, any free sulphide ions will be oxidized to sulphate. [11,13,14,15]

Table 1.The variation of hydrochemical properties and microbes at Olkiluoto in different depth ranges. The variation in pH is caused by calcite equilibrium in deep groundwaters and follows the variation in carbonate (alkalinity). Vertical lines in the redox column mean steady conditions. Variations in microbe populations are shown. MOB, MRB, IRB, SRB are methane oxidizing and manganese, iron, and sulphate reducing bacteria. [13]

Depth (~m)	Used classification	Water type	Cl (mg/l)	pH	Alkalinity (meq/l)	Redox	Microbes
0	Fresh HCO_3	Ca-Na-Mg-HCO_3-SO_4	<10	5,5	<0,5	Post-oxic	MOB,Acetogens, MRB, SRB
10		Ca-Na-Mg-HCO_3-(SO_4-Cl)	10	7	3	Sulphidic	Acetogens, IRB, MRB, SRB
100	Brackish HCO_3	Na-(Ca)-Cl-(HCO_3-SO_4)	2000	7,8	4		
200	Brackish SO_4	Na-(Ca)-Cl-(SO_4)	4500	7,5	1,0		Acetogens, MRB, IRB
300	Brackish Cl	Na-Cl	5000	8,2	0,4	Methanic	Acetogens, SRB, IRB, MRB
400	Saline	Na-Ca-Cl	6000	8	0,2		Acetogens, Methanogens
600		Ca-Na-Cl	14000	7,8			
1000			50000	7,5	<0,2		Methanogens, Acetogens

In Table 1, the hydrochemical conditions in Olkiluoto bedrock 400 meters deep are shown. The pH-level at that depth is around 8 and the chloride amount 6000 mg/l. The thermodynamic stability of copper and of the oxides decreases in the presence of chloride ions and in water at low pH. Chloride ions move slowly along groundwater to the repository. The chloride concentration of the bentonite pore-water (the free water in the pores of the bentonite) will increase with time as the buffer saturates and as the pore-water equilibrates with the groundwater. It has been studied that an increase in

pore-water pH due to an alkaline flow from cementitious material would induce a passivation of the canister surface. On the other hand, bentonite clays are known to have a large pH-buffering capacity, which would refer that the pH changes in the repository are quite small. [14,16]

2.2.2 Canister material

The material chosen for the canister has to withstand the mechanical and chemical stresses mentioned above. Also the material needs to be well characterised, easy to manufacture and available in large quantities. Maintaining the isolation of the radioactive contents is an important function for the canister. The canister shell is not meant to be the load carrying structure but the gastight and waterproof barrier between the insert iron and the surrounding environment. To be able to function a long period as a barrier, the canister must not be penetrated by any of the mechanical loads affecting the canister. [3]

Copper has been discovered in several international waste disposal programmes as a suitable canister material on the basis of its cost and corrosion resistance. Experimental and theoretical studies show a wide stability range for metallic copper, and also corrosion effects are considered to be small in the mildly alkaline and reducing environment of the repository. Oxygen free high conductivity copper (Cu-OF, OFHC) was first considered as a potential material for the canister, but it was discovered that Cu-OF would have too low creep ductility. The chosen copper alloy for the canister is oxygen free copper alloyed with 50 ppm of phosphorus (Cu-OFP), which has better creep properties and also higher creep strength than Cu-OF. The creep ductility of the copper should be at least 10 %. Material properties of Cu-OFP are shown in Table 2. [9, 17]

Table 2.Material properties of the Cu-OFP. [2,18]

Property	Value
Elastic modulus (GPa)	118
Poissons ratio	0.345
Thermal expansion coefficient (10^{-6} 1/°C)	16.9
Density (kg/m^3)	8900
Yield stress (MPa) (0.2 %)	39, 43, 50
Tensile stress (MPa)	206- 208
Tensile strain (A50) (%)	51- 54
Hardness (HV5)	38- 41
Grain size (µm)	120- 150

The Cu-OFP material should fulfil the specification in standard EN 1976:1998. In the standard the additional requirements for the allowable amounts of some elements are: oxygen < 5 ppm, phosphorus 30–100 ppm, hydrogen < 0.6 ppm and sulphur < 8 ppm. The effects of these elements in the copper composition are explained in Table 3. The grain size of the copper is limited to < 800 μm to ensure sufficient creep properties. However, to be able to do ultrasonic testing later on, the grain size is currently limited to < 360 μm. [3,19]

Table 3.Requirements and comments concerning chemical composition of the canister copper. [7]

Property	Specification	Comments
Weldability	O < 5 ppm	Higher levels reduce weldability.
Ductility	H < 0,6 ppm	Higher levels reduce mechanical properties (Hydrogen embrittlement).
Tensile strength, ductility	S < 8 ppm	Higher levels reduce mechanical properties by non-dissolved sulphur, which will be concentrated on grain boundaries.
Creep ductility	P 30–70 ppm	A phosphorus content of this order reduces the influence of sulphur impurities, increases creep ductility, increases recrystallisation temperature and has only small influence on weldability.

3 CREEP TESTING METHODOLOGIES OF DISPOSAL CANISTER COPPER

The copper canister has to endure different kinds of mechanical stresses and chemical impact. To test the properties that influence the ability to endure different stresses, various testing procedures have been developed. Creep testing provides valid information on the life-time of metals in elevated temperatures. Creep rate and ductility are related to stress, temperature and microstructure. To be able to select and use the copper material in the disposal canister, the material needs to be tested so that it has the ability to resist some amount of deformation and ensure that fractures (for example creep cracks) do not occur. Today most constant load creep tests are performed in single specimen dead weight lever machines with continuous displacement measurement. The existing creep test data for Cu-OFP material covers testing times little over 10 years, which means that extensive extrapolations has to be done to be able to predict the creep behaviour up to 100 000 years. In addition the creep behaviour in the repository involves low temperature creep which is not as well studied as high temperature creep. These facts create challenges to the prediction of Cu-OFP creep behaviour in the repository. [19,20,21,22]

The first section is focused on the theory of creep and the uniaxial and multiaxial creep behaviour. The major interest focuses on the multiaxial behaviour. The different specimen geometries are presented in more detail and compared with each other. Creep modelling theory and definitions are discussed as well as the impact of the environment (or more specific the effect of sulphide rich groundwater) on the multiaxial creep properties.

3.1 Creep of copper

Creep is defined as time-dependent plastic deformation under a fixed stress at elevated temperature, which is usually half or more of the melting temperature of the studied substance. Creep is usually only important at temperatures over 0.4 T_m (in Kelvin) for alloys and 0.3 T_m for pure metals (T_m is the melting temperature). For copper 0.3 T_m is 407.15 K (134 ºC). A typical plot of the strain versus time is shown in Figure 5. Usually creep tests are done at higher temperatures than the actual service temperatures to keep the testing times reasonable. The final and larger service times are then extrapolated from the shorter testing periods. Larson-Miller parameter P is often used as a tool for extrapolation. [23,24]

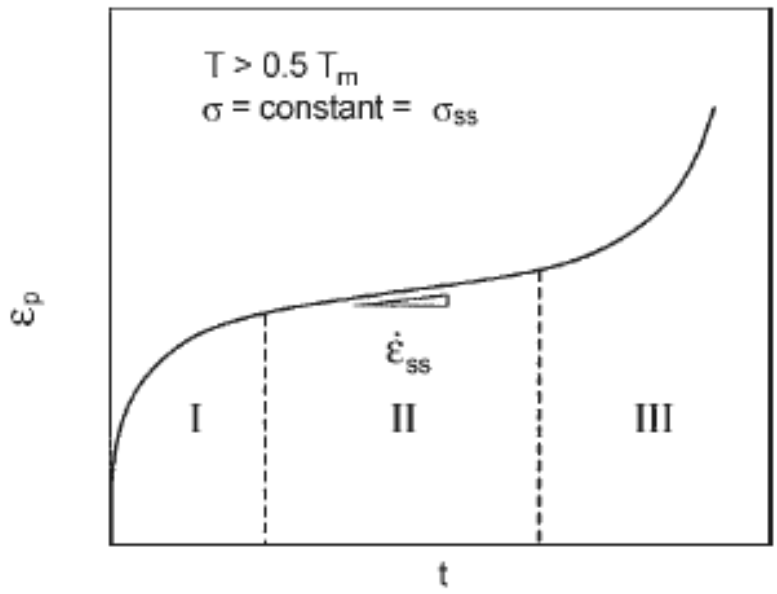

Figure 5.The three stages of creep (I, II and III) in constant stress. T_m is melting temperature, σ_{ss} is the constant true stress, ε_p is plastic strain and $\dot{\varepsilon}_{ss}$ is constant strain rate. [23]

Classical creep behaviour is divided into three stages: primary, secondary and tertiary creep (Figure 5). In Figure 5 primary creep occurs during and right after loading and the creep-rate (plastic strain-rate), $\dot{\varepsilon} = d\varepsilon/dt$, is changing with increasing plastic strain and time. Dislocations in the metal structure are being formed and when the amount of dislocations is high enough, dislocations intersect and create obstacles that prevent the further movement of dislocations. This means that the metal is work hardening. In secondary (or steady state) creep (Figure 5, stage II), the strain rate decreases to a value that is constant over a range of strain. During the stage II the work hardening and recovery rates are more or less in balance. Recovery of the material means that some of the dislocations are destroyed. After the secondary creep, the deformation rate starts to increase and finally leads to rupture (Figure 5, stage III). This last stage is called tertiary creep stage. Creep behaviour is usually characterised with two parameters: minimum creep rate $\dot{\varepsilon}_m$ and time for rupture t_r at a given stress and temperature. The strain rate during secondary creep is given:

$$\dot{\varepsilon}_{II} = B\sigma^n e^{(-Q_c/RT)}, \tag{1}$$

where B is a material constant, n is a creep exponent and Q_c is the activation energy of creep. This creep law is called Norton creep or the power-law creep. At high stresses and deformation rates the power-law behaviour in Equation 1 is not valid anymore. This stress behaviour is called power-law breakdown. The power-law breakdown is thought to be the dominating creep mechanism in the repository. [10,22,23,24,25]

3.1.1 Different creep mechanisms and deformation map

Creep mechanisms can be divided into dislocation and diffusion controlled creep. The dislocation creep occurs by movement of the dislocations in metals. When the moving dislocation meets an obstacle, it can overcome the obstacle by adding or emitting vacancies (called climb) if temperature or stress is increased. In diffusion creep the vacancies move along grain boundaries. At different stresses and temperatures different mechanisms are important: higher temperatures and lower stresses favour diffusion creep, while lower temperatures and higher stresses favour creep mechanisms based on dislocation glide.

There are three types of secondary creep, which are diffusion controlled: Harper-Dorn, Nabarro-Herring and Coble creep. The differences between the three types of creep are in the diffusion mechanisms. The Harper-Dorn creep involves diffusion of vacancies from the edges of dislocations normal to the tensile axis to the edges of dislocations parallel to the tensile axis. The Harper-Dorn creep occurs at low stresses and temperatures and the creep mechanism is influenced by grain size. The Nabarro-Herring creep is a higher temperature process which depends on the bulk diffusion of the vacancies. The Coble creep, which occurs at lower temperatures, depends on vacancy diffusion along grain boundaries. The Coble creep is faster than the Nabarro-Herring creep at lower temperatures. Creep rates are inversely proportional to the grain size for the Harper-Dorn creep. In the Nabarro-Herring creep rates are inversely proportional to the square of the grain size and for the Coble creep inversely proportional to the cube of the grain size. In all of these mechanisms the creep strain rate is proportional to the stress. It has been suggested that at the low stresses and temperatures (which are the expected circumstances in the copper canister in service) the Coble creep is the most likely creep mechanism. [23,24,25]

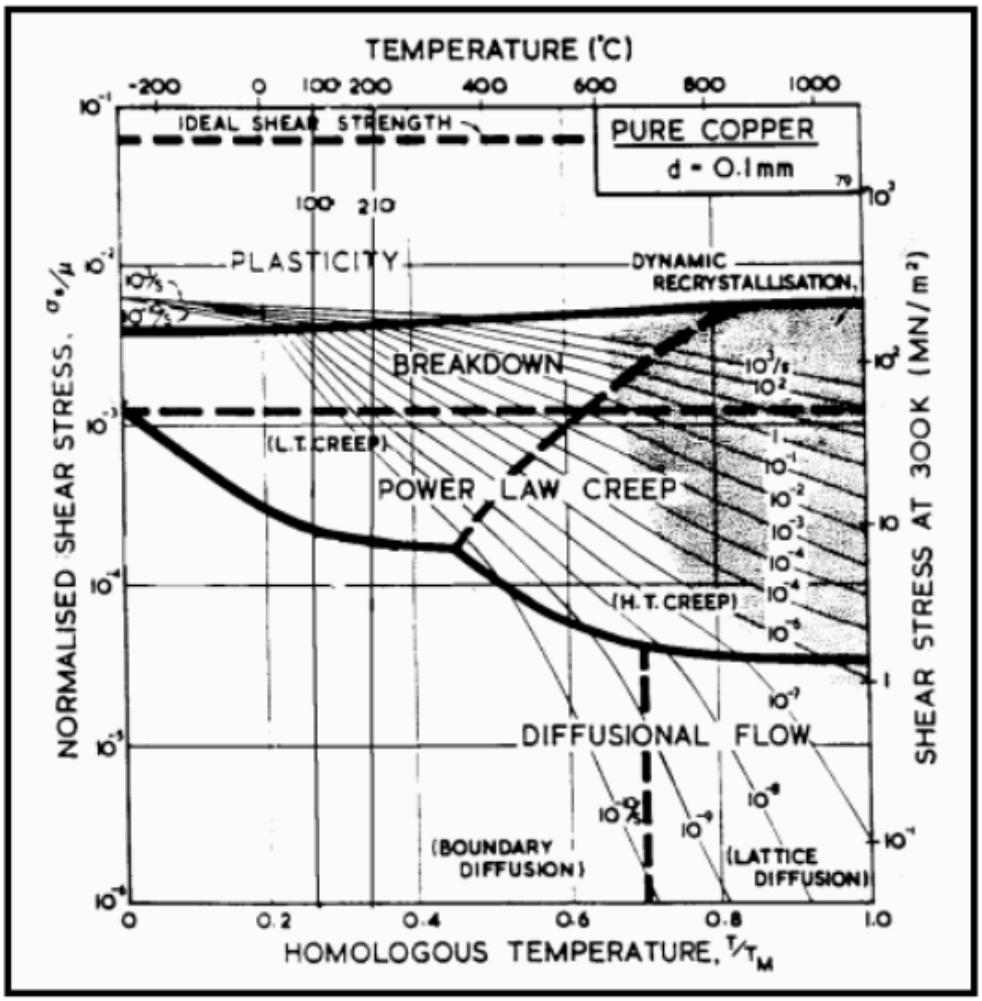

Figure 6.Deformation diagram for pure copper with a grain size of 100 μm. [24]

In a deformation map (Figure 6) the deformation mechanisms are balanced with each other: in one area different deformation mechanisms can exist at the same time, but only one mechanism is dominant. The vertical axis corresponds to the applied shear stress. The deformation maps are material dependent, and in Figure 6 the map is made for pure copper with a grain size of 100 μm. As shown in Figure 6, the power-law and power-law breakdown creeps have a boundary at 100 MPa stress: below 100 MPa the deformation at the relevant temperatures is described as the power law creep and above 100 MPa as the power law breakdown creep. The low temperature creep (L.T. creep) and the high temperature creep (H.T. creep) areas can also be seen. The deformation maps are developed for many materials by using a combination of theoretical analysis and experimental measurements. [24,25]

3.1.2 Uniaxial creep

The simplest way of handling the creep test is to perform uniaxial creep tests. In the uniaxial test the stress is thought to effect only in one direction, which simplifies the interpretation of the creep test results. A disposal canister is exposed to the multiaxial stress states in the repository, which means that the uniaxial creep testing alone is not

enough to predict the behaviour of the canister copper. The majority of the material creep tests have been performed using uniaxial tests and this will probably continue in the future. Most of the existing material creep data have been generated using uniaxial tests. Nowadays more and more multiaxial creep tests are being performed, which makes it easier to compare and investigate the measured multiaxial creep test data. [26]

Uniaxial tests are performed by heating the test piece to a specific temperature and then straining the specimen by means of a constant tensile force applied along its longitudinal axis for a certain time. The goal is to obtain a specific creep elongation of the specimen (called interrupted test) or continue the test to rupture (called uninterrupted test). Uniaxial creep tests are usually performed by round bars without notches (Figure 7). In Figure 7 the shoulders are used to measure the elongation of the specimen. More about the testing circumstances in uniaxial test is found in the chapter 4.1. [27]

Figure 7. Round uniaxial creep test specimen. [28]

3.1.3 Multiaxial creep

As mentioned earlier the copper canisters will be subjected to the multiaxial stress states. The stress state affects failure mechanisms, failure modes and ductility. Experience shows that the creep failures often occur at sites of the stress concentration where the triaxial tensile stress state is present. The actual stress state depends upon the applied loading conditions and geometrical configurations of the component exposed to the loads. Different materials respond differently to multi-axial stress situations. In the copper canister under multiaxial stress, the creep cracks can be initiated prematurely. High degrees of multiaxiality can be found especially at notch roots or in front of a crack tip. [26,29,30]

3.1.3.1 Definition of multiaxiality

Any complex stress combination with stresses in three directions and six different shear stresses can be reduced to just three stresses: the principal stresses $\sigma_1>\sigma_2>\sigma_3$. The most commonly used effective stress concept in high and low temperature ranges is von Mises effective stress, which is based on a concept of a maximum energy of distortion:

$$\sigma_{VM} = \frac{1}{\sqrt{2}}[(\sigma_1 - \sigma_2)^2 + (\sigma_2 - \sigma_3)^2 + (\sigma_3 - \sigma_1)^2]^{0.5}, \quad (2)$$

where σ_{VM} is the von Mises stress, σ_1, σ_2 and σ_3 are the maximum, intermediate and minimum principal stresses of the stress tensor. The von Mises stress describes quite well the deformation of materials under complex loading situations, and it is also a parameter for the creep rupture at high stresses where the rupture is associated with the large deformations and the ductile failure mechanism. However, it has been found that the von Mises criterion underestimated creep for some cases in comparison to available data. This underestimation can be corrected by combining the general model of correlating damage under uniaxial tension with damage under more complex conditions by adopting an equivalent stress. [22,26,29]

In a multiaxial stress system also strains will occur in three different directions, which are assumed to coincide with the principal stress axes. It is supposed that the failure will occur when the effective strain reaches the uniaxial rupture strain value. The effective strain equation is almost identical with the respective stress (Equation 2):

$$\bar{\varepsilon} = \frac{\sqrt{2}}{3}[(\varepsilon_1 - \varepsilon_2)^2 + (\varepsilon_2 - \varepsilon_3)^2 + (\varepsilon_3 - \varepsilon_1)^2]^{0.5}, \quad (3)$$

where ε_1, ε_2 and ε_3 are principal strains and $\bar{\varepsilon}$ effective strain. Similarly, the effective strain rate can be expressed as:

$$\dot{\bar{\varepsilon}} = \frac{\sqrt{2}}{3}[(\dot{\varepsilon_1} - \dot{\varepsilon_2})^2 + (\dot{\varepsilon_2} - \dot{\varepsilon_3})^2 + (\dot{\varepsilon_3} - \dot{\varepsilon_1})^2]^{0.5}, \quad (4)$$

where $\dot{\varepsilon_1}$, $\dot{\varepsilon_2}$ and $\dot{\varepsilon_3}$ are principal strain rates and $\dot{\bar{\varepsilon}}$ is effective strain rate. Multiaxiality can be characterised by a constraint parameter h or by the ratio of maximum principal stress to the von Mises equivalent stress H. These parameters are determined as:

$$h = \frac{\sigma_1 + \sigma_2 + \sigma_3}{3\sigma_{VM}} \text{ and } H = \frac{\sigma_1}{\sigma_{VM}}. \quad (5)$$

As mentioned earlier, the triaxility has a strong effect on the ductility of the materials: the ductility will decrease significantly when high degree of tensile triaxiality are present. The ratio of multiaxial and uniaxial ductility can be expressed by an exponential equation:

$$\frac{\varepsilon_{fmx}}{\varepsilon_f} = 1{,}65 \times e^{\left(\frac{-3h}{2}\right)}, \quad (6)$$

where ε_f is the uniaxial failure strain and subscript *mx* refers to multiaxial conditions. The Equation 6 gives lower multiaxial ductility values at small and negative values of h and is more conservative at high degrees of multiaxiality. [26,31,32]

3.1.3.2 Different specimen geometries and handling of multiaxial creep data

The multiaxial creep tests are usually performed with fracture mechanics specimen CT (compact tension) bars (Figure 8) or circumferentially double notched uniaxial test bars (Figure 9). Both specimens are extracted from the extruded copper cylinder sections (Figure 8 and 10). The CT bars have higher degree of multiaxiality than the notched bars due to the geometrical differences. The NB (notched bar) specimens are easier and cheaper to manufacture than the CT bars, and they can be tested in the same machines as used for standard uniaxial tests. Notches create stress concentrations and affect the stress distribution. By changing the notch profile different stress states can be obtained. The creep deformation is to a great extent concentrated to the region around the notch tip. The stress distribution developed across a notch is sensitive to the material properties. Initially, on loading, an elastic or elastic and plastic stress field is generated. With time, the stress redistribution usually happens (sometimes until a stationary stress state is achieved). More specific knowledge of how the stress redistribution occurs, and leads to strain accumulation, requires numerical analysis (FEM) and complete description of the material behaviour. In double notched bars the fracture is expected to take place in one of the two notches, while the other unbroken one should represent the circumstances close to rupture, making the creep damage investigation possible. [12,29,30]

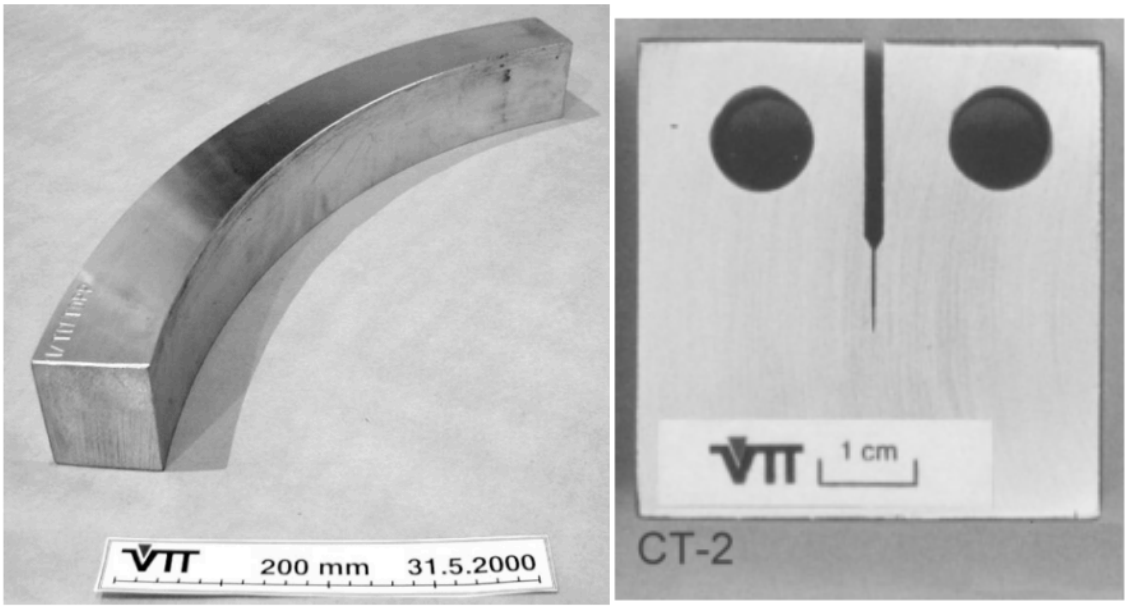

Figure 8. Ring section of a hot pressed cylinder (Cu-OFP) and the compact tension (CT) specimens extracted from it.[28]

Figure 9. Double notched round test specimen.

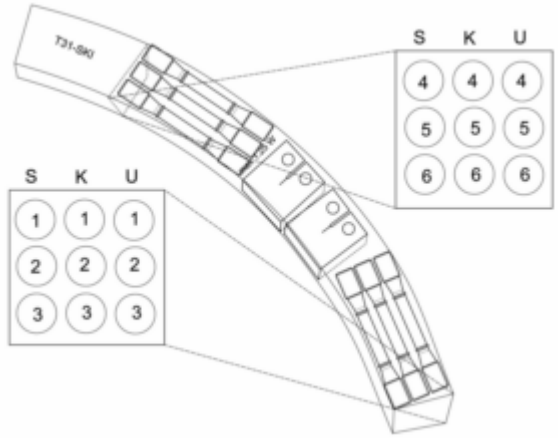

Figure 10. The principle of extracting uniaxial and CT specimens from the copper cylinder sections. [20]

In this work the new testing approach is to use circumferentially double notched square bars (Figure 11). The square bars are made by wire-erosion method (also called EDM= electric discharge machining), because the idea is to avoid any cold work, which usually occurs when the test bars are made by milling. Cold work reduces the creep ductility and at same time increases the creep strength, which might distort the testing results. The cold work consumes some of the available straining capacity of the material, which reduces creep ductility. The reduced creep ductility may affect the notch sensitivity and the creep behaviour under the multiaxial stress state. Geometrical changes (including notches) are frequently associated with the cold work caused by manufacturing and machining processes. It has been found that cold working in compression along the creep load direction has no influence on the creep life or creep rate but the ductility is reduced. Cold working in compression transverse to the creep load direction leads to prolonged creep life but reduced creep ductility. With the EDM method the amount of the cold work should be negligible, and the results should give a more realistic view of the properties of the canister copper. The best solution would be to make a round bar (instead of square shape bar) by the EDM but the manufacturing is considered too challenging and expensive. The amount of material that should be removed with EDM creates challenges. The circumferential notches for the round and square bars are made by the EDM. The notches for the square bars are made in an octagon shape (Figure 12) to avoid too sharp edges and to imitate a round shape. An octagon shape was chosen, because in the first three round bars the round notches were too inaccurate, whereas the

octagon shape notches are possible to manufacture in adequate accuracy. The problem in manufacturing round notches is how the rolling of the specimen can be done during EDM in proper accuracy. However, now it seems that the quality of the round notches is getting better, and it is possible to get some specimens with suitable round notch geometry accuracy. The square shaped area in Figure 12 is designed to match the round specimens original cross-sectional area of the parallel length, and the octagon shaped area is designed to match the round specimens original cross-sectional area across notch throat. [5,10,26,30]

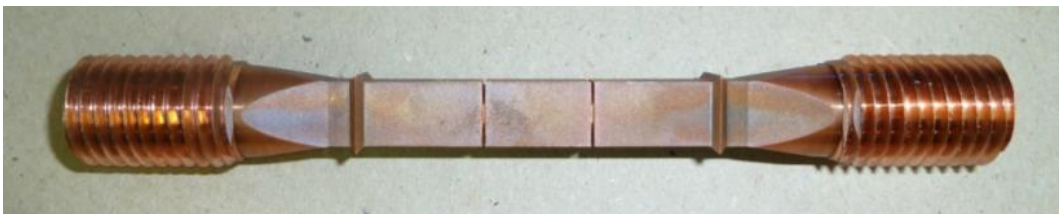

Figure 11. Square circumferentially double notched test specimen.

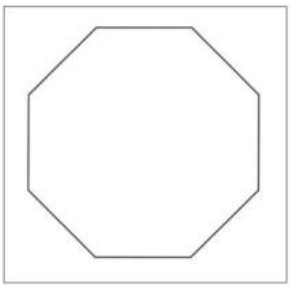

Figure 12. Example of the octagon shaped notch inside square bar.

The notched bar rupture life obtained for a given geometry, loading condition, and temperature should be compared to the uniaxial (plain bar) stress rupture data for the same material at the same temperature to obtain the representative rupture stress, σ_{rep}. Representative rupture stress is the stress applied to a plain bar that results in the same effective strain accumulation or rupture life as that obtained in a notched bar tested at the same temperature. The comparison of the uniaxial and multiaxial testing results is important in order to make valid conclusions from the creep test data. A suitable conversion from multiaxial back to the uniaxial behaviour is also needed. However, the multiaxial creep behaviour under stress does not always correlate directly with the uniaxial behaviour.

For a notched bar, a three-dimensional stress state exists across the notch throat. Numerical computer calculations have shown that for symmetrical shapes and simple loading under constant tension, pressure or bending, a point called a skeletal point exists in the cross-section where the stress state remains approximately constant with time, independent of the elastic, plastic or creep properties of the material. The stress components at skeletal point (the skeletal stresses) can be used to characterize the overall creep behaviour of the notched testpiece. The values of the skeletal stresses stay approximately unchanging with the creep stress exponent, *n* (Figure 13). As can be seen

in Figure 13, the normalized effective stress distribution curves for different *n* values encounter at the same point (*n=1* is an exceptional case). For the notch geometry, or the range of notch geometries tested, it is necessary to determine the significant skeletal point stress parameters: the mean stress σ_m*, the maximum principal stress σ_1*, and the effective stress σ_{VM}*. The values of the normalized skeletal stresses (σ_1*/σ_{net}, σ_m*/σ_{net} and σ_{VM}*/σ_{net}) at the skeletal point vary depending on the notch profiles (Figure 14). The multi-axial stress parameters controlling the rupture (the multi-axial stress rupture criterion) should be interpreted by comparing σ_{rep} with σ_1*, σ_m* and σ_{VM}*.

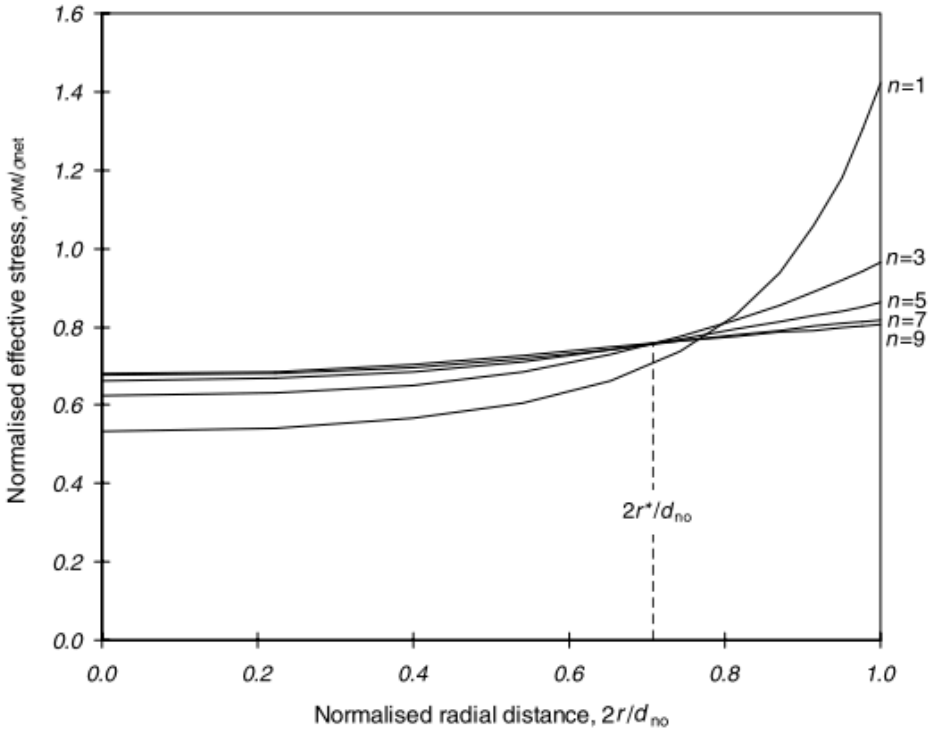

Figure 13. Normalized effective stress distribution at steady state across the throat of a semi-circular notch (d_{no}/r_{no} = 3, D/d_{no} = 1.41). [29]

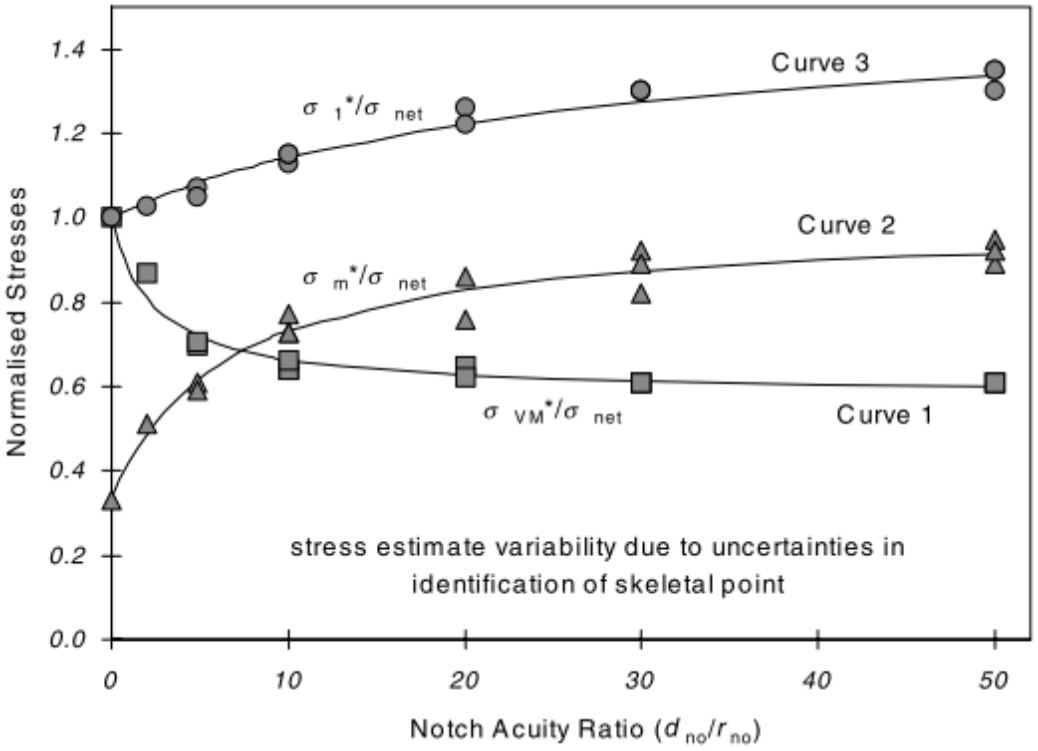

Figure 14.Normalised skeletal stresses as a function of notch sharpness (d_{no}/r_{no}) for D/d_{no}= 1.41. [29]

With the help of the skeletal stresses the creep response of materials at the triaxial stress state can be examined also without numerical computer calculations. The approach relies on the coincidence of the radial location of the skeletal points for each of the skeletal stresses. The accuracy of this approach is a function of the notch geometry. However, for severe notches ($d_{no}/r_{no} > 20$) the effective and maximum principal skeletal stress magnitudes are well defined but the skeletal mean stress is less clearly defined. Also, for these severe notches, the radial locations of the skeletal points for each of the stresses do not coincide. The same applies for blunt notches ($d_{no}/r_{no} < 3$) where the definition of a skeletal point becomes continuously more indistinct as stress gradients decrease towards zero for a plain bar. Nevertheless, for sharp and blunt notches it is still possible to identify a radial location where the approximate skeletal stress values can be determined. [29,30,33,34]

3.1.3.3 Features of multiaxial creep testing

Differences in the testing temperatures and in the stresses usually shift the creep mechanisms to different regimes so that the life prediction becomes difficult, especially at relatively low service temperatures. The multiaxial testing method is developed to receive data from new materials from which long-term service experience is not available. Existing standards for the NB testing have generally been based on two classes of behaviour: the notch weakening and the notch strengthening. This means that the rupture life of the NBs is lower or higher than the rupture life of the plain (uniaxial)

bar tested at the same net section stress. Generally, the notch sensitivity appears to increase as the temperature is decreased. [20,29,31]

One of the main problems in estimating the long-term creep strength is the required testing time: long testing times are expensive and impractical. Studies made by VTT indicate that the multiaxial creep testing reduces the creep lifetime, which enables shorter testing times. The short-term creep testing at high stress and/or temperature tends to be dominated by the failure mechanisms producing the ductile transgranular fracture. In long term testing this can gradually change to a lower ductility mechanism accompanied with the creep cavitation damage at the grain boundaries. The shift can be accelerated by the tensile multiaxiality using notched specimens. In this study the CT-specimens were tested at the temperature of 150 °C and at the reference stresses of 46 and 59 MPa. The concept (Figure 15) is based on the model equation predicting the time to failure as:

$$t_r = A' \cdot \sigma_{VM}^{-v'} \cdot H^{-\mu \cdot v'}, \tag{7}$$

where A' and v' characterise the shape of the uniaxial creep rupture curve (inverse Norton law), and σ_{VM} (or σ_{ref}) is the deformation mode dependent reference stress. H is the ratio of maximum principal stress to the von Mises equivalent stress ($H = \sigma_1/\sigma_e$), which is obtained according to the material and geometrical configurations using appropriate steady-state values. The value of μ varies between limits of 0 (for σ_e-controlled rupture), and 1 (σ_1-controlled rupture). With the grain boundary cavitation $\mu > 0$, it is possible to perform the accelerated creep testing without elevating temperature or effective stress. Usually for copper $\mu \approx 1$. However, because all standard values of the creep strength are obtained by the uniaxial testing, they will not reflect the potential shortening of the creep life by the tensile multiaxiality. Also the most traditional methods of the multiaxial creep testing are not very effective in shortening the creep life or cost effective. [20,33]

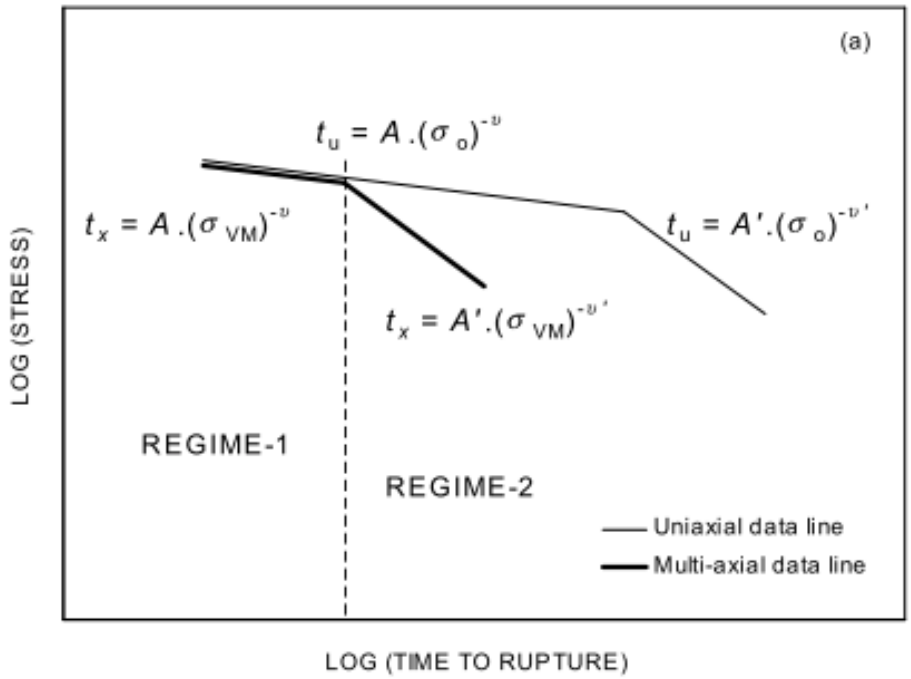

Figure 15. The principle of shortening the creep life by damage in multiaxial loading (CT specimens). Creep life is described by the simple inverted Norton expression. Subscripts u and o refer to uniaxial and subscript x to multi-axial loading; subscript VM refers to von Mises stress. Regime 2 is the region where grain boundary cavitation can dominate creep damage. [20]

However, also different opinions of the effect of multiaxiality on the creep lifetime of Cu-OFP exist. Swedish studies [10,12,30] claim that the creep lifetime under the multiaxial stress state is longer than under the uniaxial stress state (at a given net section stress), which indicates to the notch strengthening (or in another words notch insensitivity) behaviour. Also it was found that, the sharper the notch the longer the creep lifetime. By comparing the results of the notched specimens with the uniaxial specimens, Swedish studies suggested that the creep lifetime for notched specimens could be estimated to be two orders (or more) longer than for the plain bars for the investigated Cu-OFP material. In a study by Rui Wu et al. the testing stresses varied between 170 and 255 MPa, when the temperature was 75 °C in all the 20 creep tests. As shown in Figure 16, the results of the study are presented with the net section stress, whereas in the Finnish studies (mentioned above) the reference stress is used (Figure 15). Another difference between these two studies appears to be the level of multiaxiality present in the specimens: Swedish specimens had quite blunt notches, when the multiaxiality inside the bar is lower. Swedish tests have also been performed at low temperature (75°C), where the actual rupture phenomenon is harder to register because of the long testing times required. For that reason only 8 from the 20 tests were continued till rupture, which is not very informative. To get actual results and see the behaviour of the tested material, creep tests should be continued to rupture. [10,12,30]

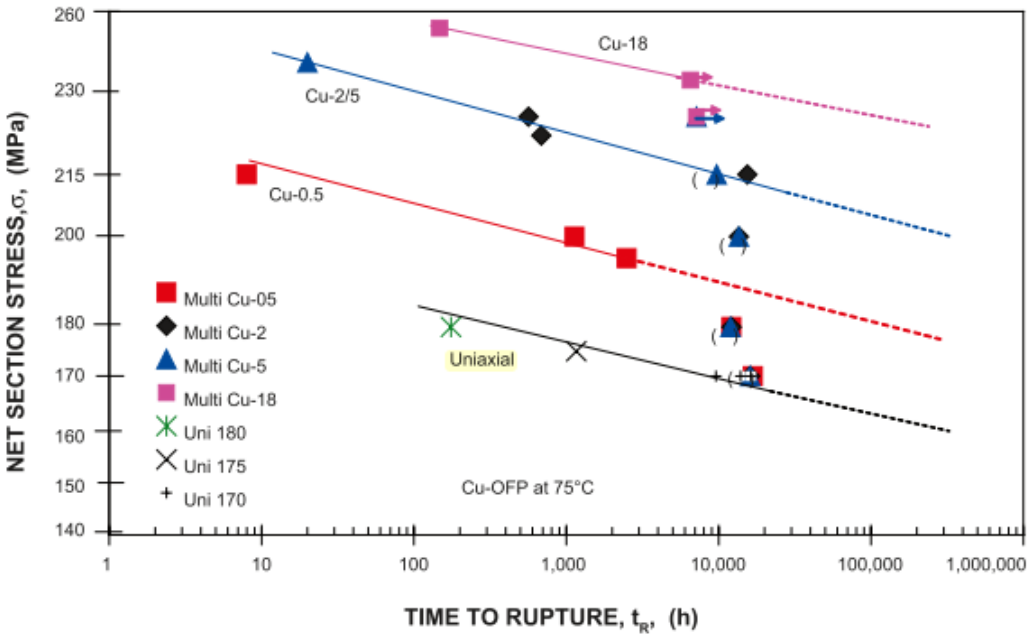

Figure 16. Creep lifetime under multiaxial stress state (multi) as a function of net section stress for notched Cu-OFP at 75°C. Notch acuities are 0.5, 2, 5 and 18. Running tests are indicated by arrows, interrupted tests are in brackets. Creep lifetime under uniaxial stress state (uni) using smooth specimen is included for comparison.[12]

3.2 Creep modelling

To ensure the safe storage and prevent the creep rupture from occurring, it is necessary to predict the amount of the creep deformation in the copper canister. There are different models for the prediction of the creep behaviour, for example: Norton law, Wilshire model, Manson-Haferd-Grounes model, and LCSP model. These models will be discussed more closely in the next chapters. A more detailed interpretation of notched bar test data can be obtained by conducting finite element calculations of the stress redistribution that occurs during creep in the notch area. Finite element method (FEM) is a valid tool for successful interpretation of creep results for notched bars. Different rupture and strain models (the ones mentioned above) can be implemented in FEM to get the proper creep prediction. FEM calculations will be discussed in Chapter 4.3. [10,17,29,30,22]

3.2.1 Norton model and Monkman-Grant relationship

The simplest model for creep strain based life-time predictions is the Norton model and the Monkman-Grant relationship. Even nowadays minimum creep rates are being estimated by the Norton and Monkman-Grant relationship. The simple minimum strain rate based models do not take the primary and tertiary creep regimes into account and therefore predict significantly lower strains. The Monkman-Grant relationship is defined as:

$$t_r = K \cdot \dot{\varepsilon}_m{}^{-r} \quad \text{or} \quad \ln(t_r) = \ln(K) - r\ln(\dot{\varepsilon}_m), \tag{8}$$

where t_r is the time to rupture and K and r are material constants. Note that the constants may be sensitive to both temperature and stress. It has been also studied that the uncertainty of the Monkman-Grant relationship is more significant than thought before.

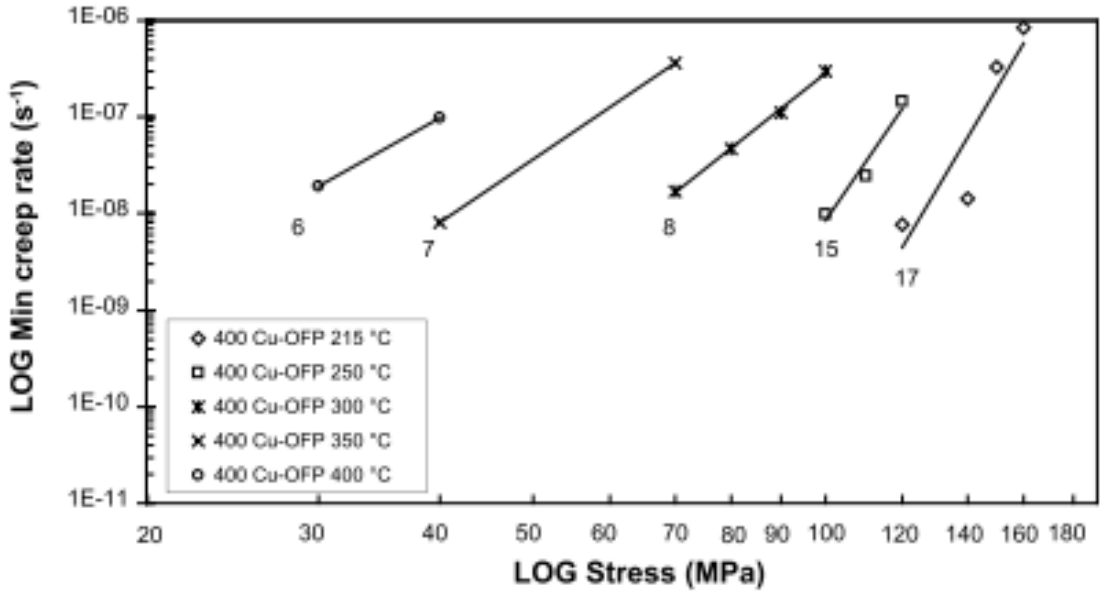

Figure 17. The Norton plot for the creep test series of Cu-OFP. The Norton exponents are marked in the graph.[10]

The simplest version of the Norton model is presented in Equation 1, Chapter 3.1. As can be seen in Figure 17, the Norton model can only present the secondary creep regime and for that reason doesn't describe the actual creep test data very well. Traditionally the minimum strain rate in the dislocation creep range is described by the extended Norton law expression, which is presented in classical expression for polycrystalline metals as:

$$\dot{\varepsilon}_m = A \cdot (DEb/kt) \cdot (b/d)^p \cdot (\sigma/E)^n \cdot e^{\left(-Q_C/kT\right)}, \tag{9}$$

where A is a dimensionless factor, D the diffusion coefficient, E the elastic modulus, b the Burgers vector, d the grain size, p the exponent for grain size dependence, σ is the applied stress, k the Boltzmann's constant and Q_c the activation energy for creep. For high temperature power law creep the stress exponent n for minimum creep rate $\dot{\varepsilon}_m$ will normally range within 3–5 and for low temperature power law creep within 5–7. When using Equation 9, problems usually occur in modelling complex high temperature steels, and what is more important for this thesis, in extrapolation. The stress exponent n and the activation energy Q_c tend to change at stress levels and temperatures relevant for service conditions. The Wilshire model (next chapter) introduces a more effective way for estimation of strain rate, time to strain and time to rupture. [22]

3.2.2 Wilshire model

Modelling creep of copper is challenging, because copper is initially soft but strongly strain hardening material. This means that testing at high stresses (necessary when testing for sensible test durations at temperatures close to the repository conditions) creates scatter in observed creep strength. For this reason the Wilshire rupture model is convenient, because it normalizes the tensile strength. The Wilshire equations provide a method for direct fitting and prediction of the minimum strain rate, time to strain, and time to rupture. The method needs additional tensile test data at the creep test temperatures for the stress normalization. With the Wilshire model the creep activation energy can be defined in a straightforward way. The Wilshire model improves the long term predictions of both the rupture and strain. The Wilshire equation for time of rupture t_r at the stress σ and temperature T is expressed as:

$$\ln(\sigma/\sigma_{UTS}) = -k\left[t_r e^{(-Q_C^*/RT)}\right]^u, \tag{10}$$

where k and u are constants obtained by fitting to the test data, Q_c* is the apparent activation energy and σ_{UTS} is the ultimate tensile strength or another reference stress (like yield stress) at the specified temperature. In Figure 18 is shown, how well the model can predict the creep test behaviour (in this case for uniaxial test). [4]

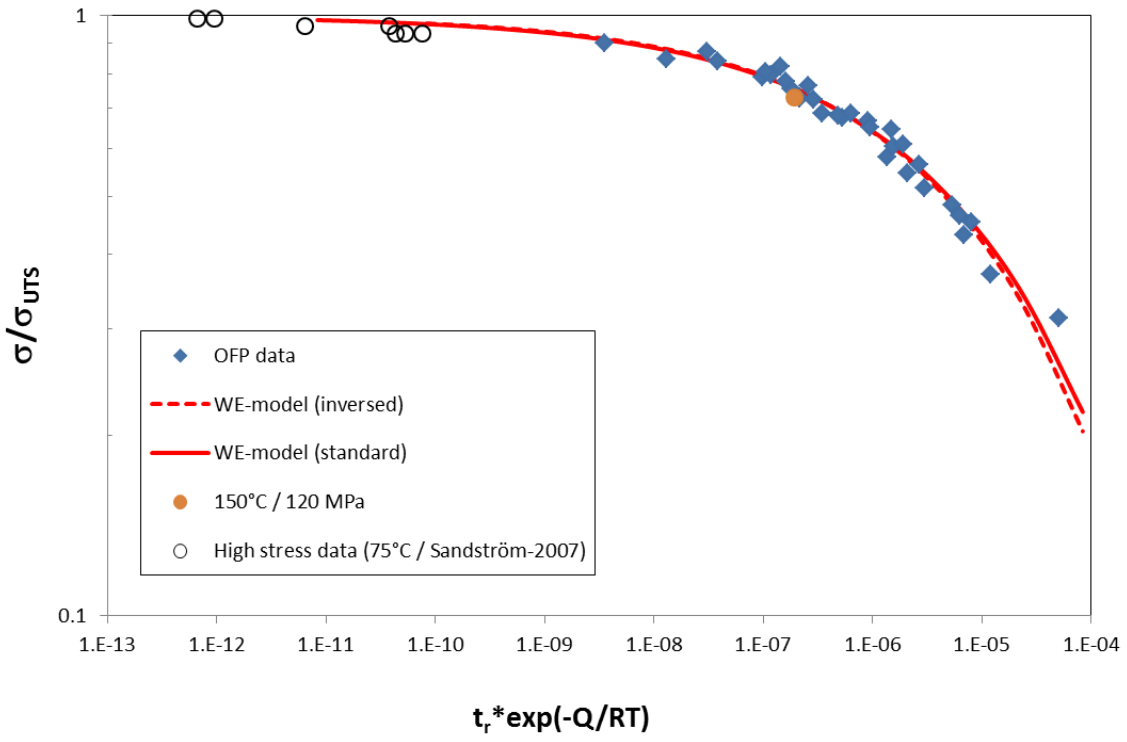

Figure 18. The Wilshire model based life predictions for base material (BM) of Cu-OFP; the large red dot is the running 150℃/120 MPa uniaxial test (running at 10.4 years, predicted life 16.2 years when Q_c=95 kJ/mol). [4]*

3.2.3 MHG and LCSP model

The Manson-Haferd-Grounes creep strain model (MHG) is a simple parametric creep strain model, which is based only on actual strain data. The MHG model predicts the time to the specific creep strain by assuming a parametric relationship (Manson-Haferd) and that the creep mechanism follows an Arrhenius type of temperature behaviour. In addition the model assumes that the creep damage can be related to the accumulated strain. The MHG parameter is defined as:

$$MHG = [\ln(t_\varepsilon) - C]/T = F(T, \sigma, \varepsilon), \tag{11}$$

where C is a constant, t_ε is the time to strain and $F(T,\sigma,\varepsilon)$ is a multi-linear combination of temperature T, stress σ and strain ε. The model is theoretically valid with both constant stress and constant load creep tests. Although the MHG model describes the creep results quite well with minimum number of fitting constants, room for further development was needed, especially in the prediction of curve end point (time to rupture). For this reason the LCSP model was developed. [22]

The logistic creep strain prediction (LCSP) model can be regarded as a further development of MHG. The LCSP model is a creep strain prediction instrument, which is able to predict realistic creep strain curves and strain rates in a large stress and temperature range. The suitable range of stress and temperature for specific material needs to be determined from the existing creep rupture data combined with the time to rupture prediction. The best result in time to strain or strain at specified time is naturally attained using the actual (true) rupture. In extrapolation, or when data is missing the true rupture time is replaced by the master curve prediction for the rupture. The advantage in the LCSP model is that it can be used to predict the strain rates and the time to rupture from the relatively early strain data of unfailed specimens. The accuracy of the model improves when more strain data are available. The LCSP model is perhaps the best alternative for accurate multiaxial creep modelling. [22]

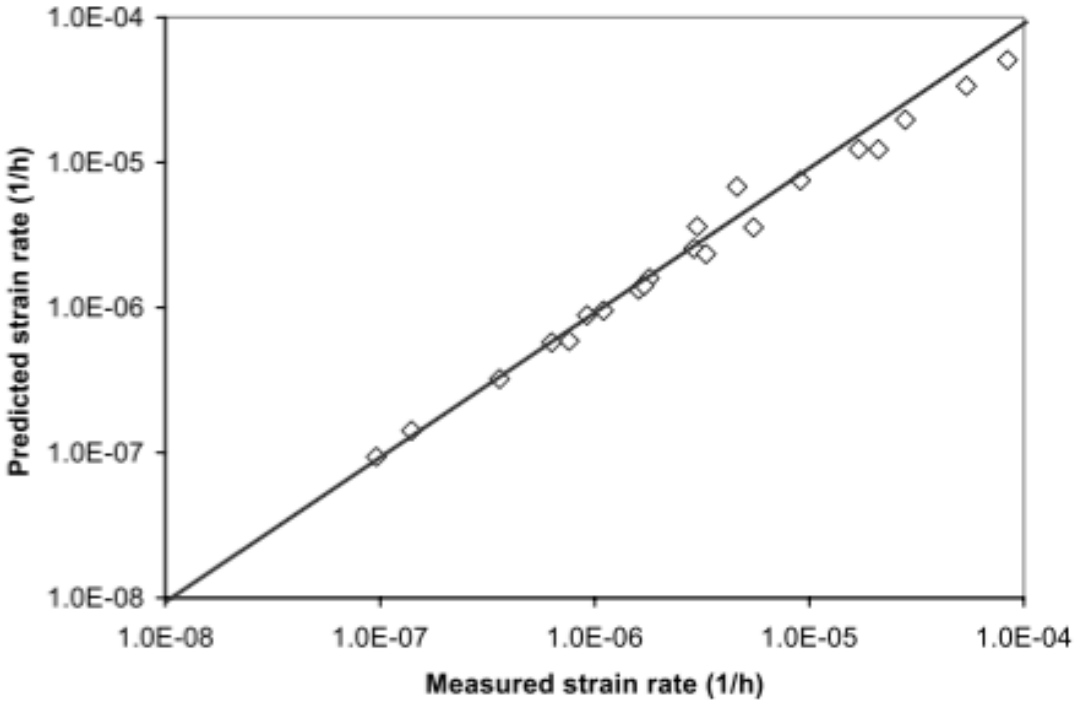

Figure 19. Predicted minimum creep rates by LCSP model for 12CrMoV 11-1 steel against measured creep rates.[22]

In the LCSP model the strain and strain rate depend on the stress, temperature, and time, according to the LCSP functions:

$$\log(t_\varepsilon) = \frac{\log(t_r)+C}{1+\left(\frac{\log(\varepsilon)}{x_0}\right)^p} - C, \tag{12}$$

$$\log(\varepsilon_t) = \left(\frac{\log(t_r)+C}{\log(t_\varepsilon)+C} - 1\right)^{1/p} \cdot x_0\,, \tag{13}$$

$$\dot{\varepsilon} = -\varepsilon \cdot k_1 \cdot k_2 \cdot x_0\,, \tag{14}$$

where t_r is the time to rupture, x_0, p and C are fitting factors and k_1 and k_2 are functions of time to strain. In the easiest case x_0, p and C are constants, but in normally they depend on the stress and temperature. An evaluation of the minimum strain rates is also convenient with the help of the LCSP model. An example of the functionality of the LCSP model is shown in Figure 19, in which the model predicts quite accurately the behavior of the measured values. [4,22]

3.3 Impact of sulphide rich groundwater on creep properties

Groundwater has many components (different ions and compounds), which might have either negative or positive influence on corrosion of Cu-OFP and thus also an influence on the creep properties. Components of the groundwater include for example: sulphide, chloride, ammonium, methane, hydrogen, sodium, calcium, potassium, nitrogen dioxide, and DOC (dissolved hydrogen carbon). Also trapped oxygen, pH-level and microbes at the repository can affect the corrosion of Cu-OFP. It has been studied, that microbes, pH-level, and Cl^-, HS^-, NH_4^+, NO_2^- ions present in the groundwater are considered to have an important role in the corrosion of the copper canister. However, this doesn't give direct information about the effect of mentioned components on the creep lifetime. Most of the corrosion processes can ease the creep of corroding copper, but some mechanisms do not. For example, the corrosion mechanisms that produce hydrogen on metal surfaces can enable the hydrogen to enter the metal under the oxide film. The hydrogen is able to reduce the creep strength of the metal, especially at locations where high tensile stress is present. However the hydrogen producing corrosion processes are in general thought not to be present at repository conditions. Some other corrosion processes can produce vacancies that can enter the metal from the surface. At low temperatures (where the diffusion is slow), these vacancies probably would not affect much the bulk behaviour of copper. If the surface of the canister would start to create cracks, corrosion could become more significant. [13,14,28]

The combined and separated effect on creep properties of all the factors in groundwater is hard to predict and would need a lot of further research. For that reason, the main focus in this chapter is on the effect of sulphide (S^{2-}) that is present in the groundwater. Sulphide, as mentioned in Chapter 2.2.1.2, can have harmful effects on the properties of Cu-OFP. It has been studied by different groups, that sulphide can cause stress corrosion cracking (SCC) in pure copper under anoxic seawater conditions. Sulphide is able to diffuse from Olkiluoto-type groundwater into the Cu-OFP grain boundaries, which might cause embrittlement of the material, for example a brittle creep failure. This kind of unfavourable behaviour can influence the lifetime of all the canisters in the repository. Sulphides can come to contact with the copper canister surface through three different processes: 1) transport via groundwater flow, 2) production at the bentonite/rock interface via sulphate reducing bacteria (SRB) and further transport, and 3) through the SRB activity within bentonite (pyrite reduction). In the groundwater sulphide concentrations are typically relatively low, approximately 1-3 mg/l. The maximum value of sulphide that can be formed via the SRB activity at the bentonite/rock interface is about 450 mg/l, causing a high diffusion gradient through the bentonite. The sulphide concentration that forms through the SRB activity within bentonite is known to be (to a certain extent) dependent on bentonite density. Sulphides can form also within a fully compacted bentonite. If the density of bentonite locally

decreases (for example in case of erosion-corrosion) in some areas, the access of sulphide to the copper surface will be much easier. [10,18,35,36]

However, it is also believed that the SCC behaviour in the copper canister is unlikely, because the maximum concentration of the SCC agents and the corrosion potential of the canister might be below their threshold values for the SCC reaction to start. Other reason for the inhibition of SCC could be that the creep rate of the copper will be higher than the crack growth rate. Also it should be noticed that there are a number of uncertainties affecting the sulphide behaviour in the repository. [13,14]

VTT has studied the uniaxial and multiaxial creep behaviour of the specimens exposed to the sulphide rich groundwater. Different sulphide amounts in groundwater might give different results in creep behaviour. Comparison of the non-exposed creep test results with the sulphide rich groundwater exposed creep results hopefully give information about the sulphides effect on the creep behaviour of Cu-OFP. These studies will be observed in Chapter 4.4. CT and notched bars can be used as the multiaxial creep test specimens also in the sulphide exposure creep testing. However, the notched bars may differ in geometry to the multiaxial NB specimens mentioned earlier. In Figure 20 the NB specimen geometry for the groundwater exposure creep studies by VTT is presented. [18]

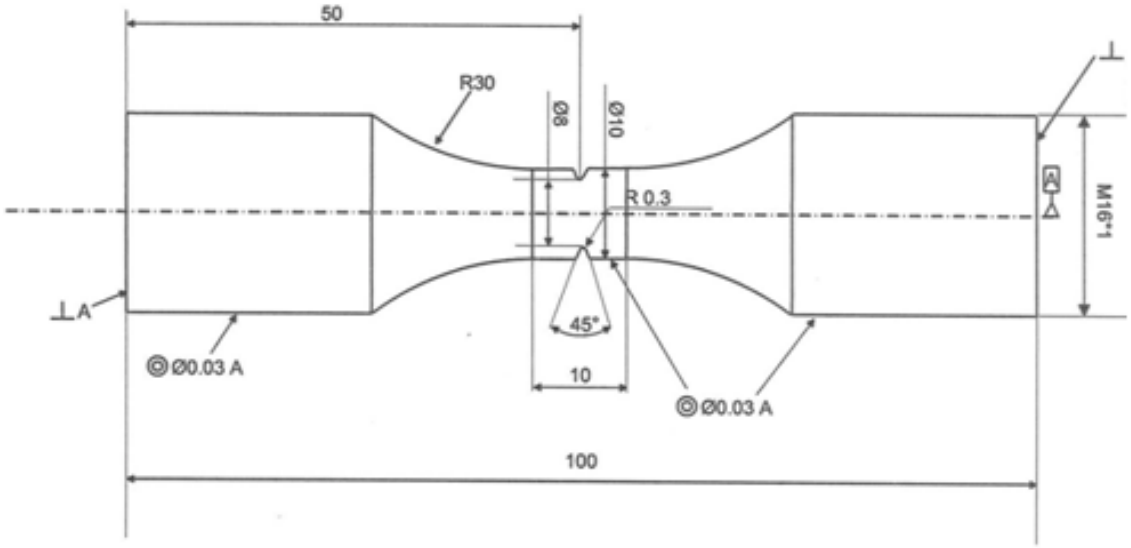

Figure 20. Geometry of notched specimen used in sulphide exposure creep testing by VTT. [18]

4 RESEARCH METHODS AND MATERIALS

The objective of this work is to find out how do the results from the double notched square creep specimens and round creep specimens differ from each other and also from the results obtained by other uniaxial and multiaxial creep testing studies. The idea is to find out, whether the amount of cold work in square specimen is non-exsistent or at least lower than in round specimen. Also the effect of sulphide exposure on the creep properties is investigated. In the next chapters the uniaxial and multiaxial testing procedures and devices are described, as well as the tools used for creep modelling and metallographic damage evaluation.

The material tested is Cu-OFP, the indicative chemical composition of which is presented in Table 4. The test bars are extracted from a base material part of the cylinder, which means that welded sections are not included here. A code of practice for conducting notched bar creep tests and for interpreting the data covers the methods of carrying out the tensile creep and stress rupture tests on circumferentially notched test pieces in order to obtain data which can be used for design and lifetime assessment purposes. The sulphide exposure creep testing procedure follows the same guideline as for the uniaxial and multiaxial creep testing. [29]

Table 4. The chemical composition of Cu-OFP (in ppm).

	Cu-OFP
Cu	bal.
P	30-100
Ag	13
S	< 8
O	< 5
H	< 0.6

4.1 Uniaxial creep testing

The uniaxial creep tests were not performed during this work, but for comparison the uniaxial tests studied by VTT for the KYT 2014 programme in 2012 and for the SKI project in 2003-2006 are included. For the uniaxial tests, standard 10 mm diameter cylindrical specimens (Figure 7) with 50 mm gauge length were used and tested in general accordance with the standard EN- 10291 (nowadays the standard is updated to the latest version SFS-EN ISO 204). Specimens were machined with the longitudinal

axis parallel to the tangential direction of the original ring section. Drawing of the uniaxial test bar is found in Appendix 1. The procedure of performing uniaxial testing is similar to the multiaxial creep testing, and is discussed more closely in the next chapter.

Table 5. The uniaxial creep testing program.[4,28]

Specimen	T (°C)	σ_{VM} (MPa)	Notes
V1	150	120	Interrupted, running
V5	120	153	Interrupted
K3	200	70	running

The uniaxial testing programme from the three projects is combined in Table 5, where σ_{VM} is the von Mises effective stress. The tests V1 and K3 are still on-going at VTT. [4] Because of the small amount of uniaxial tests made by VTT, for comparison in Chapter 5.1 Swedish uniaxial testing results are included.

4.2 Multiaxial creep testing

The multiaxial creep testing for ten specimens was performed during this work. During the tests the displacement and rupture time of the specimens in air were measured. The testing was made in accordance with the code of practice for conducting notched bar creep tests and for interpreting the data. [29] The planned testing programme for ten specimens is shown in Table 6. In Table 6 σ_{net} is the net section stress, which is determined by:

$$\sigma_{net} = \frac{4}{\pi \cdot (d_{no})^2} \cdot load. \tag{15}$$

The loads used in testing are calculated according to the net section stress. The three square specimens (y397, y400, y405) were tested at the same temperature and stresses as the three round specimens (y418, y419, y420) to see how the results differ from each other. The tests y385 and y396 as y386 and y391 were tested at the same temperature, but at different stress. The notched cylindrical creep specimens were extracted from a forged cylinder made of Cu-OFP. The tests were planned to run to rupture, unless the test lasted for an unreasonably long time. [29]

Table 6. The testing programme for the 10 specimens. O represents the round specimens and □ the square specimens.

Test code	σ_{VM} (MPa)	σ_{net} (MPa)	T (°C)	Machine
y385 O	80	133.47	175	4
y386 O	120	199.97	152	5
y391 O	110	182.34	152	5
y396 □	110	182.46	175	5
y397 □	80	132.65	250	4
y400 □	50	82.901	325	14
y405 □	40	66.318	350	14
y418 O	80	132.55	250	4
y419 O	50	82.873	325	8
y420 O	40	66.266	350	14

4.2.1 Creep testing apparatus

All creep tests in this study are made with a dead weight lever machine, which consists of five important elements (Figure 21). The main function of the tube furnace is to heat the specimen to the specific temperature and maintain the temperature within the limits. The temperature controller (manufactured by Oy Meyer-vastus Ab) adjusts the right temperature of the tube furnace. The load strains the specimen, and the displacement is measured with extensometers continuously. Four creep machines from the VTT creep laboratory were used when performing the tests: the machines 4, 5 and 8 (trademark Mayes), and 14 (trademark Denison). These machines have slightly different adjustment systems, which needs to be taken into account when inserting the sample and balancing the system.

Figure 21. The important elements of dead weight lever machines: 1) weights, 2) temperature controller, 3) spiral pole moving in vertical direction, 4) tube furnace and 5) lever arm. [37]

4.2.2 Preparation of specimens

In creep testing the number of specimens was altogether 10. The first three round specimens (y385, y386, y391) have been manufactured by turn-milling and it is possible that the bars have experienced cold work to some extent. The first specimens were just an attempt to test the possibilities to manufacture a round double notched specimen. Thus the accuracy of the specimen and notch geometry is not as uniform as with the other bars. It is also possible that these three bars had before this creep testing already been attached to a creep testing apparatus or exposed to other minor mechanical stresses. This will be taken into account when discussing the test results. Drawing of the round bars is presented in Appendix 2.

The next four square double notched specimens (y396, y397, y400, y405) were manufactured by the wire-erosion method, thus no cold work should be present in these specimens. The notches were made in octagon shape with EDM. The specimen drawing is presented in Appendix 3. In Table 7 one can see, that the dimensions from these four bars are very close to each other.

The last three round specimens (y418, y419, y420) were a better attempt to create a round double notched specimen with minimum cold work. They were manufactured by very gentle turn-milling to avoid any bending of the specimen. From Table 7 we can see that the accuracy of measures of the bars is acceptable. The testing bars were made according to the same drawing as with the earlier round specimens (Appendix 2). The notches for the round bars (also the first ones) were made by wire-erosion. The dimensions of all the specimens are presented in Table 7. The dimensions of the specimens correspond to that recommended in the code of practice for notched bar testing.

Table 7. Dimensions of the specimens.

Test code	D (mm)	L_{eo} (mm)	d_{no} (mm)	d_{no}/r_{no}	r_{no}	Notch bottom width (mm)
y385 O	9.99	-	7.94/8.07	49.61	0.16	-
y386 O	9.99	-	7.95/7.64	47.77	0.16	-
y391 O	9.445	50.14	7.05/7.41	41.01	0.172	-
y396 □	8.84	49.94	6.90/6.91	41.47	0.172	0.4285/0.4275
y397 □	8.83	49.96	6.92/6.96	41.32	0.172	0.4345/0.433
y400 □	8.84	49.99	6.91/6.91	41.26	0.172	0.4315/0.4235
y405 □	8.84	49.95	6.90/6.90	41.2	0.172	0.4245/0.4225
y418 O	10.14	44.79	6.96/6.96	40.47	0.172	0.3325/0.3285
y419 O	10.09	44.86	7.03/7.05	40.87	0.172	0.3285/0.328
y420 O	10.07	44.98	6.94/6.95	40.35	0.172	0.3265/0.3275

In Table 7, D is the diameter of parallel portion of a notched testpiece of the circular cross-section, d_{no} is the initial diameter of the testpiece at the notch plane (throat), r_{no} is the initial notch root radius, L_{eo} is the original extensometer gauge length and d_{no}/r_{no} is the notch acuity ratio. The value of r_{no} was determined only for tests y386, y386, and y391, but for the other specimens the r_{no} was assumed to be the same. It was important to remember when calculating the notch acuity ratio for square specimens with octahedral notch, that the corresponding d_{no} was calculated such that the octagon cross-section area would match the area of a round specimen with diameter d_{no}. The notch bottom width was measured to see how uniform the geometry of the notches is between different bars (slash separates the mean value for first/second notch of the specimen). As can be seen in Table 7 the notch bottom width within the same geometry is very

uniform, the difference is at maximum ±0.01 units. The critical test piece dimensions were defined according to Figure 22.

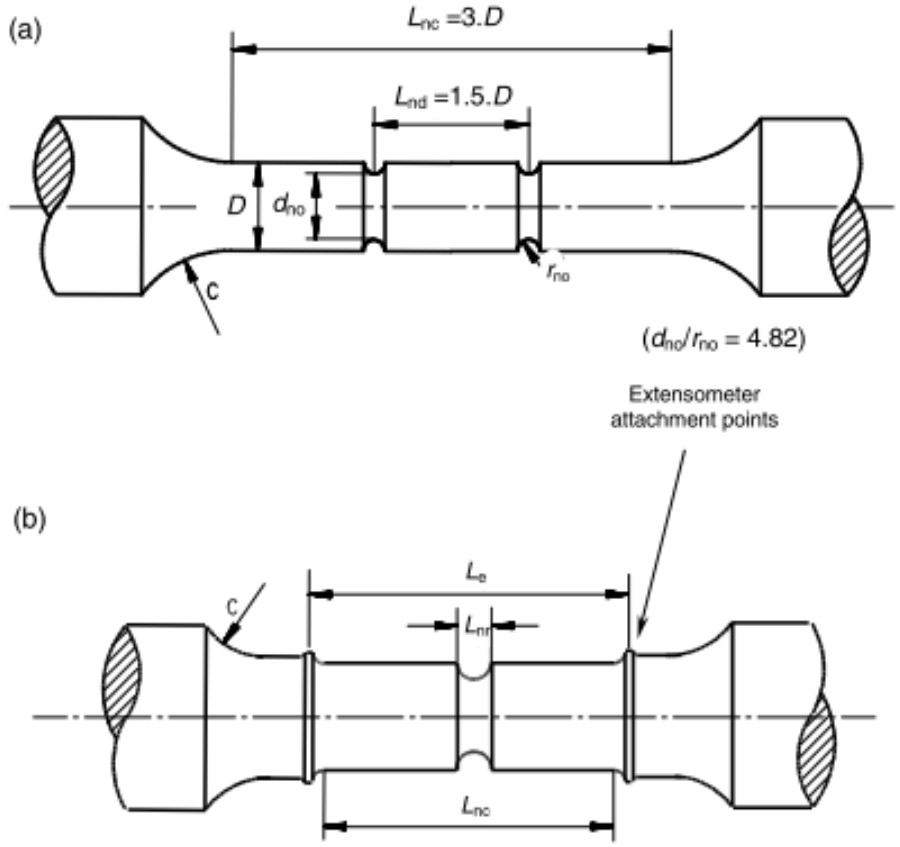

Figure 22. The testpiece measures: a) double notched and b) single notched Bridgeman type testpiece.[29]

4.2.3 Testing procedures for multiaxial creep tests

The testing procedure is the same for round and square specimens. The specimen is inserted into the creep testing machine according to Figures 23 and 24. Figure 23 shows how the ceramic extension arms and thermocouples are fitted on the specimen. Contact between the specimen and thermocouple should be as tight as possible (Figure 23, right hand side). In Figure 24 the whole measuring equipment (without thermocouple) is put to together, and few important parts are numbered and explained. Before the actual testing can start the specimen is heated to the specified temperature. The grips, loading bars, and extensometer should be at thermal equilibrium and the testing temperature should be maintained for at least one hour before the load is applied. During the heating period, the temperature of the specimen shouldn't exceed the specified temperature with its tolerances. When the specimen is inserted to the apparatus, and the force is applied along the axis of the specimen, care should be taken that bending and torsion of the specimen are minimized. The accuracy of the force should be at least ±1%. The load is applied in stepwise manner, and the displacement is recorded after each loading step to verify the linearity of the strain measurement. During the loading process the specimen

is strained by the load. When the length of the specimen changes the moving spiral pole (Figure 21) balances the lever arm. Temperature and displacement were monitored continuously and recorded at suitable interval to have 1000 measurements per test. The extensometers had a gauge length of 10 or 12 mm, which is within the standard. The displacement signals from the two extensometers were averaged. Before testing the extensometers and thermocouples were calibrated. [29]

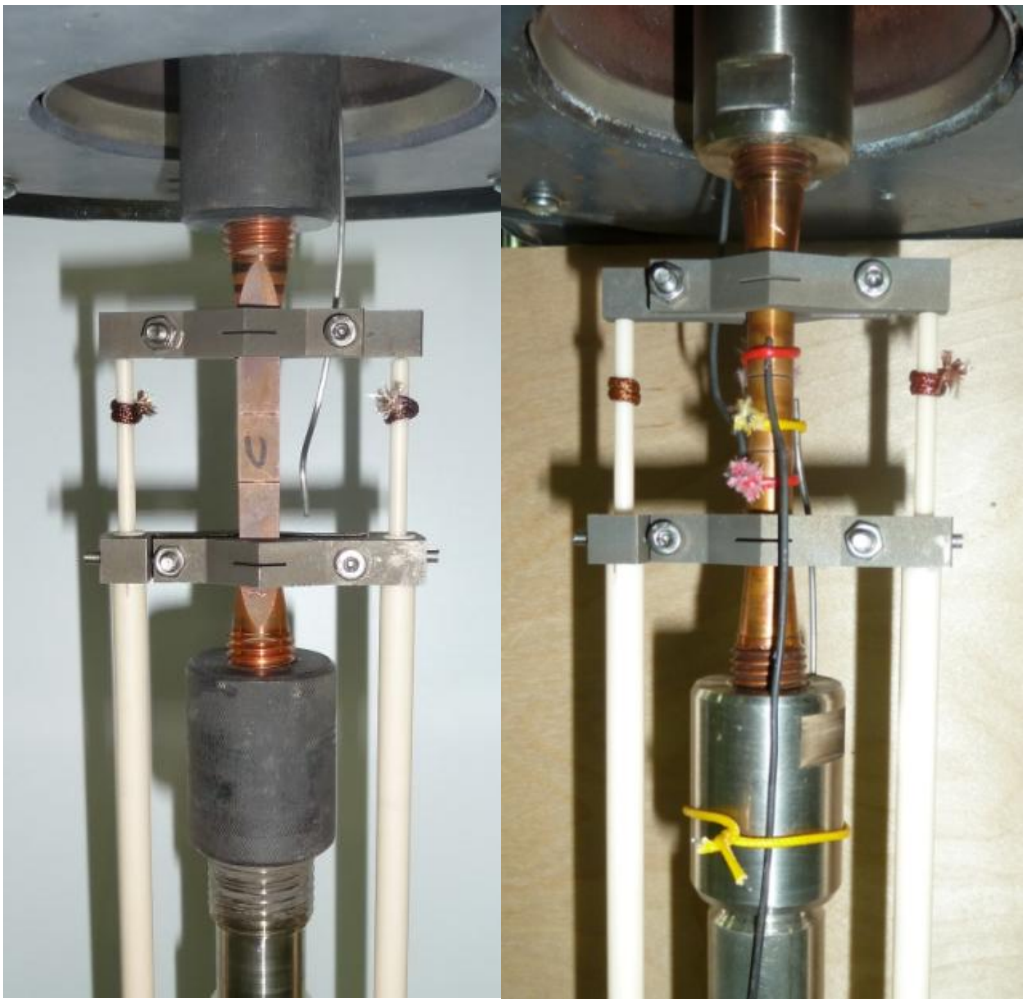

Figure 23. On the left a square specimen is inserted to the creep machine without thermocouples and on the right a round specimen is inserted with thermocouples. Ceramic extension arms are fitted on the specimen.

Figure 24. The creep testing apparatus: 1) furnace, 2) grip ends of test piece, 3) ceramic arms of the extensometer and 4) extensometer.

4.3 FE analysis of specimens

For many components creep causes stress redistribution to occur from the initial elastic or elasto-plastic stress distribution. A detailed description of how this takes place usually requires numerical analysis by computer. [29] The FE analysis in this study was done to the round and square double notched specimen geometry. The programme performs the calculations according to the simple Norton creep model:

$$\dot{\varepsilon} = B\sigma^n, \tag{16}$$

which is basically the same as Equation 1, but without the temperature term. The analysis was done for the specimen geometries at temperature of 175 °C and stress of 110 MPa. For more realistic modelling the LCSP model based FE calculations would have been a better choice, but for time saving reasons the LCSP analysis was not carried out.

The skeletal point and the corresponding skeletal stresses (the mean stress σ_m^*, the maximum principal stress σ_1^*, and the effective stress σ_{VM}^*) were determined with the help of the FE analysis. Also the normalised values of the skeletal stresses for the specific notch acuity ratio were calculated (σ_m^*/σ_{net}, σ_1^*/σ_{net} and $\sigma_{VM}^*/\sigma_{net}$). The multiaxiality parameters *H* and *h* were determined as a function of normalised distance.

4.4 Metallographic damage evaluation

The post-test metallographic damage evaluation was done by light optical microscopy (LOM) to observe the creep damage within the specimens. The observations were made with Leica ME F4 M microscope for tests y396 and y397. The main interest was to see what kind of changes appears within the structure near the rupture surface and also near the bottom of the unbroken notch. After the creep testing, the specimens were longitudinally sectioned in the middle of the specimen and ground by a Stuers Tegramin-30 grinding machine. The grinding programme Stuers-copper was used and after that the specimens were polished with OP-S (colloidal silica suspension). The specimens were etched with a mixture of 100 ml of H_2O, 50 ml of HCl (37%) and 5 g of $FeCl \cdot 6H_2O$.

4.5 Multiaxial and uniaxial creep testing in sulphide rich groundwater

To see the influence of different kind of environment on the creep properties, the results from the creep specimens exposed to sulphide rich groundwater are investigated. The experiments discussed here were performed by a research group at VTT for KYT 2014 programme (the CUHA project). Two kinds of creep tests were performed during the project: the in situ (multiaxial) and ex situ (uniaxial) creep tests. The round specimens having a circumferential notch (Figure 20) were exposed to the reference groundwater (RGW) with different sulphide concentrations and simultaneously kept under constant load (the in situ tests). In the ex situ testing the unnotched creep specimens were tested in air at specific temperature after the RGW+ sulphide exposure. Both of these test procedures are explained later on.

The test material (Cu-OFP) was delivered by Posiva Ltd. In the experiments specimens were exposed for five weeks to the reference ground water (composition found in Table 8), which corresponds to Olkiluoto groundwater. Sulphide measurement was performed with a spectrophotometer (HACH LANGE DR 2800 Laboratory Analysis Spectrophotometer), which results in an accuracy of about ±0.01 mg/l of

sulphide. The pH was measured with Thermo scientific Orion 5 Star Benchtop meter. [35]

Table 8. The composition of the saline reference groundwater in anoxic condition. [18]

Element	Concentration	
	mg/l	mmol/l
Na^+	4800	208.8
K^+	21	0.54
Ca^{2+}	4000	100
Mg^{2+}	54.6	2.3
Sr^{2+}	35	0.4
B^{3+}	0.92	0.08
SO_4^{2-}	4.2	0.044
Cl^-	14500	412.7
F^-	1.2	0.063
Br^-	104.7	1.31
I^-	0.9	0.007
pH	8.2	

4.5.1 In situ loading tests

During the 5 weeks exposure the circumferentially notched specimens P1 and P3 were kept under constant load of 1.01 kN for P1 and 1.0 kN for P3. The specimen P1 (d_{no} = 8,006 mm) was exposed to RGW with a sulphide concentration of 1 mg/l and P3 (d_{no} = 8,0 mm) to RGW with a sulphide concentration of 200 mg/l. The increase of displacement during the exposure is taken as a measure of deformation, consisting of a mechanical and an environmental part. The testing was performed at room temperature. [18]

4.5.2 Ex situ creep tests

The objective of the *ex situ* (uniaxial) creep tests was to compare the creep strength between sulphide exposed and unexposed specimens. The creep tests (y358, y359, y360, y361, y362, y363) were performed with un-notched specimens in pairs at different stress levels so that the difference in creep behaviour between the exposed and unexposed specimens could be detected. The pre-test exposure time used here was 5 weeks. The *ex situ* creep tests were performed according to the standard SFS-EN ISO 204 at 215 °C. The temperature and stress levels were chosen so that the creep mechanism would speed up, but stay within the power-law creep area. The testing programme with results can be seen in Chapter 5.5 (Table 16). The sulphide surface

films on the exposed specimens were not removed before starting the creep experiments. At each stress level, one unexposed reference specimen and one pre-exposed (RGW + 200 mg/l of sulphide) specimen was tested simultaneously. [18,36,37]

5 RESULTS

In the next chapters mainly the results from the multiaxial creep tests are presented and analysed. The results from other studies made by different research groups are compared with the measured results, as well. The uniaxial creep results from VTT are presented and compared with available public uniaxial creep data. To get a better view of the deformation processes inside the specimen during creep, the FE analysis and post-metallographic evaluation are included for the multiaxial experiments. In the last chapter the results of the sulphide rich groundwater exposed uniaxial and multiaxial creep tests are being discussed and compared with the results from multiaxial tests of this work.

5.1 Uniaxial creep

The results of the uniaxial tests made by VTT are shown in Table 9. During the project specimen V1 had reached a testing time of 91 148 h (10.4 years) and a true strain beyond 10%. The test was interrupted three times for crack observation and measurement of the gauge diameter. At 63 760 h small surface cracks were observed and these cracks remained practically unchanged during the following inspections at 75 134 and 91 148 h (Figure 25). When the specimen diameter was measured, a rather uniform reduction of gauge diameter was seen over the whole gauge length without localised necking. The test K3 is running at 53 086 h. The test V5 results were taken at time 5756 h, when the test was interrupted. [4,28]

Table 9. The results for uniaxial testing programme. The tests V1 and K3 are still on-going. [4,28]

Specimen	T (°C)	Initial σ (MPa)	True σ (MPa)[1)]	Lowest $\dot{\varepsilon}$[1)] (1/h)	True ε[1)] (%)	t (h)
V1	150	120	136	2.3×10^{-6}	12.2	(91 191)
K3	200	70	-	-	-	(53 086)
V5	120	153	200	6.9×10^{-6}	27.0	5756

1) Value at the interruption, strain rate still decreasing

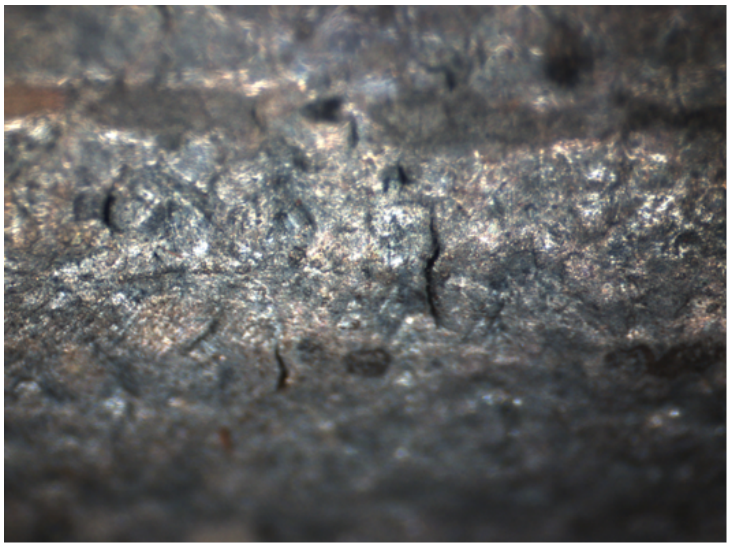

Figure 25. Surface cracks in the uniaxial specimen V1 after 91 148 h at 120 MPa 150°C. [4]

More uniaxial testing data for Cu-OFP base material for comparison was obtained from a SKB report in 2009 [10]. One testing programme and results can be seen in Table 10. The tests by SKB are made at higher temperatures than the VTT tests. Since then the Swedish test programme has used 75°C as their main testing temperature. By changing the temperature and stress, different rupture times are achieved. The difference in rupture times between VTT and SKB is quite large: the longest rupture time for SKB studies was 7 848 h whereas VTTs longest time is currently 91 191 h. The VTT uniaxial creep data compared with SKB uniaxial data is presented graphically in Figure 26 by Larson-Miller parameter. The Larson-Miller parameter is defined later in Chapter 5.2. The SKB and VTT data seem to behave similarly at higher stress, but deviate at lower stress values. [10]

Table 10. The creep test results from the 1995 study of series 400. [10]

Test ID	Copper batch	T (°C)	σ (MPa)	t_r (h)	$\dot{\varepsilon}_m$ (s^{-1})
401	400 Cu-OFP	215	120	7 848	$7{,}7 \times 10^{-9}$
402			140	1 447	$1{,}4 \times 10^{-8}$
406			160	52	$8{,}3 \times 10^{-7}$
407			150	192	$3{,}3 \times 10^{-7}$
410	400 Cu-OFP	300	100	220	$3{,}0 \times 10^{-7}$
415			90	622	$1{,}1 \times 10^{-7}$
416			80	1 374	$4{,}7 \times 10^{-8}$
417			70	3 635	$1{,}7 \times 10^{-8}$
411	400 Cu-OFP	450	30	195	$2{,}5 \times 10^{-7}$
412	400 Cu-OFP	250	100	4 796	$9{,}9 \times 10^{-9}$
413			120	656	$1{,}5 \times 10^{-7}$
414			110	2 768	$2{,}4 \times 10^{-8}$
424	400 Cu-OFP	350	70	194	$3{,}6 \times 10^{-7}$
426			40	4 704	$8{,}1 \times 10^{-9}$
427	400 Cu-OFP	400	40	469	$9{,}7 \times 10^{-8}$
428			30	1 558	$1{,}9 \times 10^{-8}$

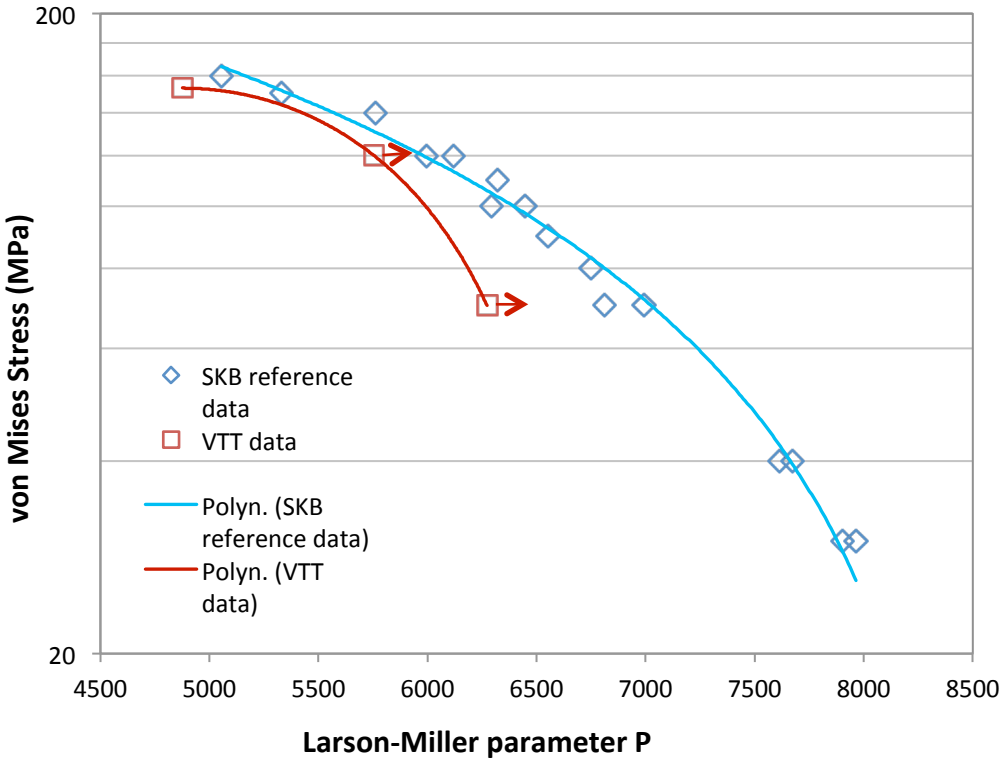

Figure 26. Von Mises stress as a function of Larson-Miller parameter for uniaxial VTT and SKB data. [4,10,28]

5.2 Multiaxial creep

The results from the ten tests performed in this study are shown in Table 11. The percentage reduction Z in the area at notch plane after creep rupture was calculated according to equation:

$$Z = \frac{A_0 - A_f}{A_0} \cdot 100\%, \quad (17)$$

where A_0 is the original cross-sectional area across notch throat and A_f is the minimum cross-sectional area after rupture across the notch throat (unit is mm^2). Elongation was simply determined by:

$$Elong. = L_{eu} - L_{eo}, \quad (18)$$

where L_{eu} is the final extensometer gauge length and L_{eo} is the original extensometer gauge length. A strain value in multiaxial tests cannot be presented as the gauge length in notched specimens is not defined. An example of a square specimen after rupture is shown in Figure 27.

Table 11. The results of the creep testing programme. All tests were continued till rupture except y385, which was interrupted at 1293.86 h.

Test code	σ_{VM} (MPa)	T (°C)	t_r (h)	Z (%)	Elong. (mm)	Notes
y385 O	80	175	1224	-	-	Interrupted
y386 O	120	152	580	43	-	Ruptured
y391 O	110	152	35	62.7	7.87	Ruptured
y396 □	110	175	1485	44.1	7.99	Ruptured
y397 □	80	250	457	21.3	6.15	Ruptured
y400 □	50	325	223	16.3	4.42	Ruptured
y405 □	40	350	355	9.6	3.86	Ruptured*
y418 O	80	250	744	25.4	5.27	Ruptured
y419 O	50	325	289	9.7	3.33	Ruptured
y420 O	40	350	186	9	2.4	Ruptured

*Max. temperature during heating 442 °C

Figure 27. A picture of a square specimen after the rupture.

As can be seen in Table 11, the tests have quite a lot variation in the rupture lives, due to the different testing temperatures and stresses. Though made at different testing conditions, the tests y396 (longest t_r, 1 485.4 h) and y391 (the shortest t_r, 35.2 h) stand out. The test y385 would probably have lasted the longest time, if it hadn't been interrupted. The tests y397 and y418, y400 and y419, y405 and y420 were carried out as pairs at the same stress and temperature. The difference in rupture lives between round and square specimens can be due to the milling of the last three round specimens. The test y396 had the highest value of rupture elongation. Also the specimen y391 had a high value of rupture elongation (and the highest reduction in area), and the shortest rupture time.

The temperature was measured constantly during the tests. The temperature-time diagram for the test y386 can be seen in Figure 28. Normally for the other tests the temperature stayed constant within ±0.5 °C. The measured displacement-time diagram for test y386 is presented in Figure 29. The series 1 and 2 represent the signals from the two extensometers. The displacement-time diagrams for the rest of the tests are found in Appendix 4. In the displacement diagram for the test y400 (Figure 74) can be seen a malfunction of one of the extensometers. The balancing of the lever arm results in a new primary creep deformation as shown in Appendix 4 for tests y385, y396 and y397.

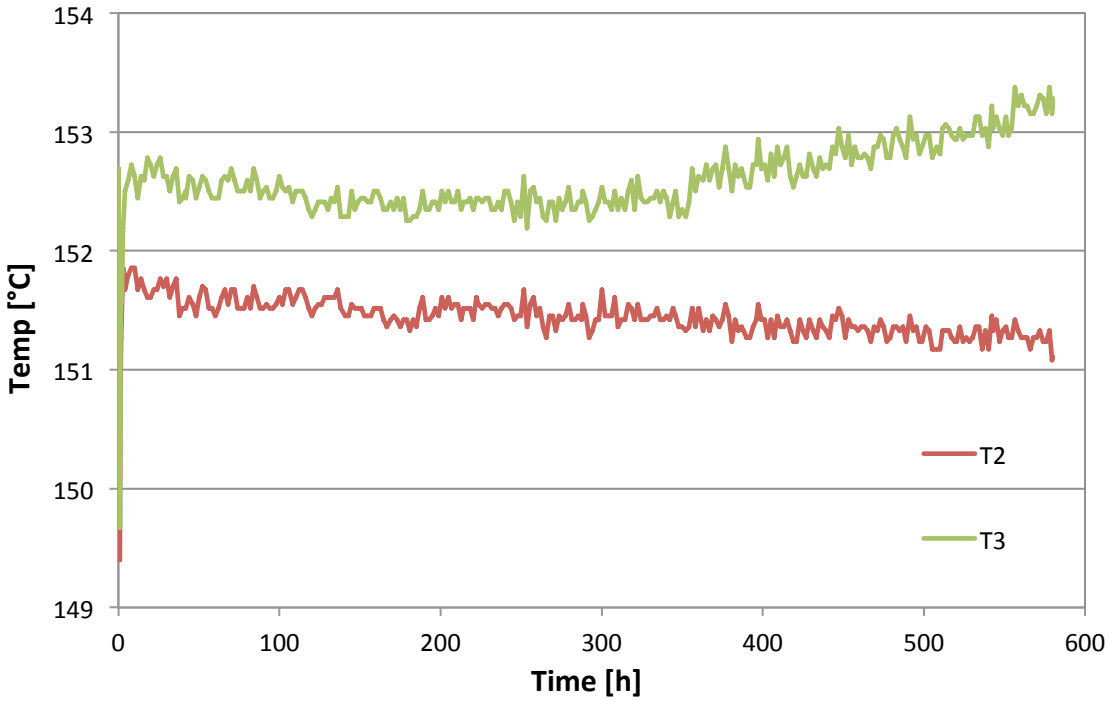

Figure 28. The temperature-time diagram for test y386.

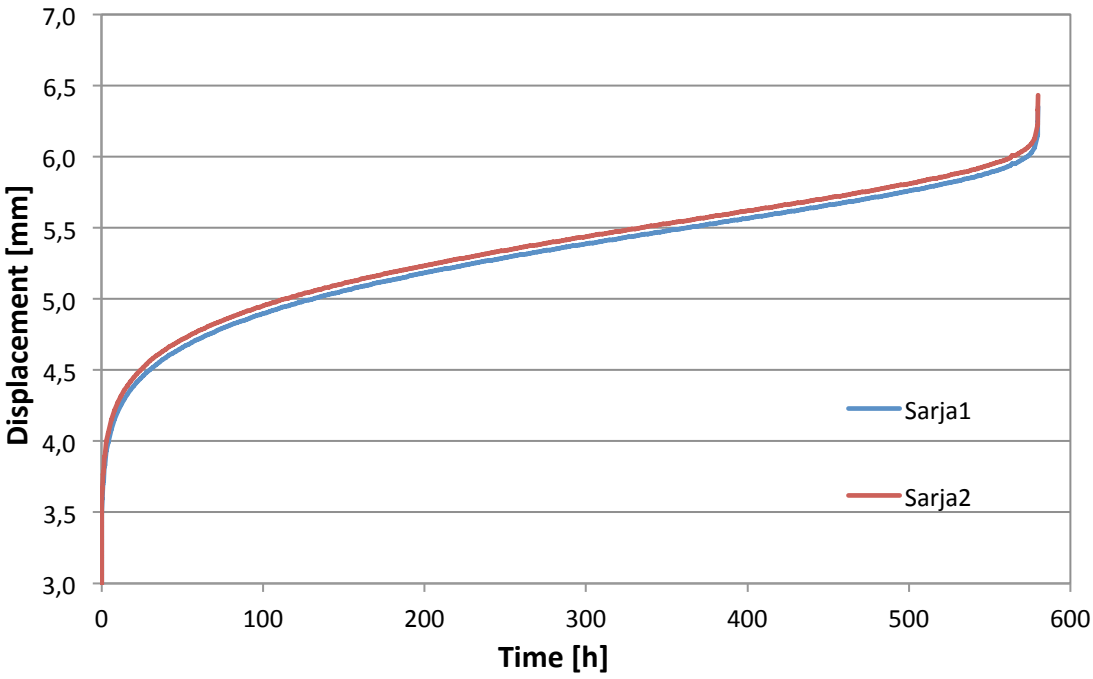

Figure 29. The displacement-time diagram for test y386.

The combined average displacement-time diagram of the tests is presented in Figure 30. The effect of cold work should influence the amount of plastic strain during loading when the specimen experiences work hardening. Studies show that the initial plastic and primary creep strain is much smaller in the cold worked specimens [5]. A close up of the displacement in the primary creep stage is presented in Figure 31. The tests performed at the same temperature are coloured with same colour. When comparing the initial plastic and primary creep strains between the tests performed at the same

temperature (y386 and y391; y385 and y396; y397 and y418; y400 and y419; y405 and y420) it can be seen that the biggest difference is between specimens y385 and y396. Here it seems clear that y385 has experienced much more cold work than y396 before testing. The test y396 was performed at higher stress than y385 (110 MPa vs. 80 MPa), which also has had an effect. The tests y386 and y391 were also performed at slightly different stress (120 vs. 110 MPa). The difference between the other couples is about 0.5-1 mm, highest for y400 and y419 and for y397 and y418 and lowest for y405 and y420 and for y386 and y391. It seems that the difference in strain is the biggest when comparing the results of square and round specimens. It could be concluded that four square specimens have experienced a smaller amount of cold work before testing (if any) than the round specimens, since the strain curves after initial plastic strain of the round specimens (dashed curves) are always beneath the square curves (solid curves) for the tests performed at the same stress and temperature. The difference between the three first round specimens and square specimens seems to be bigger than the difference between square and last round specimens. For the test y385, which had quite low initial plastic strain, the pre-test history was uncertain. It is possible that this specimen had been pre-strained in the past since the specimen was a left-over from a previous test programme and the testing history was not documented properly. The average displacement as a function of normalised time is presented in Figure 32.

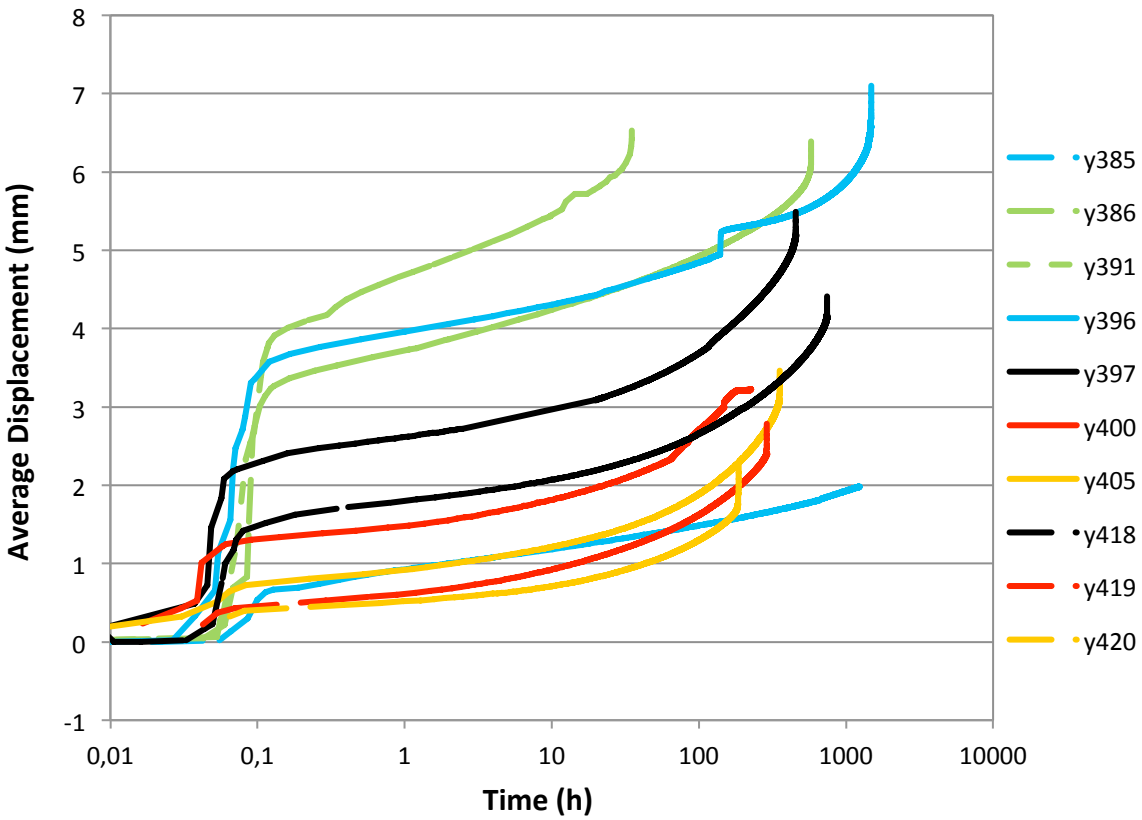

Figure 30. The average displacement-time diagram for all the tests. The "tail" at the left side of the picture is the step-loading stage, during which the loads are added in step-wise manner.

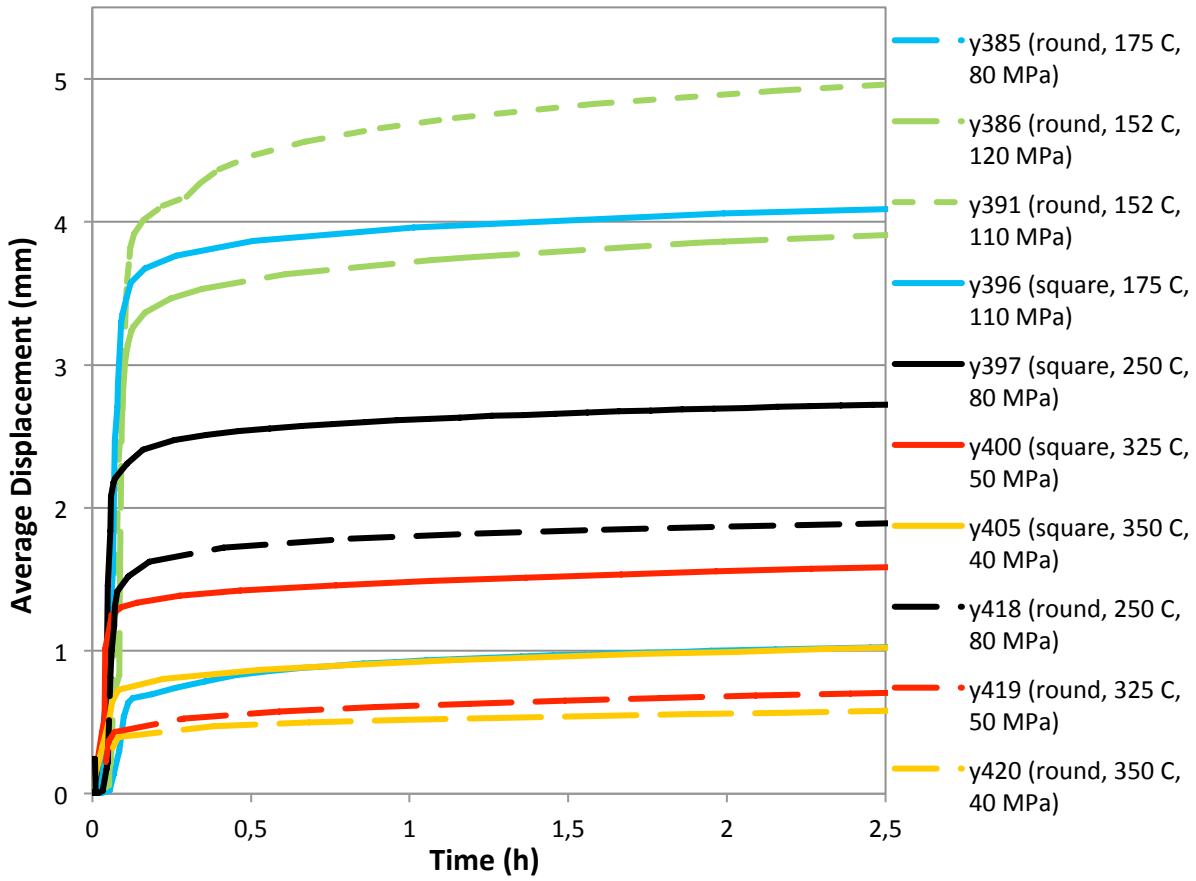

Figure 31. A close up of the beginning (primary creep phase) of the average displacement-time diagram. The tests performed at the same temperature are coloured with the same colour.

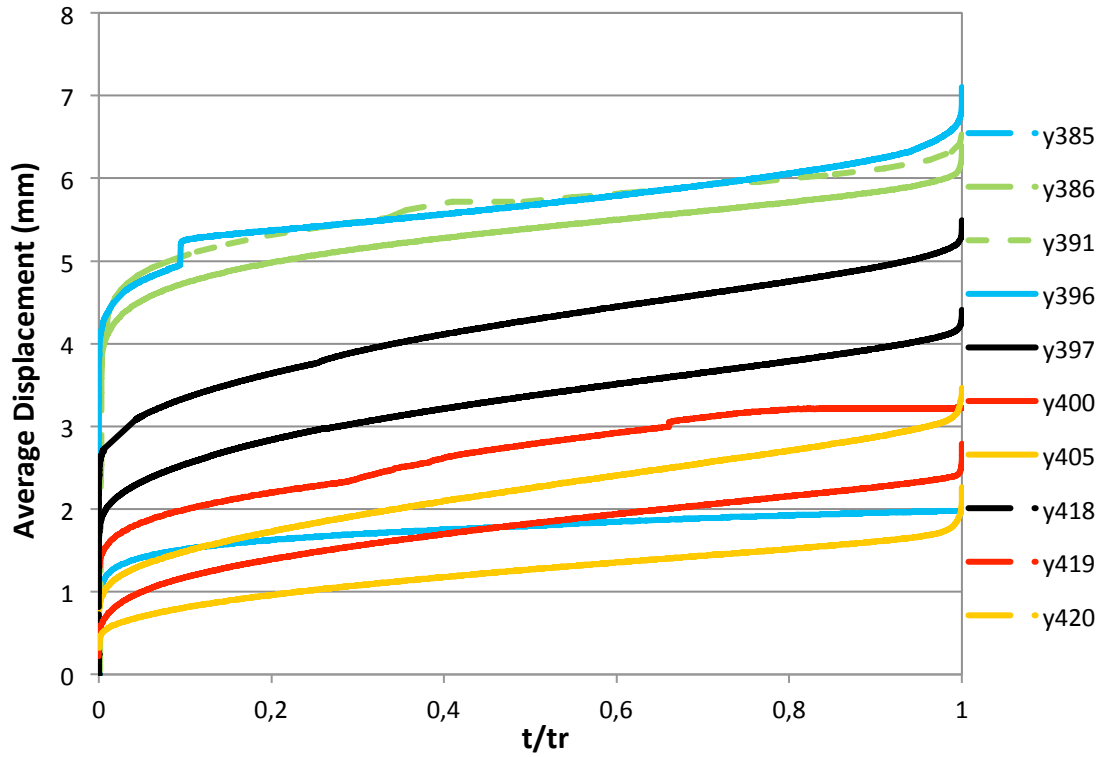

Figure 32. The average displacement (mm) as a function of normalised time.

The results from Table 11 are presented graphically in Figure 33 with von Mises stress as a function of Larson-Miller parameter (time-temperature parameter). The Larson-Miller parameter P is calculated:

$$P = T \cdot [\log t_r + C], \tag{19}$$

where T is temperature in Kelvin and C is a material constant. A constant value of 8.64 is used for the Cu-OFP. This value was determined with the help of VTT DESA software, which optimizes the parameter C to fit the test data. In Figure 33 it seems that the test values follow the prediction in rather satisfactory manner. The predicted values are calculated based on the available creep data by a VTT creep modelling expert. The interrupted test y385 deviates from the curve. If the test y385 would have been continued till rupture, it probably would have followed the curve as well. In Figure 34 the square specimens are compared with the first set and the last set of round specimens. The first set of round specimens is clearly less similar than the square specimens and the last round specimens. This is due to the undefined manufacturing history of the first three specimens.

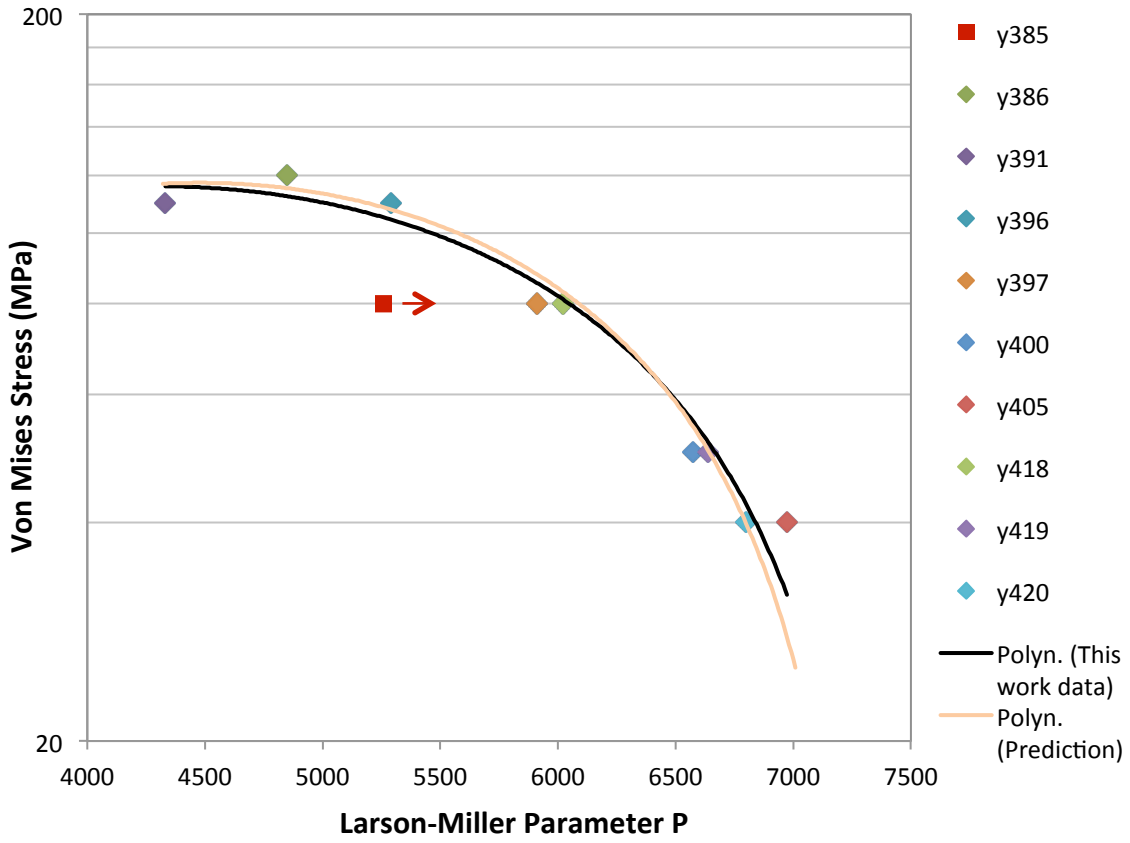

Figure 33. Von Mises stress as a function of Larson-Miller time-temperature parameter. A predicted behaviour is also added. The test y385 (175°C, 80 MPa) was an interrupted test.

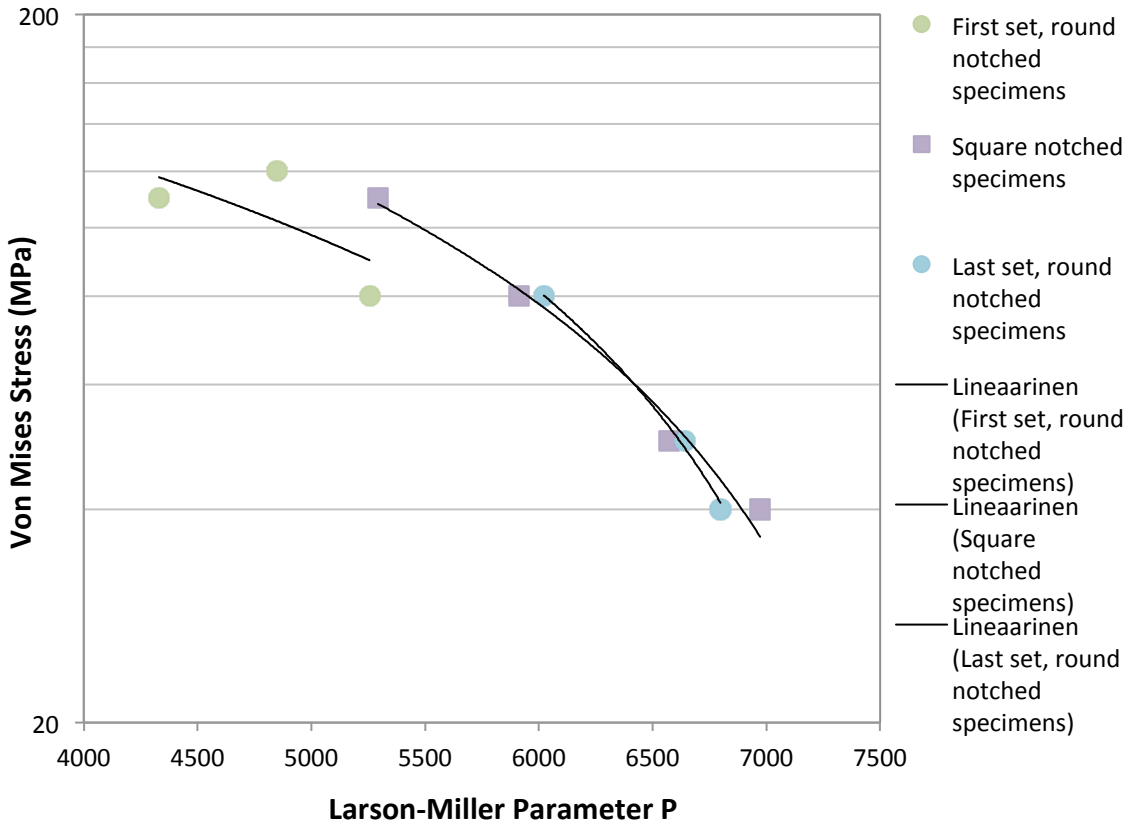

Figure 34. Comparison of the square specimens with first and the last set of round specimens.

For comparison the results from the Swedish SKB multiaxial creep report mentioned earlier in Chapter 3.1.3.3 are presented in Table 12. In the report notch acuity is determined as a/r_{no}, where a is the radius of the specimen at the base of the notch position, and equals d_{no} divided by two. Instead of the von Mises stress, the net section stress is used. As already discussed in Chapter 3.1.3.3 the SKB report claims that the notches extend the creep lifetime of the specimen, which is in contradiction with the earlier studies by VTT and this thesis study. The possible reasons for this contradiction were discussed earlier. The SKB tests have much longer testing times (most of them over 10 000 h) than the ten tests performed in this study (the longest testing time 1 485 h). The difference between the results is likely to be due to the difference in the testing temperature and notch acuity ratio. The Finnish specimens (round and square bars) had the notch acuity ratio value of 40- 50 in the beginning of testing, whereas the Swedish specimens had notch acuity ratio of 0.5- 18.8. The value 18.8 is already close to the thesis values. Also the difference in determination of the notch acuity ratio and the amount of interrupted tests may influence the results. The manner of displaying the results (use of net section stress or von Mises stress) affects the final conclusions. [12]

Table 12. The multiaxial creep testing results of copper at 75°C in SKB report. [12]

Specimen ID	r_{no} (mm)	a/r_{no}	σ_{net} (MPa)	Interrupted/ t_r (h)	σ_{VM} (MPa)	Comment
Cu-0.5-1	5.64	0.5	170	16 782	146.2	Interrupted
Cu-0.5-2			180	12 148	154.8	Interrupted
Cu-0.5-3			200	1 133	172	Ruptured
Cu-0.5-4			215	8	184.9	Ruptured
Cu-0.5-5			195	2 492	167.7	Ruptured
Cu-2-1	1.41	2	170	16 107	125.7	Interrupted
Cu-2-2			180	12 145	133.1	Interrupted
Cu-2-3			200	13 551	147.9	Interrupted
Cu-2-4			215	15 417	159	Ruptured
Cu-2-5			230	565	170.1	Ruptured
Cu-2-6			225	685	166.4	Ruptured
Cu-5-1	0.56	5	170	16 107	112.2	Interrupted
Cu-5-2			180	11 949	118.8	Interrupted
Cu-5-3			200	13 550	132	Interrupted
Cu-5-4			215	9 701	141.9	Interrupted
Cu-5-5			230	7 149	151.8	Running
Cu-5-6			245	20	161.7	Ruptured
Cu-18-1	0.15	18.8	230	7 146	139.2	Running
Cu-18-2			240	6 526	145.3	Running
Cu-18-3			255	147.5	154.3	Ruptured

The results of this work and the SKB report (Table 12) are compared graphically in Figure 35 with the help of Larson-Miller parameter. To transform the SKB net section stress values to von Mises stresses, a conversion had to be done. To get the von Mises stresses, net section stress needed to be multiplied with stress ratio (or normalised skeletal stress) y, which was determined:

$$y = e^{\left[\frac{a \cdot x}{1 + b \cdot x}\right]}, \tag{20}$$

where a and b are constants (-0.169 and 0.310), x is notch acuity ratio. The same value could have been determined graphically from Figure 14 curve 1. [29] The SKB result curve seems to deviate from this work curve at high stress values. The SKB results are performed only at one temperature, so the curve isn't as representative as the curve for this work. The final behaviour of the interrupted/running tests is hard to determine beforehand.

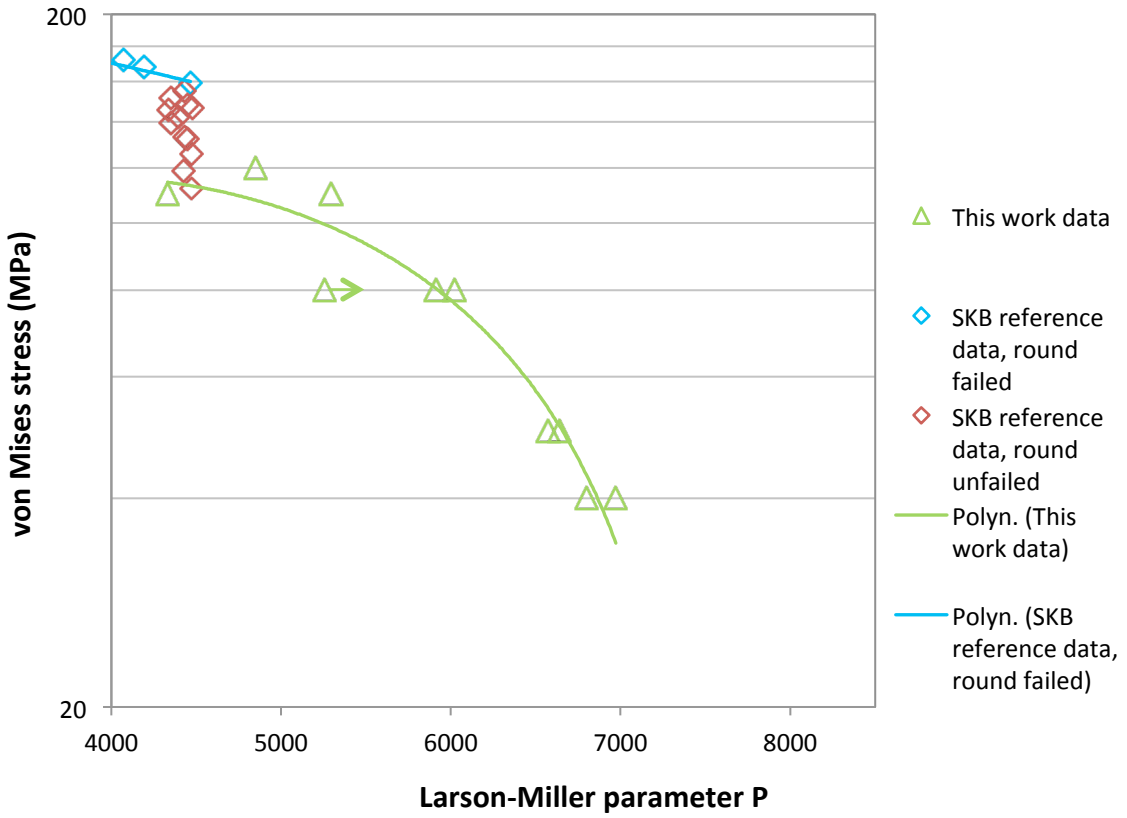

Figure 35. Von Mises stress as a function of Larson-Miller parameter. This work data compared with SKB reference data (Table 12). [12]

To see how the results behave compared to the predicted values, the Wilshire model is presented in Figure 36. In the analysis Equation 10 was used. The WE-model standard curve presents the predicted uniaxial testing behaviour while the notched multiaxial data is predicted to follow the WE-model SRF = 0.78 curve (the inversed WE-model). The strength reduction factor (SRF = 0.78) is an estimate of how much (compared to the uniaxial curve) the multiaxiality shortens the rupture time. The values used for Q^*, σ_{UTS} and k and u are shown in Table 13. For comparison test results from the Swedish SKB report (Table 12) were added into Figure 36. As can be seen the results from this work settle very well on the predicted curve. The tests y385 and y391 deviate from the curve (two green rounds, one behind the black triangles) probably due to the undefined pre-test loading history. The test y385 differs more than y391, which is reasonable, since y385 was an interrupted test. The predicted multiaxial behaviour curve is below the predicted uniaxial curve, which indicates that multiaxial tests rupture faster than uniaxial tests.

Table 13. Wilshire equation parameters for the inversed model: the apparent activation energy Q, the ultimate tensile strength σ_{UTS} and constants k and u obtained from the test data. Unit for T is °C.*

WE-model inversed	Value
Q*	95000 J/mol
k	21.867
u	0.282
σ_{UTS}	(216-0.339 ·T) MPa

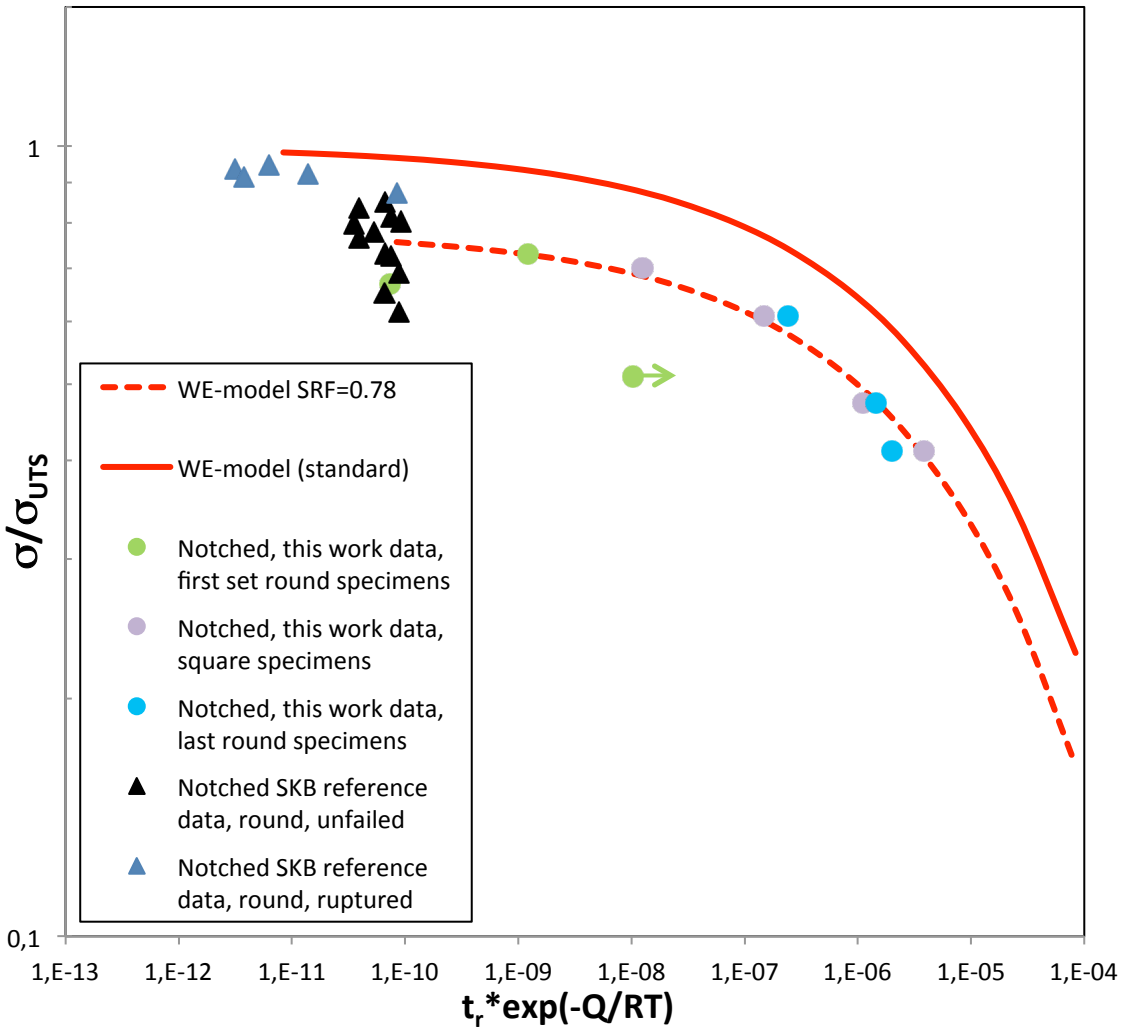

Figure 36. The Wilshire model presentation for this work data and the SKB reference data (Table 12).

The fitting efficiency of the selected model is described by the scatter factor *Z*: the smaller the scatter factor *Z*, the better the model. In a creep rupture assessment, a scatter factor close to 2 is considered to be good. A fit giving *Z* values of > 4 is according to ECCC recommendations unacceptable, whereas values of 3–4 are marginal, but may be regarded as practically acceptable. *Z* is determined as:

$$Z = 10^{2.5 \cdot \sqrt{\frac{\sum(\log n_{pd} - \log n_{md})^2}{n-1}}}, \quad (21)$$

where n is the number of data points, and the subscript *pd* means predicted data and *md* measured data. The calculated Z for the Wilshire model SRF = 0.78 is shown in Figure 37. The value 3.2 is acceptable, thus the Wilshire model SRF = 0.78 fit can be considered satisfying. In the calculation the data points y385 and y391 were dismissed, since y385 was an interrupted test and y391 behaved in a very unusual manner (t_r = 35 h). A normal distribution of t_r should lie (when the exponent of 10 is 2.5) in almost 99% of the observed times within the boundary lines defined by the scatter factor Z (Figure 37, dashed lines). The middle line in Figure 37 is $Z = 1$. In general, the closer to $Z = 1$ line the better the agreement between the predicted and measured values. [22,38]

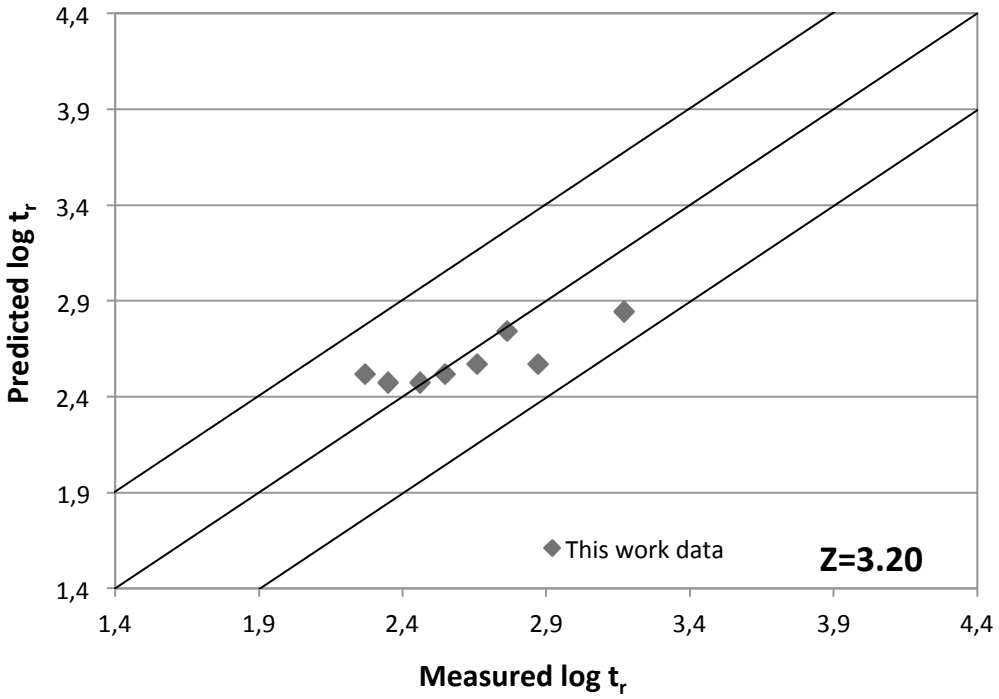

Figure 37. The predicted log t_r (from Wilshire model SRF=0.78) as a function of measured log t_r from this work data.

5.3 FE analysis of specimens

The FE analysis was carried out with ABAQUS programme for the round and square geometry at temperature of 175 °C and stress of 110 MPa. The mesh for the round and square specimen is presented in Figures 38-39. In the Norton (Equation 16) analysis the deformation rate of the specimen speeds up towards infinite at the time of 740 h for square geometry and 1185 h for round geometry, which explains the chosen time periods in pictures. The equivalent creep strain (CEEQ) of the round specimen after 1185 hours is presented in Figure 40. It can be seen, that the highest value of CEEQ

(approximately 188.2 %) is located close to the notch root. For the square geometry (Figure 41) the maximum CEEQ at 740 h is 169.6 %, and the distribution of the strain is quite similar to the Figure 40. In Figures 40 and 41 can be seen, that the equivalent creep strain distribution isn't completely symmetrical, which refers to the fact that the other notch next to it influences the strain distribution. To minimize this effect, the notches would have to be further away from each other. Figure 42 shows a cross section CEEQ view of the square specimen, showing the focusing of the highest strain value at the notch borders. Figures 41 and 42 give a quite realistic view of the deformation taking place in the specimen during creep testing.

The maximum principal stress distribution of the square geometry at 740 h is presented in Figure 43. The highest value of the maximum principal stress is 457.6 MPa, which is located close to notch bottom. In Appendix 5 it can be seen for square geometry, how the highest value maximum principal stress in concentrated on the corners of the octagon notch (time = 660 h). It seems that the corners create a locus of high stress, which is a downside for the square geometry compared to the round one. The equivalent von Mises stress of the square geometry at 740 h in shown in Figure 44. The highest values (259.4 MPa at maximum) are distributed quite symmetrically (same way as the strain in Figures 40 and 41) on both sides of the notch bottom. In Figure 44 the red coloured area (the highest values) is more spread than in Figure 43. In all the FEA figures it can be seen, that the creep deformation occurs in the area near notches as other parts of the specimen stay relatively unaffected.

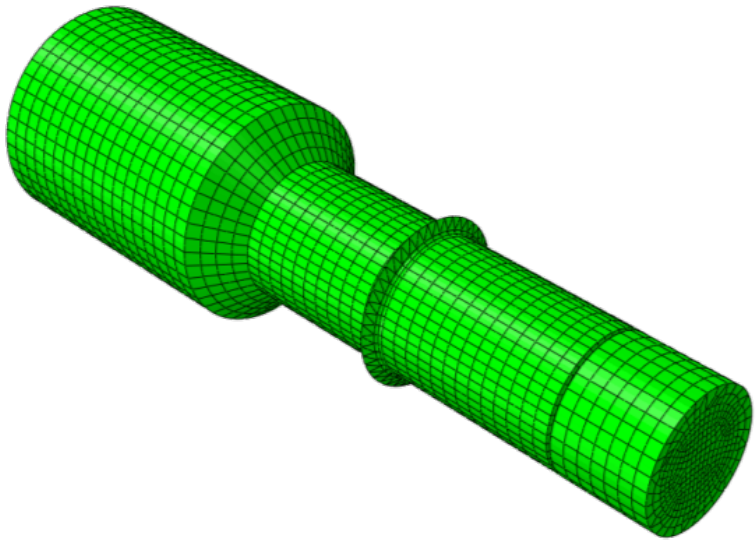

Figure 38. The round specimen mesh.

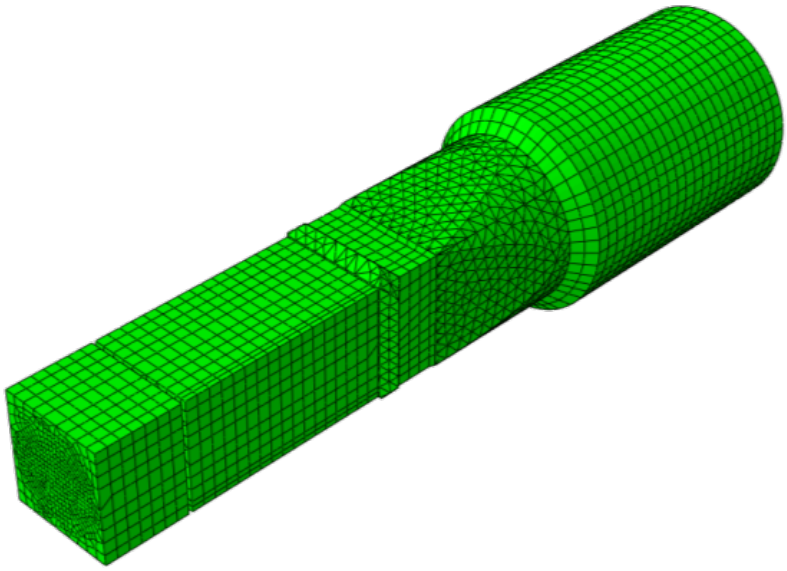

Figure 39. The square specimen mesh.

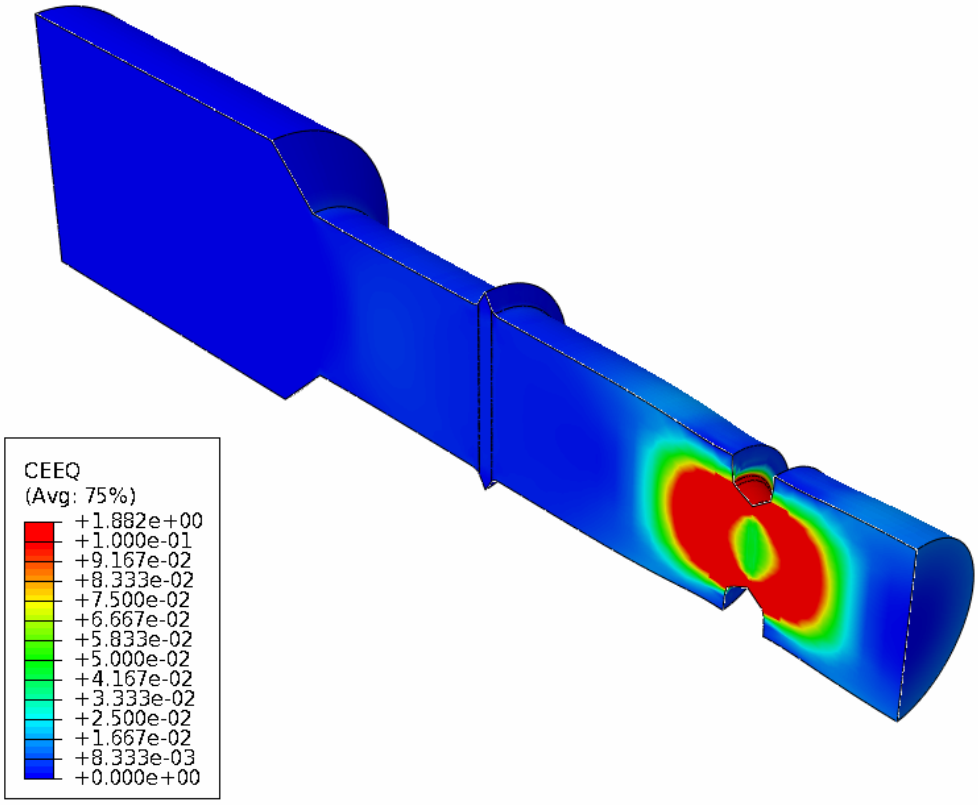

Figure 40. The equivalent creep strain of the round geometry at 1185 h.

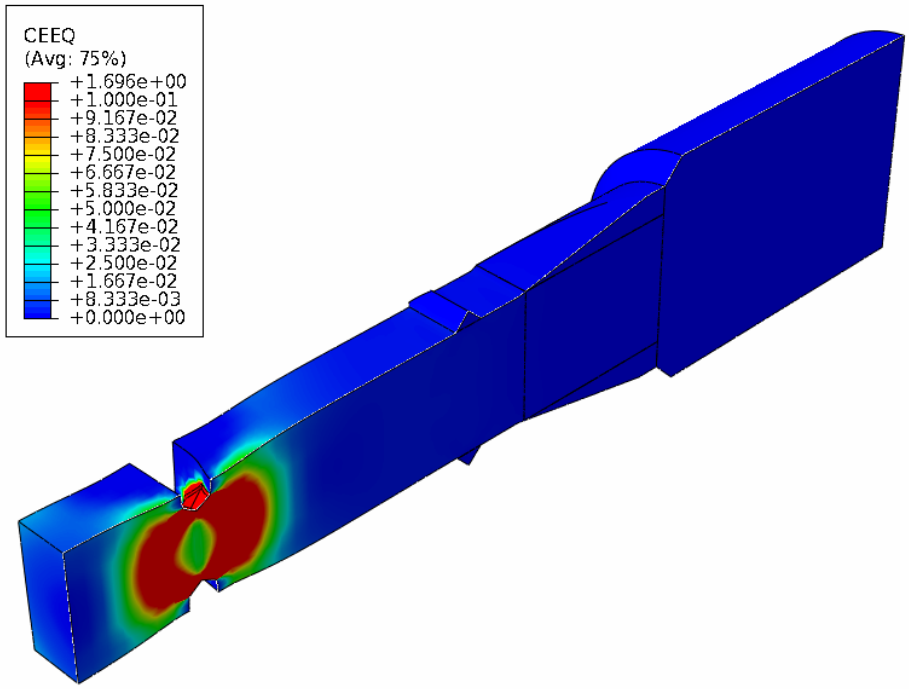

Figure 41. The equivalent creep strain of the square geometry at 740 h.

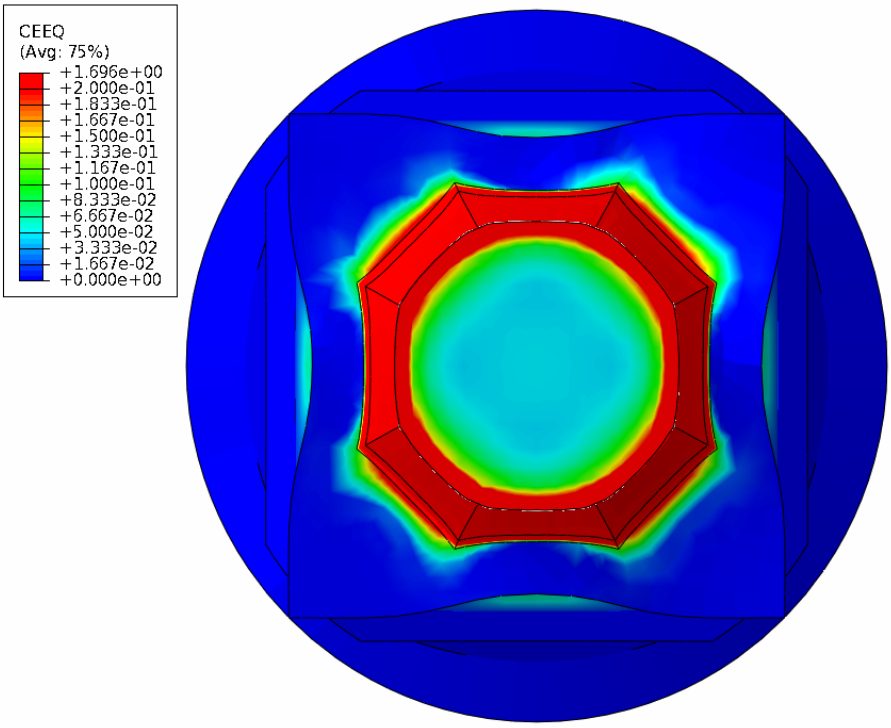

Figure 42. The equivalent creep strain of the square geometry at 740 h.

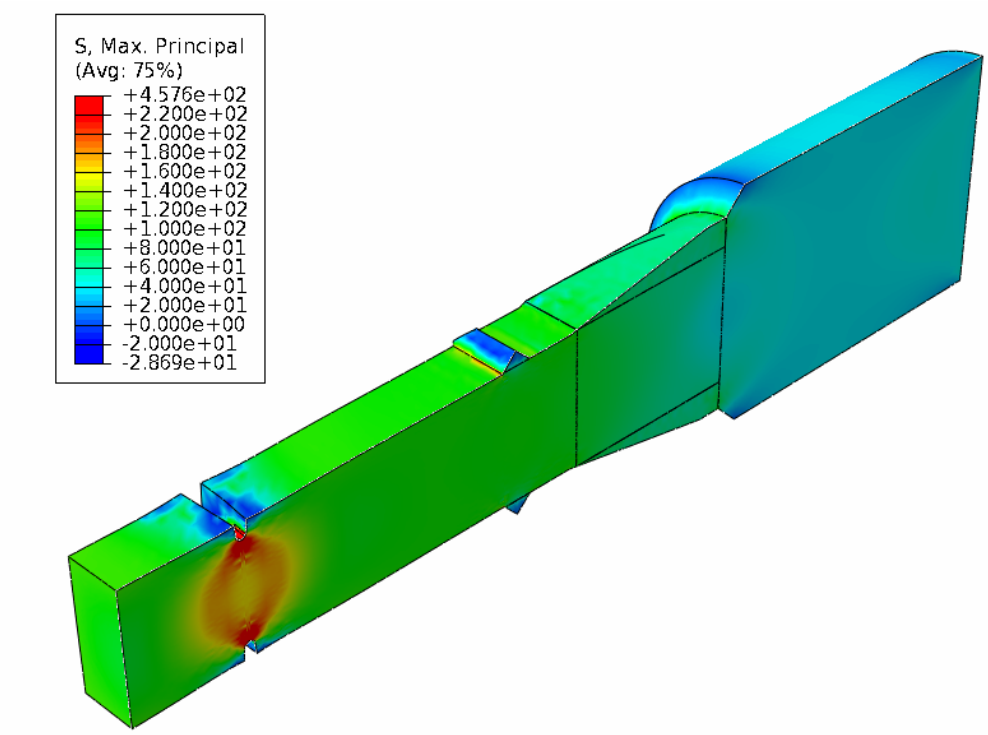

Figure 43. The maximum principal stress of the square geometry at 740 h.

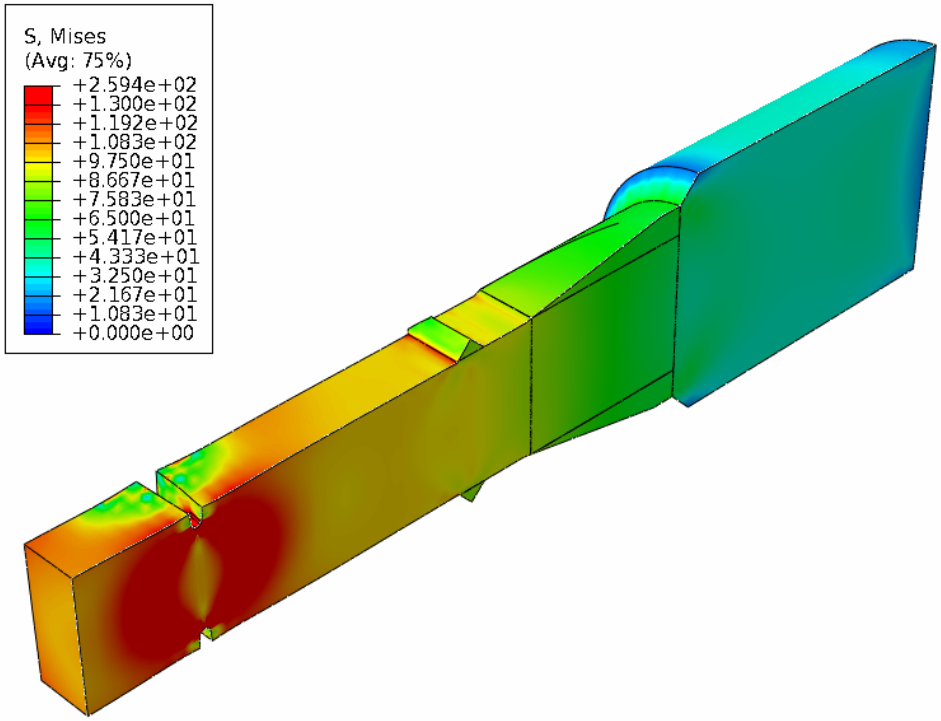

Figure 44. The Equivalent von Mises stress of the square geometry at 740 h.

According to the code of practise the normalised skeletal stresses were determined for the specimen notch acuity ratios (Table 14). Equation 20 gives the value of $\sigma_{VM}*/\sigma_{net}$, equation 22 the value of σ_m*/σ_{net} and equation 23 the value of σ_1*/σ_{net} :

$$y = c \cdot e^{\left[\frac{a}{1+b \cdot x}\right]}, \tag{22}$$

where a is -1.074, b is 0.259, c is 0.987 and x is the notch acuity ratio.

$$y = e^{\left[\frac{a \cdot x}{1+b \cdot x}\right]}, \tag{23}$$

where a is 0.02 and b is 0.049. [29]

Table 14. The normalised skeletal stresses for different notch acuity ratios according to the code of practise (D/d_{no}= 1.41). [29]

Test code	$\frac{d_{no}}{r_{no}}$	$\frac{\sigma^*_{VM}}{\sigma_{net}}$	$\frac{\sigma^*_{m}}{\sigma_{net}}$	$\frac{\sigma^*_{1}}{\sigma_{net}}$
y385 O	49.61	0.599	0.913	1.335
y386 O	47.77	0.600	0.911	1.331
y391 O	41.01	0.603	0.900	1.313
y396 □	41.47	0.603	0.901	1.315
y397 □	41.32	0.603	0.900	1.314
y400 □	41.26	0.603	0.900	1.314
y405 □	41.2	0.603	0.900	1.314
y418 O	40.47	0.604	0.899	1.312
y419 O	40.87	0.603	0.900	1.313
y420 O	40.35	0.604	0.899	1.311

With the help of the FE analysis the skeletal point and the corresponding normalised skeletal stresses were determined for notch acuity ratio value of 47.2 for the round and 45.9 for the square geometry. The determined skeletal points at normalised distance $2r/d_{no}$ are shown in Table 15. Here r is the radial co-ordinate at notch plane. An example of the skeletal point determination is shown in Figure 45 and 46. The radial position of the skeletal point is identified as s in the figures. Although this radius was not exactly the same for a given geometry for each n-value, it was found possible to define a suitably small skeletal zone in which the stresses could be identified. The maximum principal stress was chosen for the skeletal point determination instead of von Mises stress, since principal stress distribution gave more reasonable skeletal zone for sharp notches than von Mises stress. First calculations (1) were performed for n-values of 7,9 and 10.196 and the second (2) FE calculations for n-values of 5,7 and 9. The value of skeletal point for different calculations varies from 0.80 to 0.87. According to the code of practise the skeletal points for the tested notch acuities should be between 0.9-0.925. The values of normalised skeletal stresses are an average from the normalised skeletal stresses for different n-values.

When comparing the results of normalised stresses between Table 14 and 15, it seems that also quite large deviation exists. The biggest differences exists between the values of σ_m^*/σ_{net}, and the smallest between $\sigma_{VM}^*/\sigma_{net}$. When considering the differences in results, one has to keep in mind that the code of practise is not absolute when sharp notches are being used. As can be seen in Figure 45 and 46, the maximum value of σ_1 is located 0.5- 1 mm away from the notch root, not exactly at the notch root. In Figure 47 and 48 the multiaxiality parameters *h* and *H* were plotted as a function of normalised distance. Also in these pictures the highest degree of multiaxiality exists not exactly at the notch root, but 0.5-1 mm away from it. As can be seen in Figures 45- 48, some unusual behaviour exists for the curves. This is probably due to the inaccuracy of the FE calculations, and the density of the mesh used. More FE calculations are needed to receive representative results. [29,34]

Table 15. The defined skeletal points and corresponding normalised skeletal stresses for the square and round geometry. Numbers 1 and 2 refers to first and second FE calculations.

FE calculation	$2r/d_{no}$	$\frac{\sigma_{VM}^*}{\sigma_{net}}$	$\frac{\sigma_m^*}{\sigma_{net}}$	$\frac{\sigma_1^*}{\sigma_{net}}$
Square 1	0.851	0.745	1.048	1.493
Square 2	0.852	0.676	1.095	1.496
Round 1	0.866	0.789	1.241	1.718
Round 2	0.804	0.548	0.749	1.108

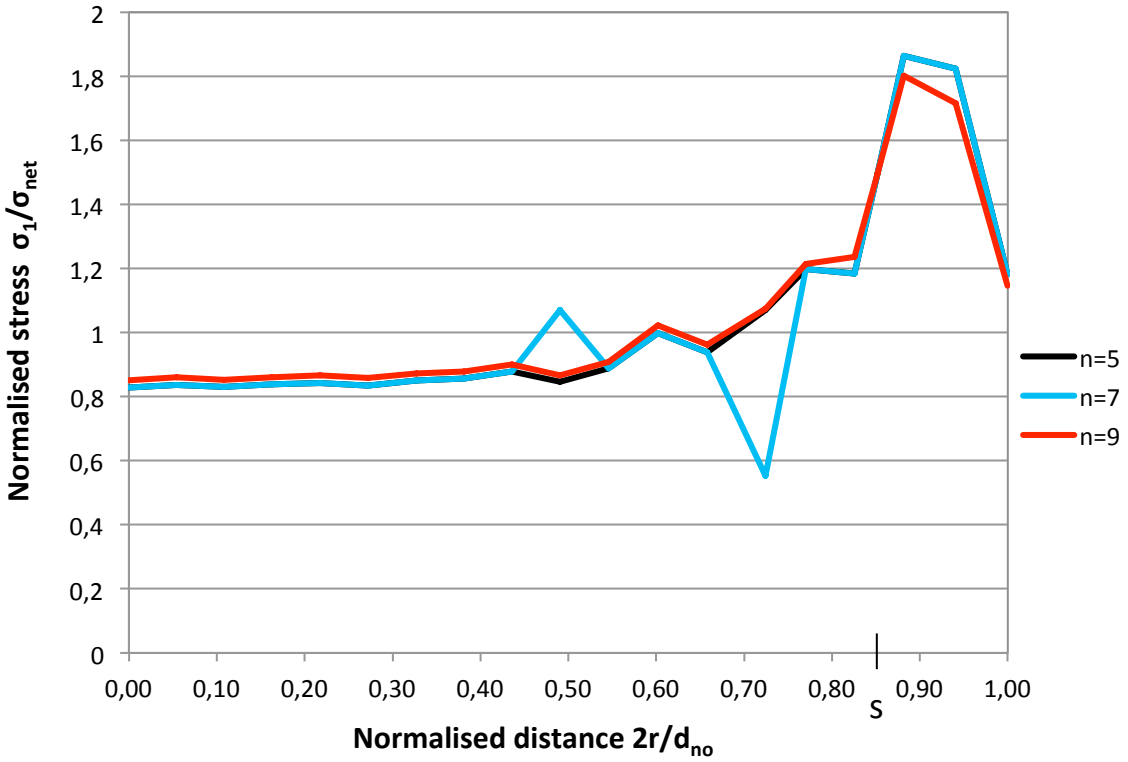

Figure 45.Determination of the skeletal point s of square specimen (second FE calculations) at temperature of 175 °C and von Mises stress of 110 MPa. Normalised principal stress distribution at steady state across the notch throat.

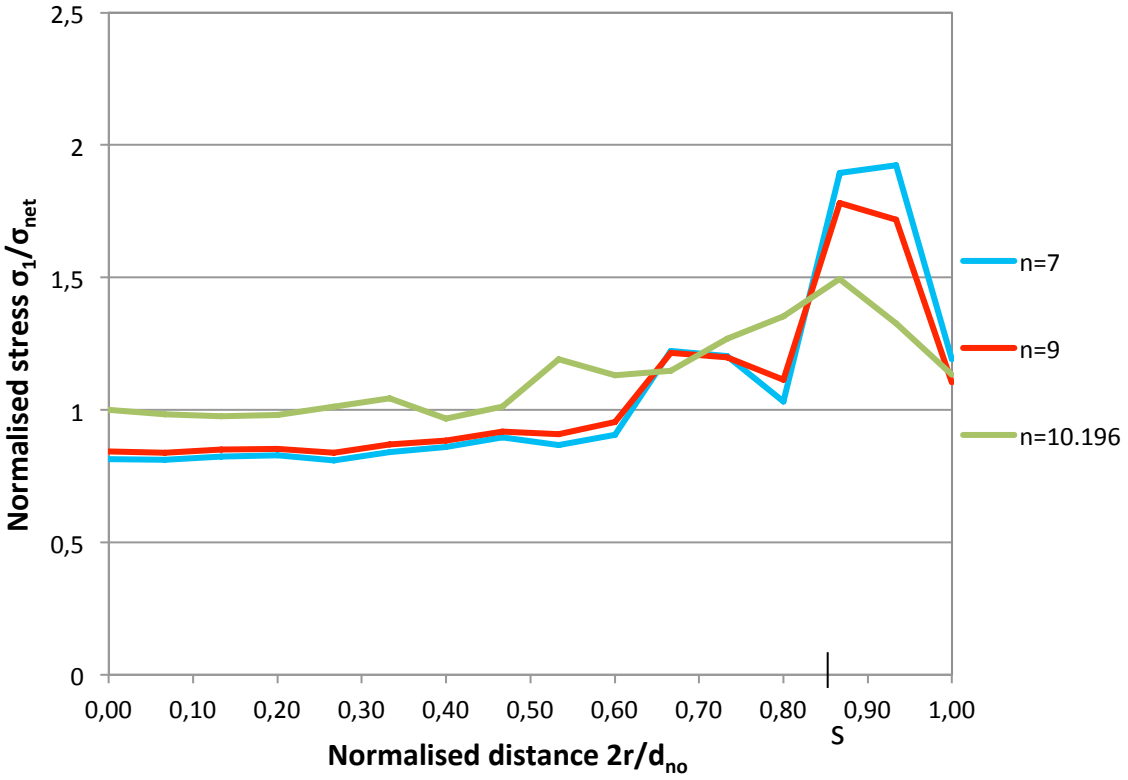

Figure 46. Determination of the skeletal point s for round specimen (first FE calculations) at temperature of 175 °C and von Mises stress of 110 MPa. Normalised principal stress distribution at steady state across the notch throat.

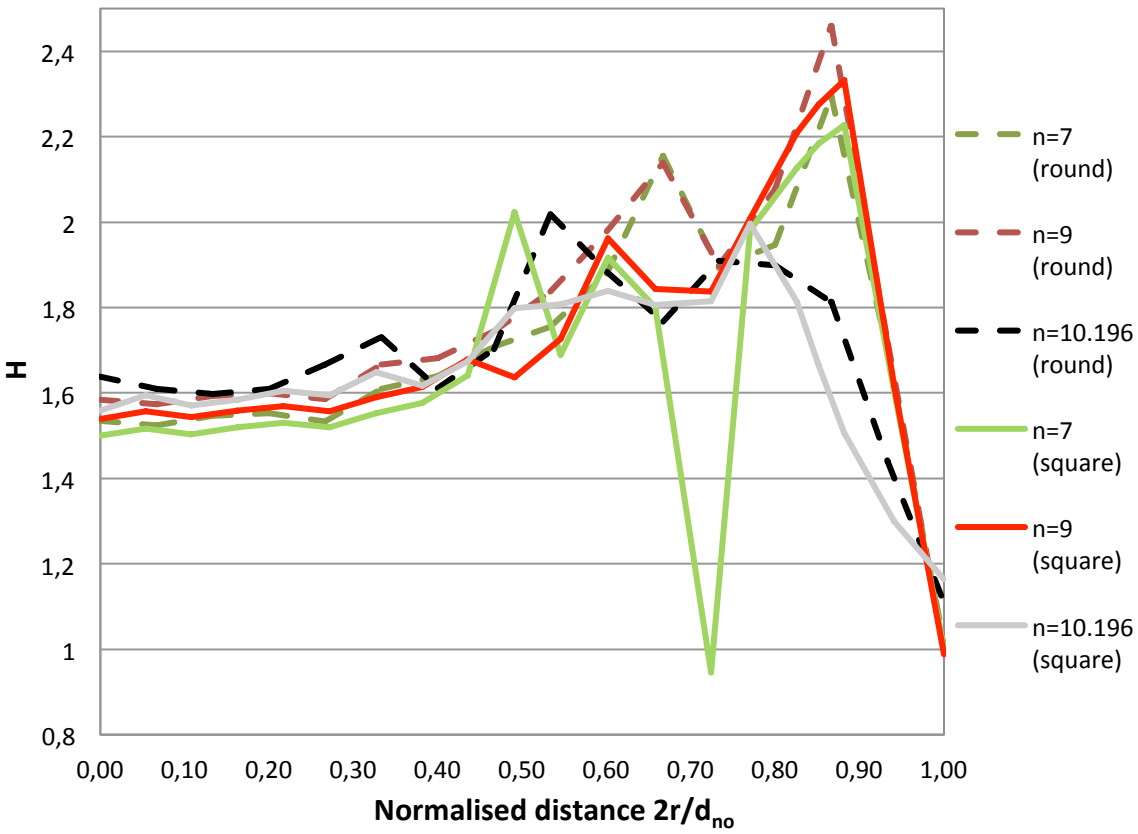

Figure 47. The multiaxiality parameter H as a function of normalised distance according to the first (1) FE calculations.

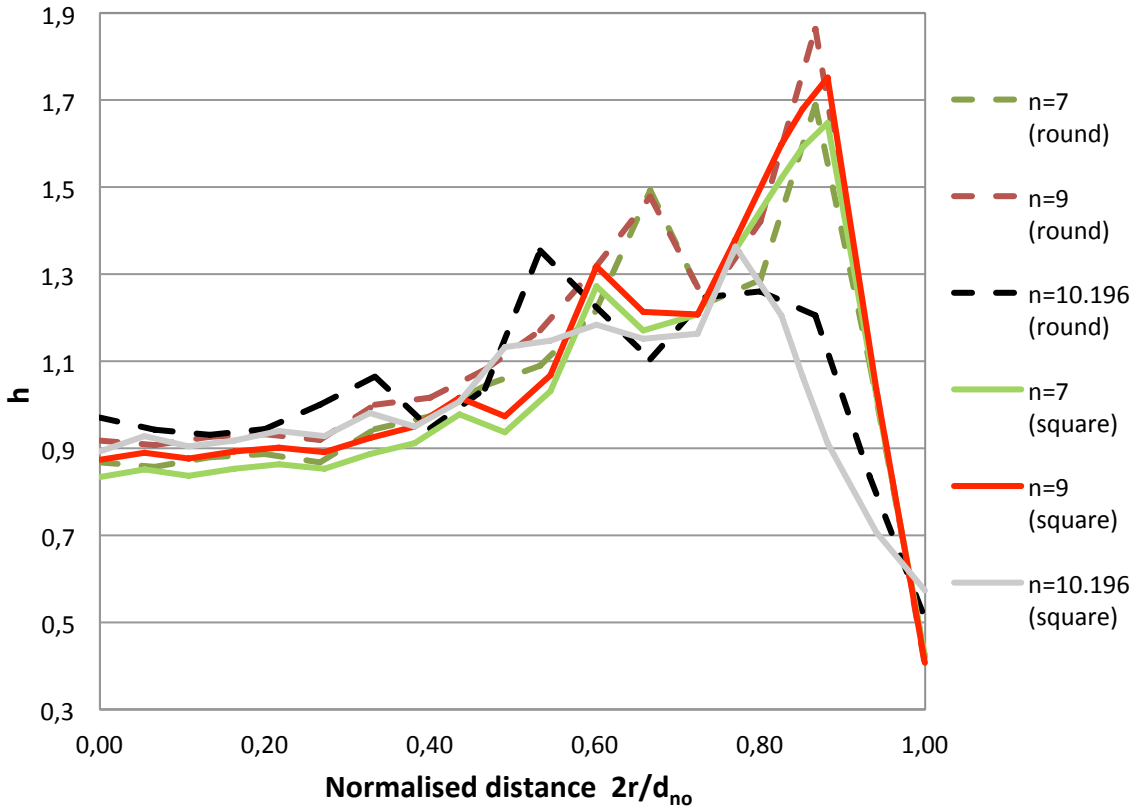

Figure 48. The multiaxiality parameter h as a function of normalised distance according to the first (1) FE calculations.

5.4 Metallographic evaluation

For the square specimens y396 (tested at 175 °C and 110 MPa) and y397 (tested at 250 °C and 80 MPa) post-metallographic evaluation was done to see what kind of behaviour occurs inside the specimens. From a square specimen a picture of the rupture surface of the notch was taken with Leica DFC 320 digital camera system to see the form of the plane of fracture (Figure 49). The approximate amount of deformation taking place inside the specimen during testing can be seen in this picture.

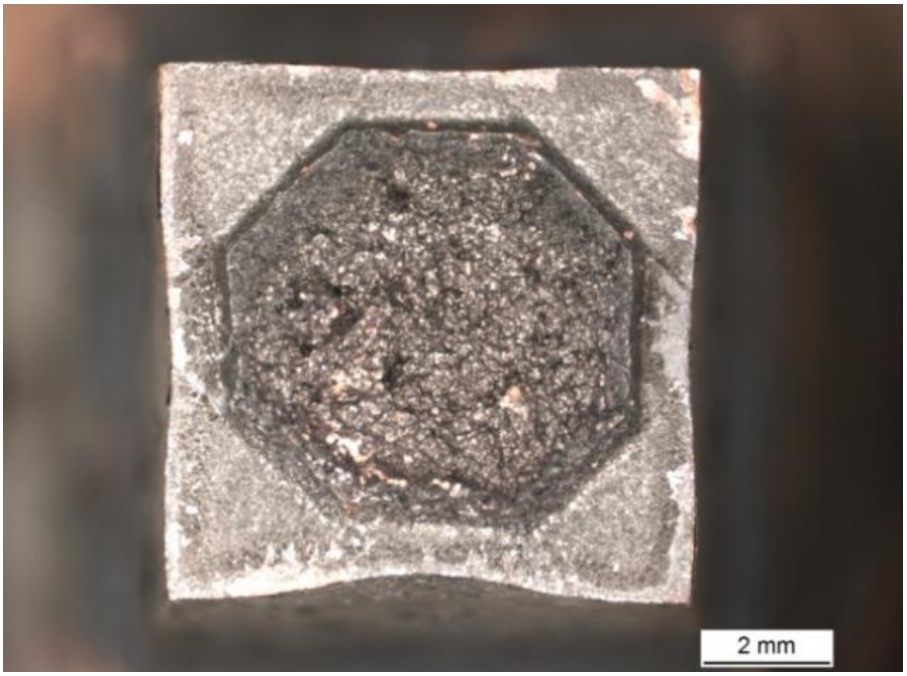

Figure 49. The rupture surface of the notch from a square specimen.

In Figures 50 and 55 cross-sections from both of the broken notches are presented. In Figure 50 the specimen y396 has deformed a lot before the final rupture on the left hand side. The crack has initiated on the right hand side. In Figure 55 y397 has much less deformation. In Figures 51 and 52 the formed cavities and the elongated shapes of the grains near the broken surfaces can be seen quite clearly. The bigger cavities have most likely occurred at the end of the test, when the specimen has strained quite fast. The smaller cavities are probably formed during the normal creep phase (at slow deformation rate). In Figures 53 and 54 the unbroken notch of the test y396 is shown. The grains are elongated near the notch bottom, on either side of the notch. Near the notch root there are also some cavities on the grain boundaries.

Figures 56 and 57 are close-ups of the middle section and the right hand side of the broken notch surface of the specimen y397. Here the deformation of the grains is not as strong as with the test y396. The same observation can be made when comparing the overview Figures 50 and 55. The cavities in specimen y397 also seem to mostly follow the grain boundaries (Figure 58). It seems that the metallographic pictures from test y397 represent the “normal” creep deformations at rupture better than test y396, since

y396 has experienced fast elongation just before the rupture. The unbroken notch in test y397 has started to crack at the notch bottom (Figures 59-62). The cracks seem to follow the grain boundaries. The FE analysis in previous chapter (Figures 42 and 43) supports the idea of cracks forming at the notch bottom, some distance away from the surface towards the specimen centre, because there the stress and strain level is the highest. According to Figures 45 and 46 it seems that the highest value of maximum principal stress should be located not exactly at the notch root, but 0.5-1 mm away from it. Cavities are also found from this area for both y396 and y397.

Generally creep cavities are thought to be nucleated either relatively early in life (when nearly all suitable nucleation sites are occupied), or continuously during creep. The local stress has to exceed a certain level before the nucleation can occur. For pure metals the expected nucleation stress would be very high but the required stress level can be reduced by impurities on the nucleating grain and phase boundaries. Nucleation is often assumed to be accelerated by local stress concentrations at grain boundary intersections on sliding grain boundaries, and the density of the cavity nuclei thereby depends on creep strain. [33]

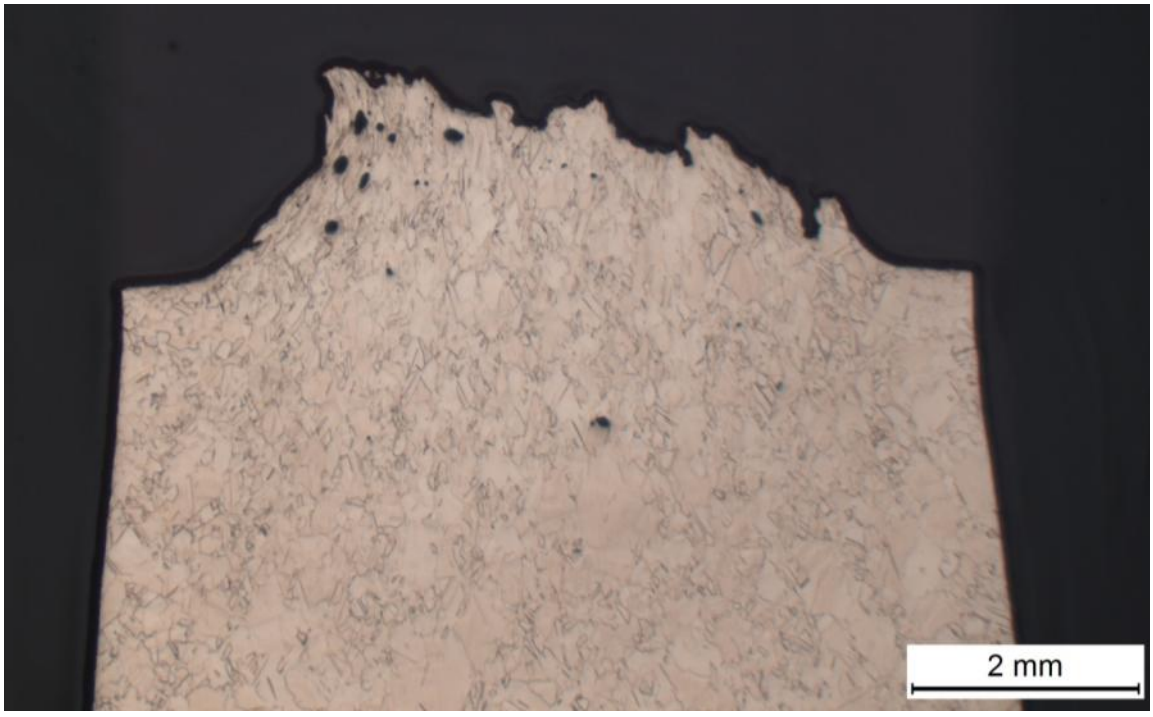

Figure 50. The broken notch of the test y396 (175 °C, 110 MPa, 1485 h).

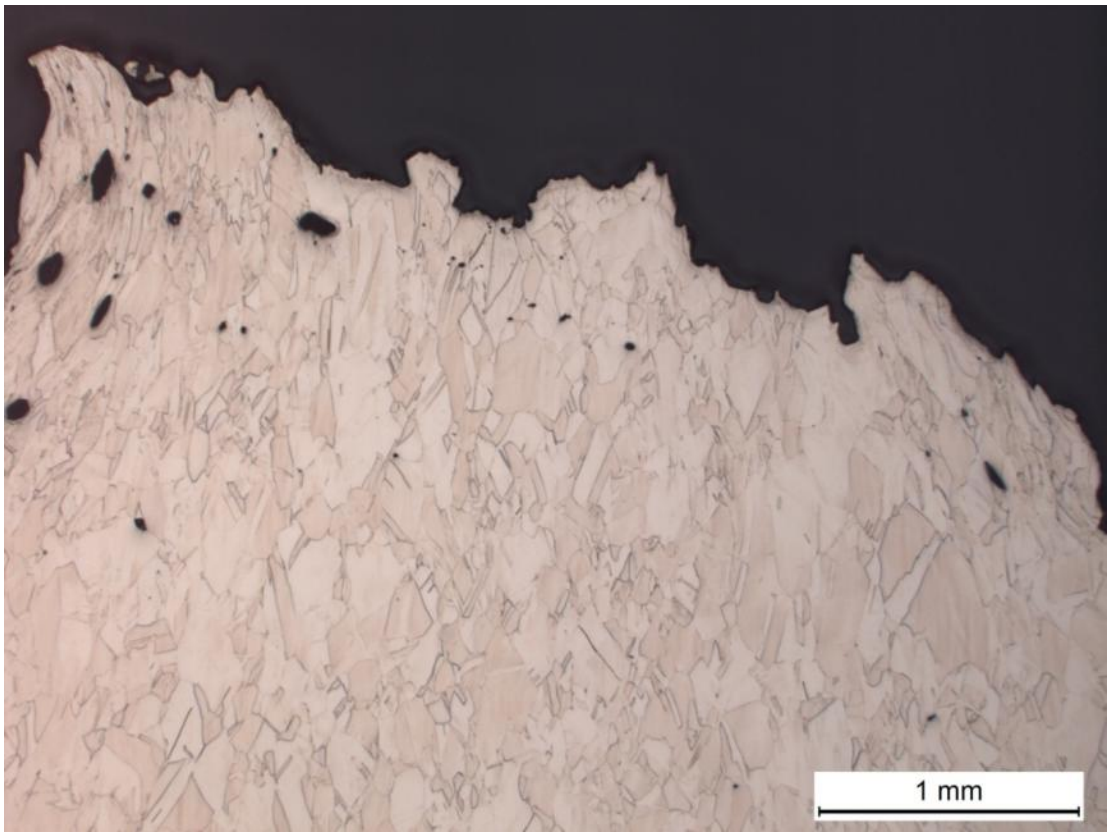

Figure 51. A close-up of Figure 50 rupture surface. The grains have elongated more on the left side.

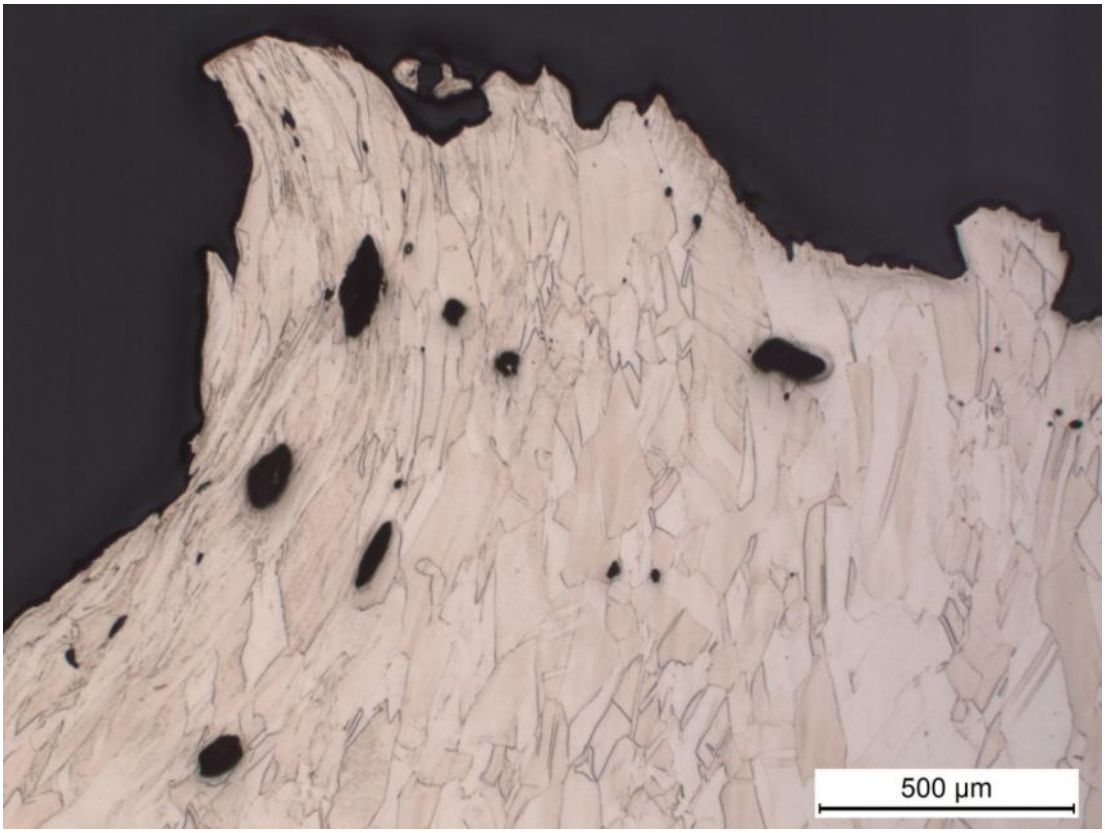

Figure 52. A close-up of Figure 51 left upper corner. The deformation of grains and the cavities near the broken surface can be seen clearly.

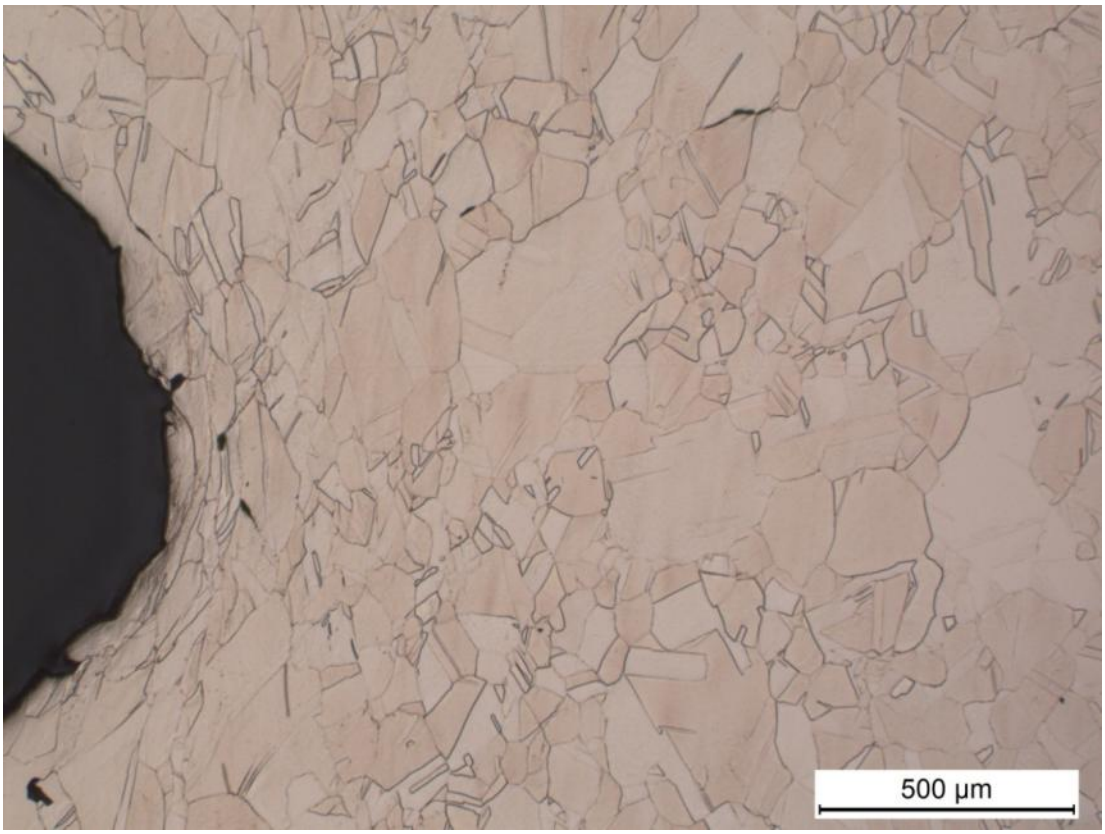

Figure 53. The unbroken notch of the test y396. The grains near the notch bottom have more elongated shape than the other grains in the picture.

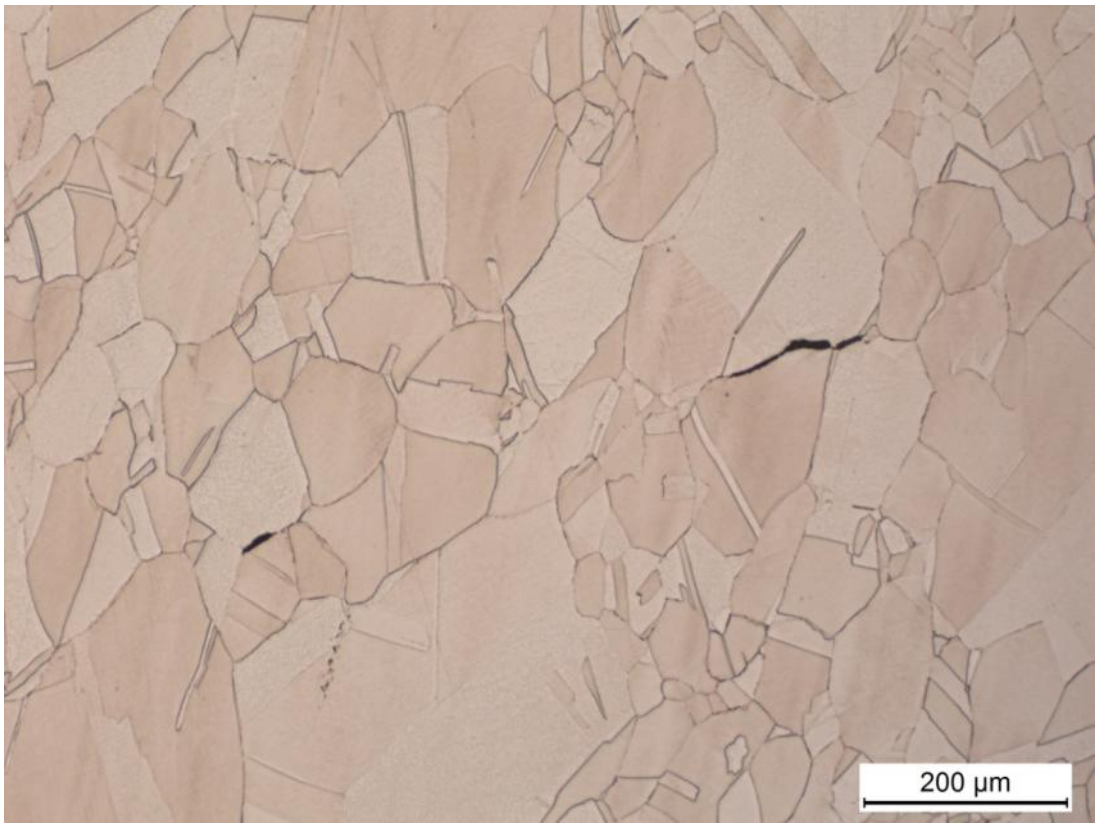

Figure 54. A close-up of Figure 53 0,6-1 mm away from the notch bottom. Few cavities exist on the grain boundaries.

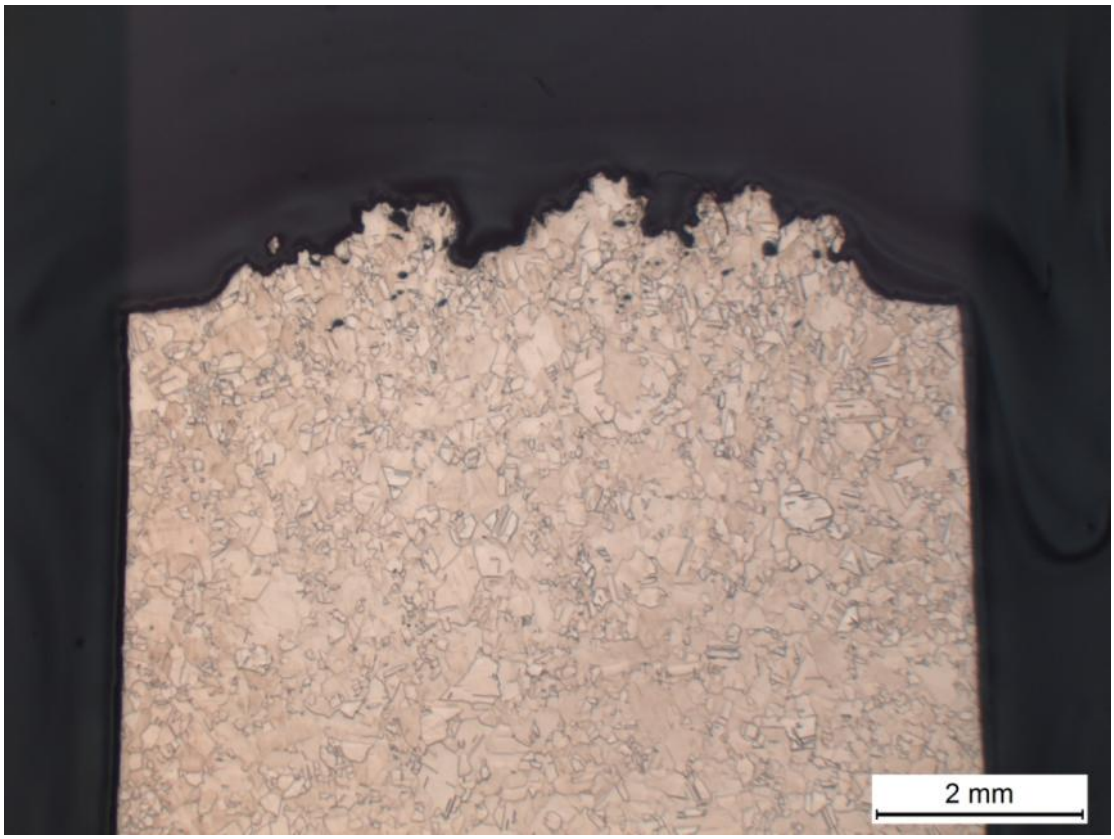

Figure 55. The broken notch of the test y397 (250 °C, 80 MPa, 457 h). Cavities appear near the broken surface.

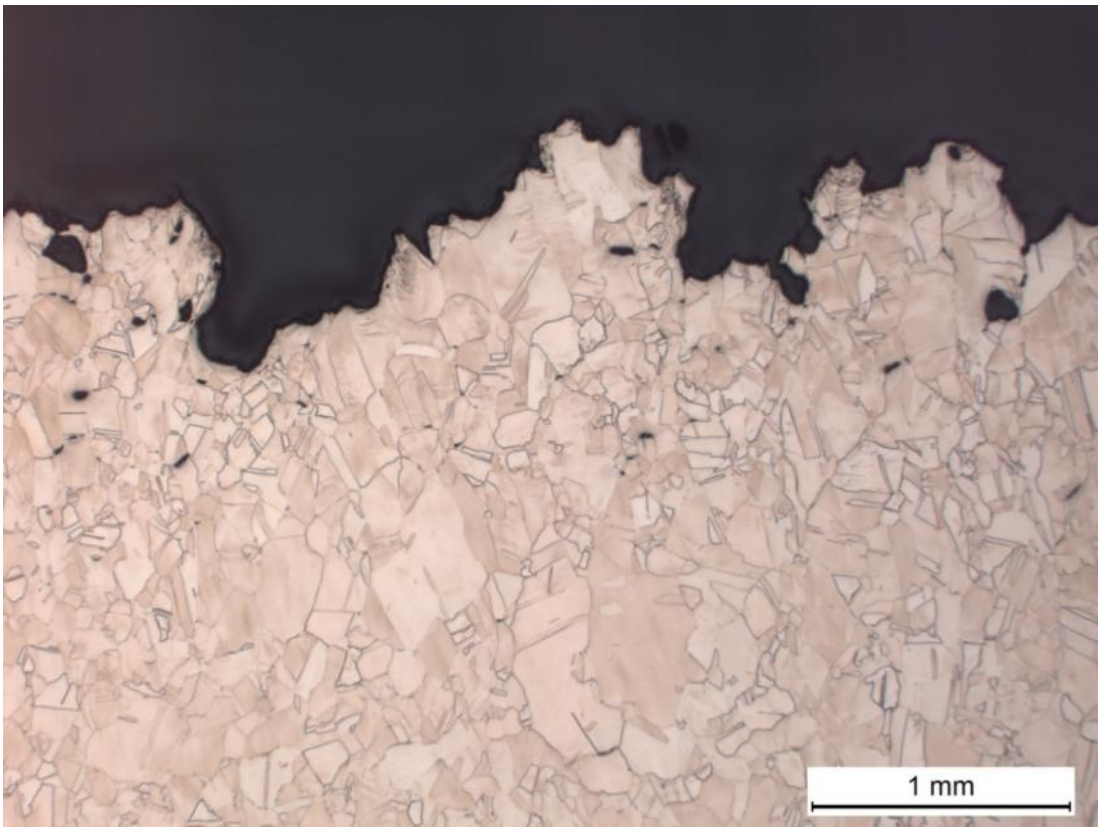

Figure 56. A close-up of Figure 55 middle section of the rupture surface. Small cavitation exists.

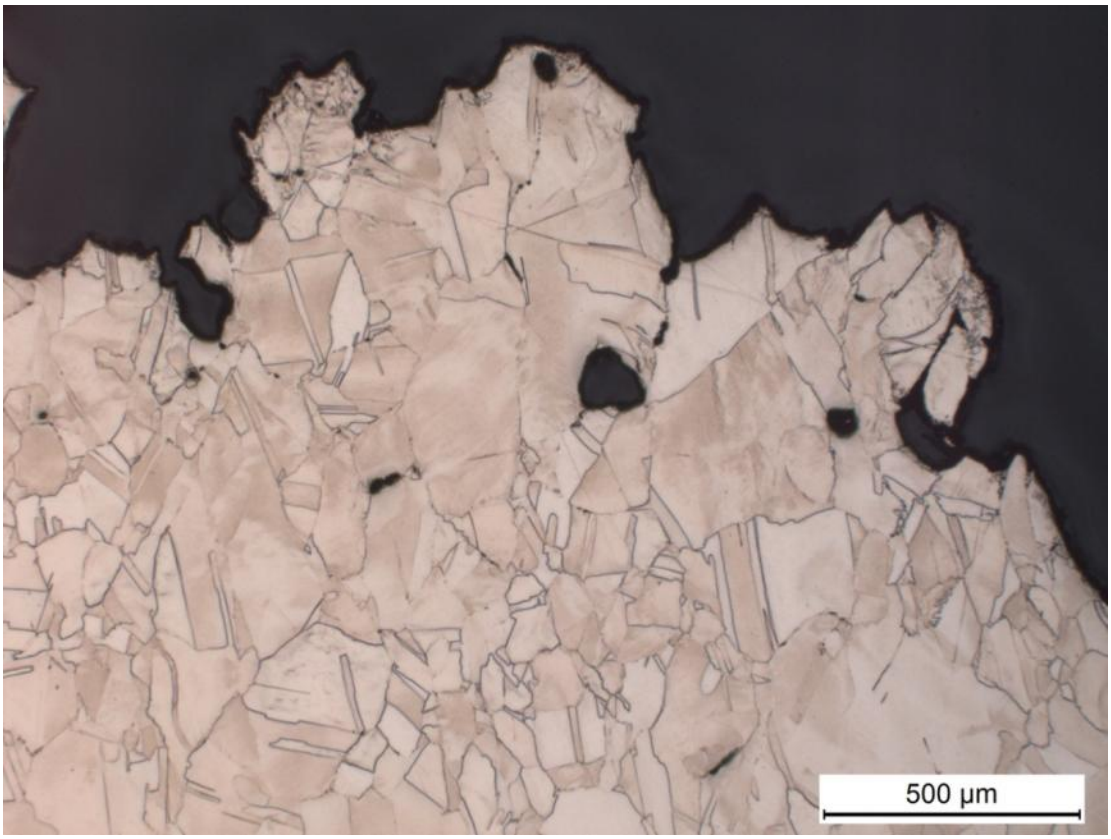

Figure 57. A close-up of Figure 55 upper right corner near notch bottom. Some cavities exist on the grain boundaries.

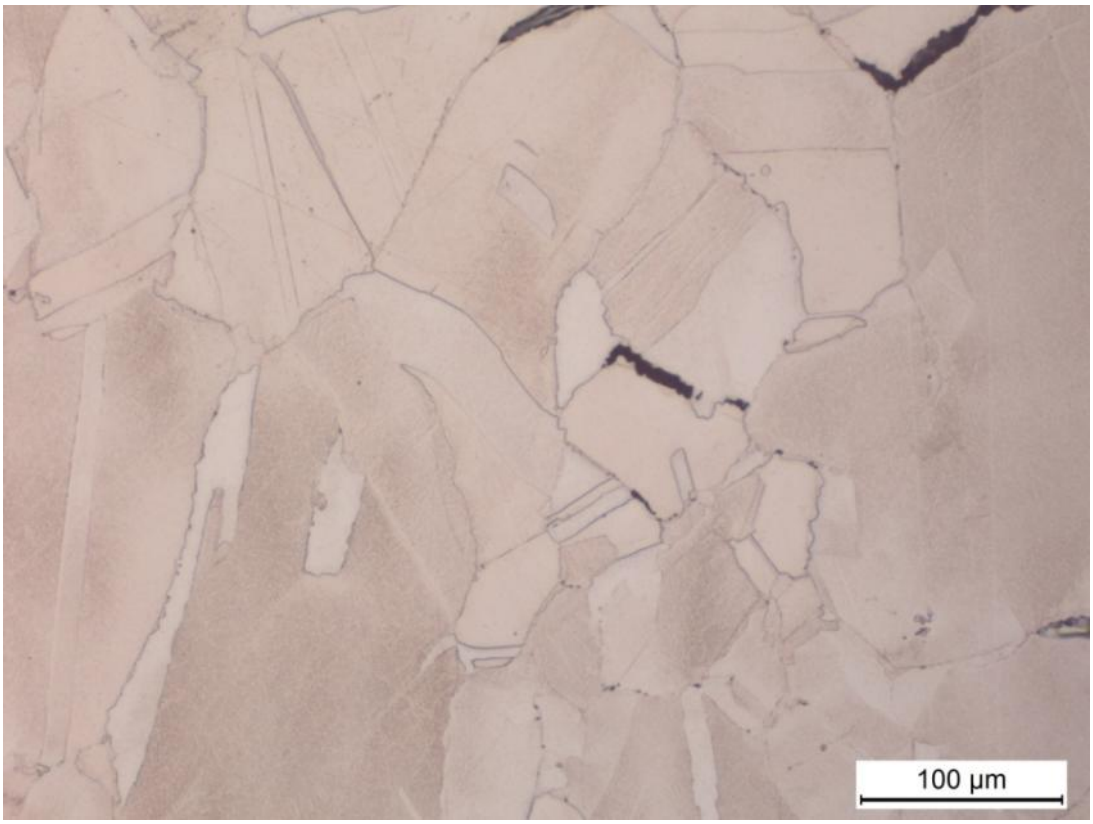

Figure 58. A close-up from Figure 55 left side 0.5-1 mm away from the broken notch bottom. The cavities seem to follow the grain boundaries.

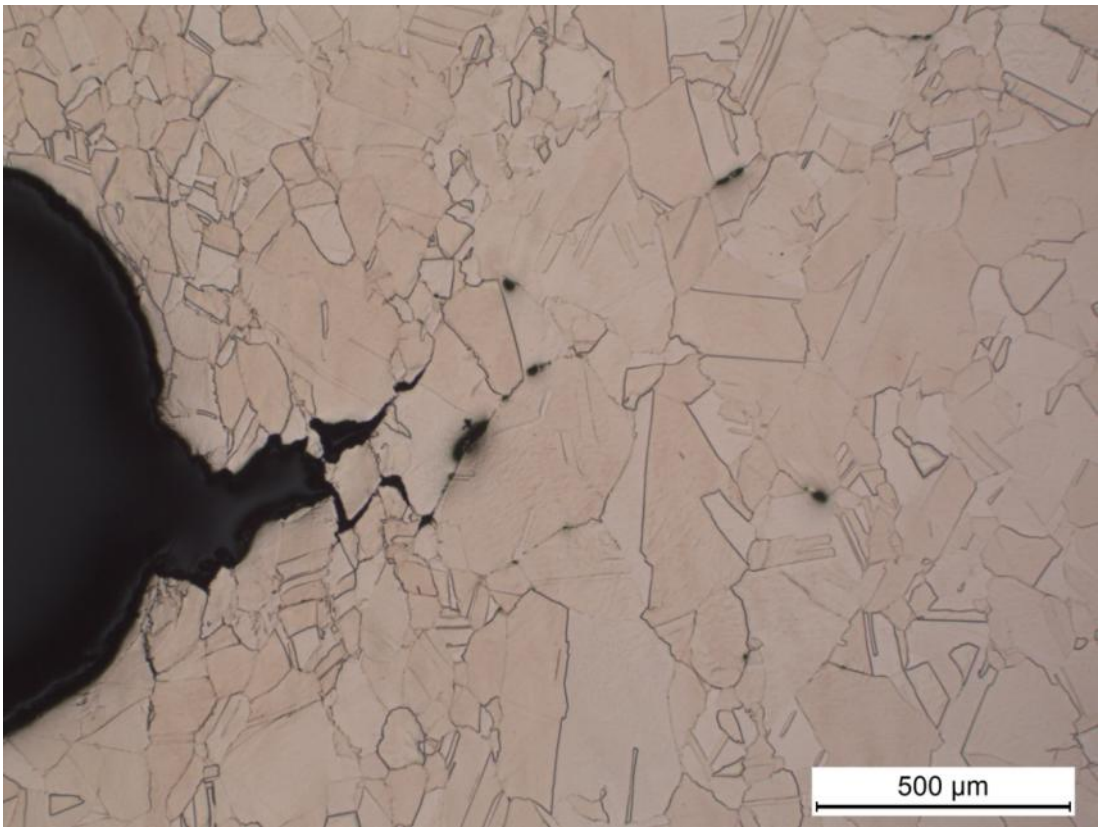

Figure 59. The unbroken notch of the test y397. The notch bottom has started to crack.

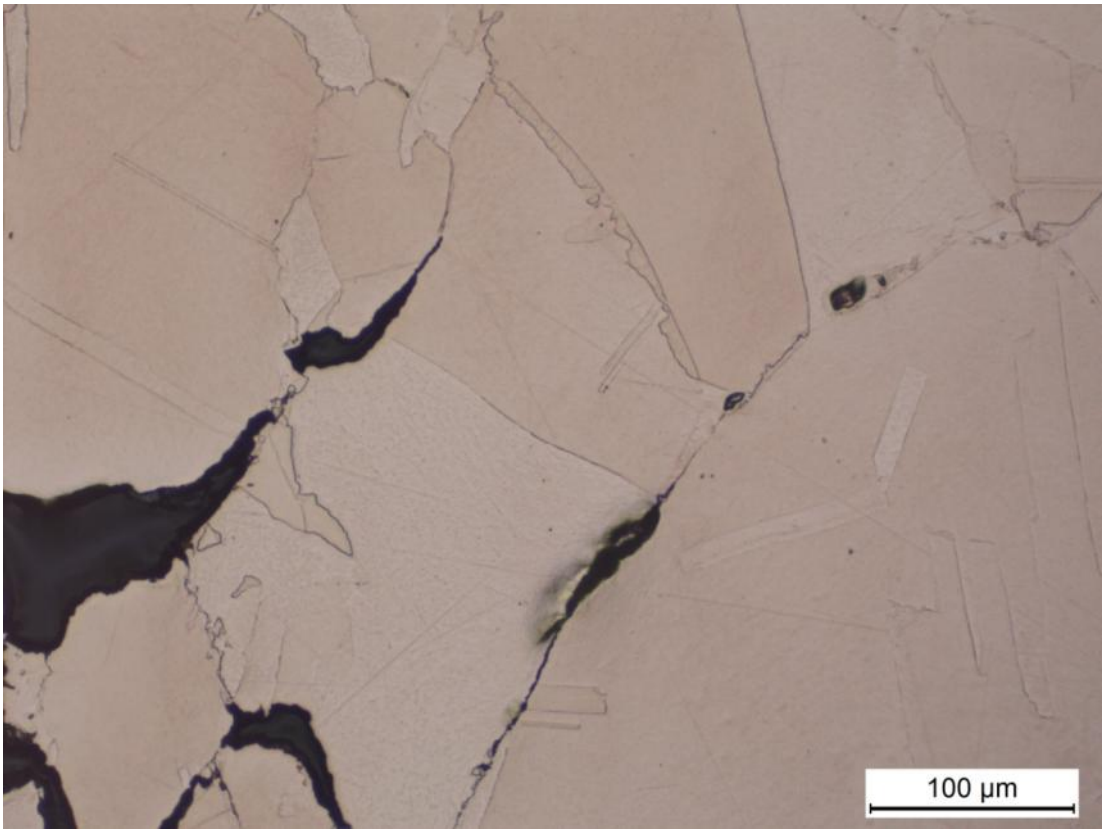

Figure 60. A close-up of Figure 59 notch bottom. Cracks seem to follow the grain boundaries.

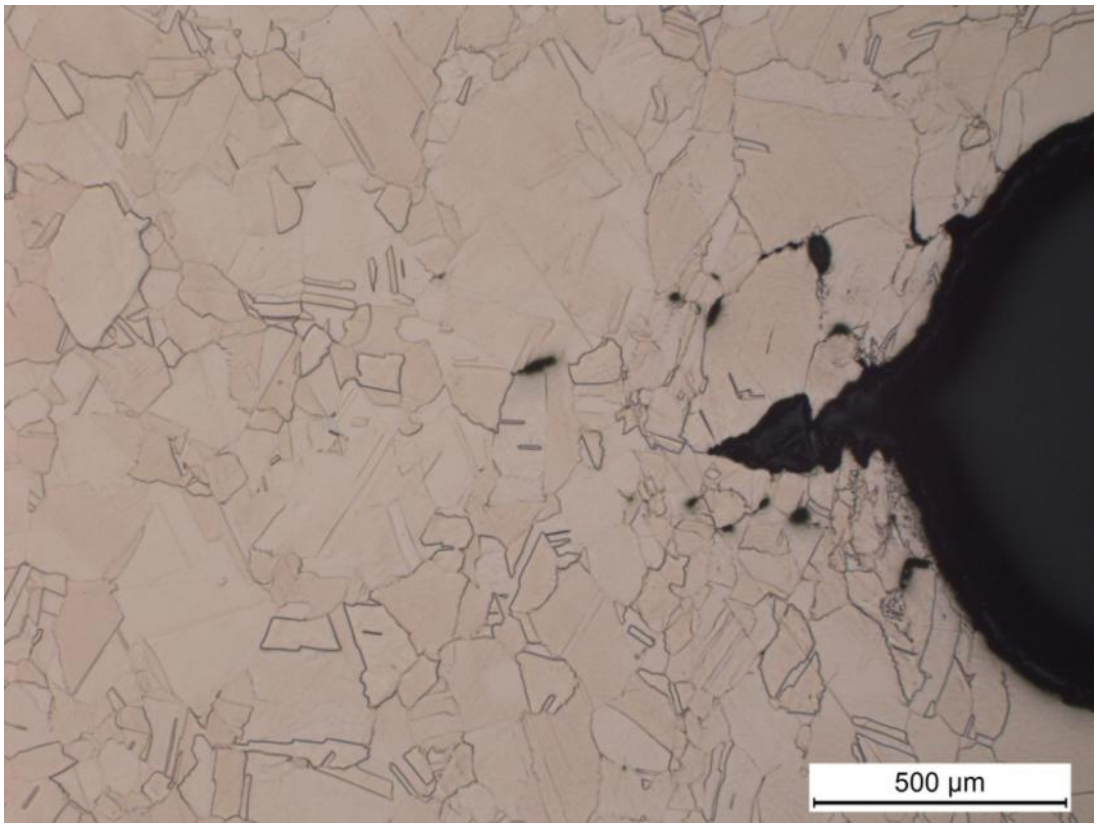

Figure 61. The other side of the unbroken notch of the test y397. This side has also started cracking.

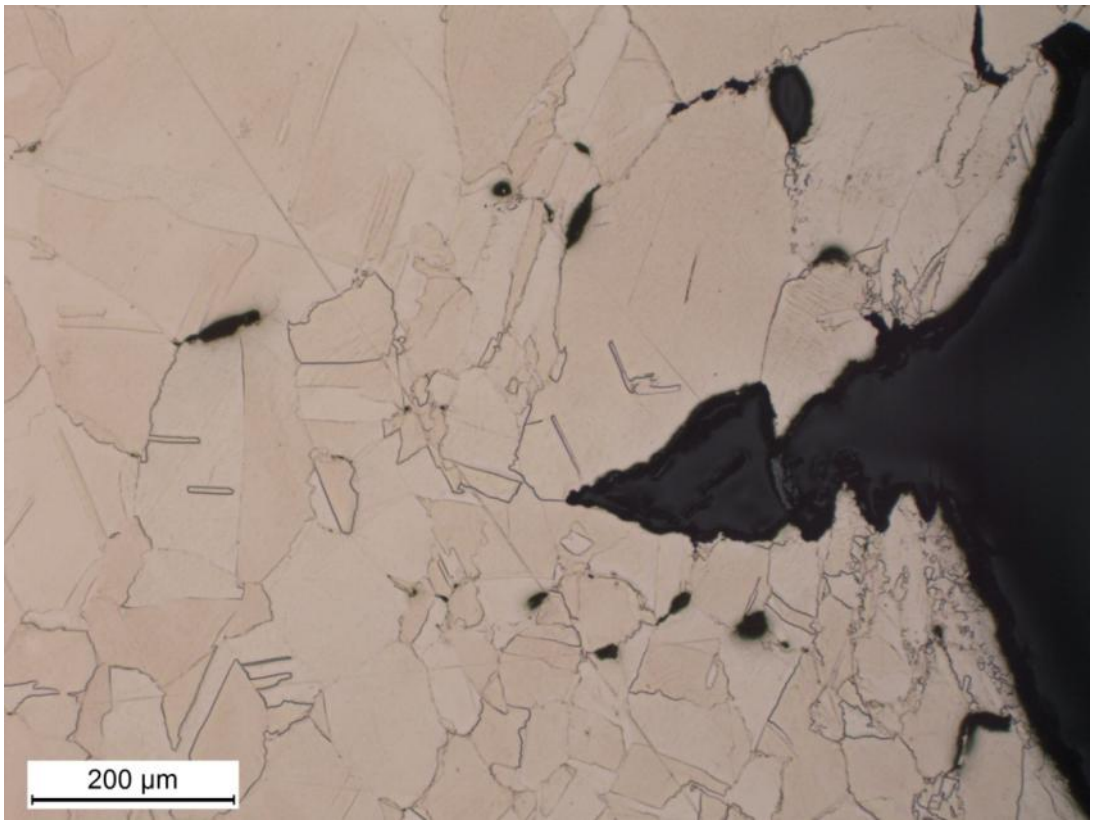

Figure 62. A close up of Figure 61 notch bottom crack. Cavities are seen on the grain boundaries, and the crack seems to follow the grain boundaries.

5.5 Effect of sulphide rich groundwater on creep properties

The results for the *in situ* room temperature loading tests are presented in Figure 63 (the geometry of the notched test specimen is shown in Figure 20) and the *ex situ* creep test results in Table 17. The displacement of the *in situ* loading tests during the five week exposure for two different sulphide concentrations (RGW + 1 mg/l and RGW + 200 mg/l of sulphide) is presented in Figure 63. The reference specimen shows a smaller increase in the displacement when comparing P3 and P1 (the dark blue and dark green lines). The step-wise increase in displacement close to the end of the exposure of the specimen P1 was caused by a small peak in loading (malfunction of the servo-hydraulic loading machine). The surface film thickness after the exposure to RGW + 200 mg/l sulphide for five weeks was 9.2 µm. The composition of the surface film in presented in Table 16. [18]

The *in situ* testing times of the interrupted tests are according to Figure 63 930.6 h for P1 and 955.6 h for P3. It would seem that the higher sulphide concentration increases the deformation a little. The loads used were 1.01 kN for P1 and 1.0 kN for P3, which corresponds to stresses close to 20 MPa. The difference between the specimen geometry, testing temperature, and stresses are quite significant, and for that reason the comparison between the results from the *ex-situ* study and the thesis study is not straightforward. [18]

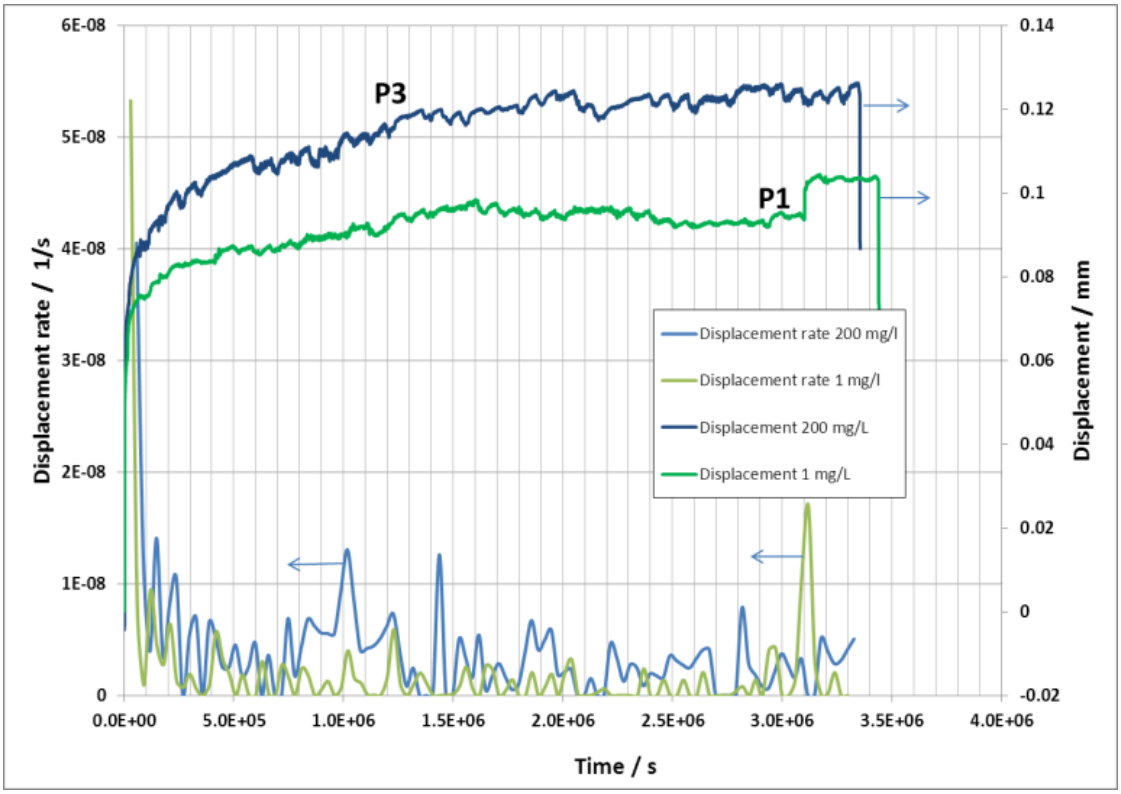

Figure 63.Comparison of displacement (right axis) and displacement rate (left axis) during exposure to RGW + 1 mg/l S^{2-} (green lines) and RGW + 200 mg/l S^{2-} (blue lines). [18]

Table 16. The surface film compositional analyses.[18]

Element	Weight %	Atom %
O	10.98	29.75
Na	0.85	1.6
Mg	2.58	4.6
Al	0.17	0.28
S	5.61	7.58
Cl	0.44	0.54
Ca	3.71	4.01
Cu	75.67	51.63
Total	100	100

The normalised skeletal stress $\sigma_{VM}^*/\sigma_{net}$ was determined according to the code of practise for the in situ specimen geometry at notch acuity ratio of 26.7 (d_{no}= 8 mm and r_{no}= 0.3 mm). The value of the skeletal stress was 0.62. Due to the differences in geometry between sulphide specimen and the geometries mentioned in the code of practise, the determination of the normalised stress is not absolute. When compared to this work $\sigma_{VM}^*/\sigma_{net}$ –values, 0.676 and 0.548 (square 2 and round 2) are the closest to 0.62. [29]

The *ex situ* creep test results are presented in Table 17. As can be seen in Table 17, there seems to be a small degrading effect of the sulphide exposure on the creep properties when comparing the un-exposed and exposed results: the time to rupture is slightly lower for the exposed specimens than for the un-exposed. Both the *in situ* and *ex situ* creep results indicate a small degrading effect related to the exposure of sulphide containing groundwater. When the creep data is normalised and shown with publicly available data from various heats and laboratories, the results are within the scatter band. In Figure 64 is shown the comparison of the *ex situ* results with this work and uniaxial SKB results with Larson-Miller parameter. The comparison indicates that the SKB uniaxial data and sulphide test data behave quite similarly. [18]

Table 17. The results of the sulphide exposure tests (RGW +200 mg/l S^{2-} for five weeks).

Specimen	σ [MPa]	T [°C]	Sulphide exposure	Z [%]	t_r [h]	Fracture ε [%]
y359	125	215	no	82	226	66.9
y362	125	215	yes	67	218	63.7
y358	115	215	no	78	2508	76.7
y361	115	215	yes	75	2053	69.3
y360	100	215	no	NA*	10007*	32.64*
y363	100	215	yes	NA*	9099*	27.30*

* marked results are from running tests. [18]

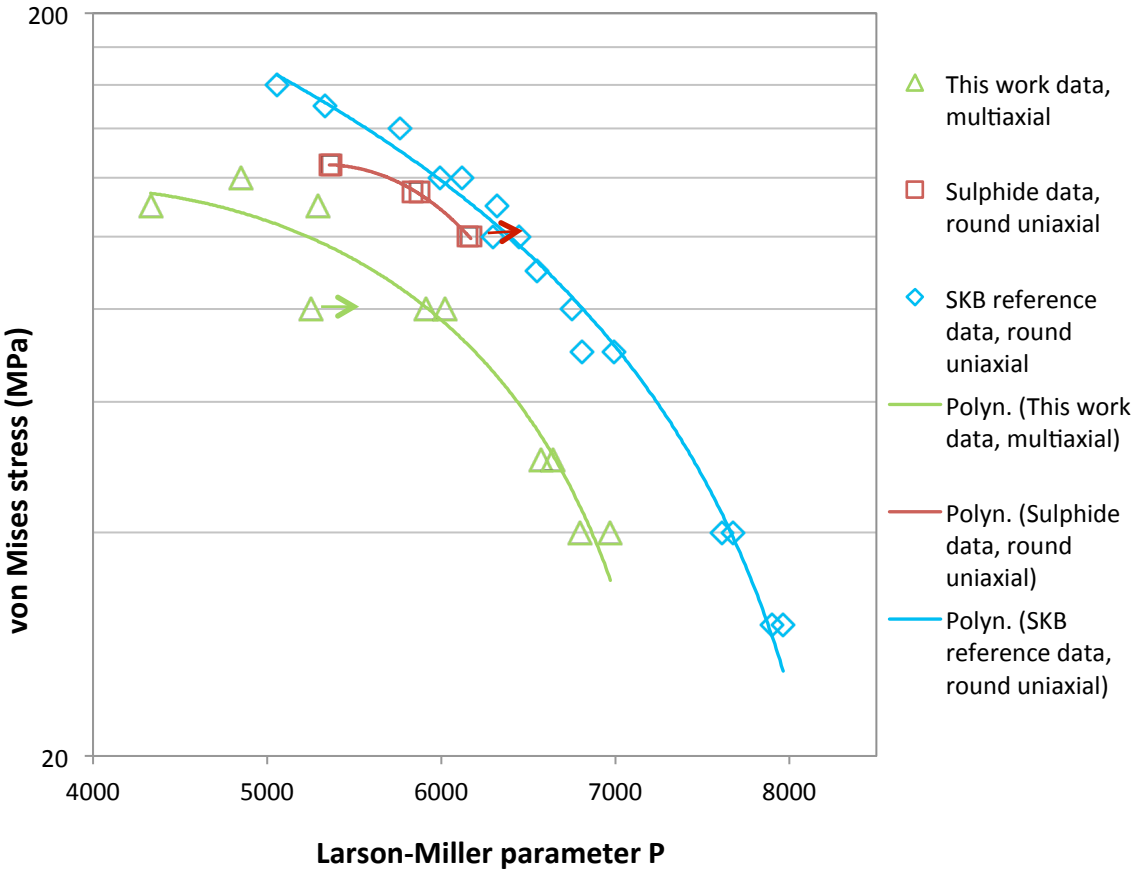

Figure 64. Von Mises stress as a function of Larson-Miller time-temperature parameter. This work multiaxial data and SKB uniaxial reference data (Table 10) were added for comparison. [10]

The SEM/EDS –studies made on fracture surfaces and cross-sections of the exposed specimens revealed in some cases small concentrations of sulphur on the surfaces. In case of cross-sections of the exposed specimens, there can be a carry-over from the sulphur containing surface film due to the sample preparation technique (for example polishing). In the creep specimens, the sulphur may have diffused via surface diffusion from the external sulphur containing surface film e.g. during the cool down of the furnace after the specimen had fractured by creep. Thus, based on the results from this work one cannot definitely conclude that sulphur has actually diffused into Cu-OFP from the sulphide containing groundwater during the exposure. This is in contradiction with the earlier findings by other studies of high sulphur concentrations on the CT-specimen fracture surfaces. Also in these studies no evidence of stress corrosion cracking was found under multiaxial constant loading conditions in the sulphide containing groundwater at T = 25°C. [18]

6 DISCUSSION AND CONCLUSIONS

The study indicates that the amount of cold work in the square specimens seems to be lower than in the round specimens or non-existent (Figure 31). The difference in the initial plastic and primary creep strain is not remarkable for the square and last three round bars. When comparing the first round specimens to the square ones, the difference seems bigger. It could be concluded that the use of square specimens gives a bit more realistic results than the turn-milled round specimens, but the difference (when the milling is gentle enough) is not remarkable. However, the problem lies in manufacturing: how to know whether the specimens are turn-milled gently enough before testing? A reliable manufacturing procedure should be established. No significant difference in creep life between round and square specimens were found, suggesting comparable mechanisms of creep damage and failure. Thus the use of round specimens (when properly manufactured) can also be recommended. The amount of cold work could influence rupture times, when tested at lower stresses and longer times, and the tests fail with less deformation. Wire-eroded specimen could be recommended to be used when the exact amount of initial plastic and primary creep strain has to be measured.

More tests made by square specimens are needed to achieve a useful data base. In the future a round geometry made completely by wire-erosion could be good choice for multiaxial creep testing since it would be better to have the same geometry with all the specimens when comparing the results. However, problems appear here too, because the rotating of the specimen during EDM is challenging, as is the removal of large amount of material with EDM. Probably in the future with experience the quality of the round bars will get better. In any case more attention should be paid to the manufacturing methods, so that the specimens wouldn't experience cold work.

The reliable comparison of the results between different studies is always challenging. The comparison of results in this study between square and round notched specimens should be reliable, since the square shaped area is designed to match the original cross-sectional area of the parallel length of the round specimens, and the octagon shaped area is designed to match the original cross-sectional area across the notch throat of the round specimens. The specimens are made of the different Cu-OFP material batches, which can also influence the results. Different material batches can have in some cases slightly deviating amounts of ingredients, for example phosphorus. Higher amount of phosphorus can increase creep lifetime and make the specimen more ductile than a specimen with smaller amount of phosphorus [39]. Small differences especially in the notch root geometry and notch depth will influence the results a little.

The first three round specimens were known to be less accurately specified than the other specimens, thus the results for the first round bars have more variation. Also one of the first round tests (y385) was interrupted, so it can't be analysed as a rupture point. Based on the results presented in Chapter 5.2, different opinions on the effect of multiaxiality on the creep lifetime exist. However nowadays it seems that the general opinion is heading to the conclusion that the multiaxiality in creep testing shortens the rupture time.

The predicted values and the real results match very well when comparison is based on Larson-Miller parameters (Figure 33) and Wilshire model (Figure 36). This is a good sign indicating that the specimens have behaved as expected, in other words the testing bars work for their purpose. The first three round specimens differ the most from the predictions, which was expected since the manufacturing history of the first three specimens was unclear. However, the small amount of tests doesn't give a reliable view. Also the Larson-Miller model is often used for its simplicity, but its representative value isn't necessarily very high. If all of the tests at the same temperature could have been also performed at the same stress, the comparison of the results would have been easier. Now from the ten tests six were performed as couples at the same testing temperature and stress (tests y397 and y418, y400 and y419, y405 and y420). The tests y385 and y396, y386 and y391 were performed at same temperature but at different stress.

From the FE analysis and the post-metallurgical evaluation it can be seen that near the notch bottom stress level is the highest. The FE analysis shows that the highest level of multiaxiality and maximum principal stress is located not exactly at the notch root, but 0.5-1 mm away from it towards the middle. In square geometry the corners can act as a locus for high stress values, which can cause different results when comparing round and square geometry. The FE analysis suggested also that the notches might be too close and affect to each other to some extent. As a solution the distance between the notches could be extended to 20 mm. Determination of the skeletal point and the corresponding stresses for sharp notches with the FE analysis is challenging, thus the FE calculations didn't give as consistent results as the code of practise suggested. However, it was said in the code of practise that for severe notches ($d_{no}/r_{no} > 20$) the radial locations of the skeletal points for each of the stresses do not coincide. A new version of the code of practise is coming up in the near future, since it has been found necessary to update the skeletal point stress values particularly for sharp notches. The FE analysis also suggests that for sharp notches, the distributions of maximum principal stress rather than von Mises stress are applicable to define the skeletal point. The FE analysis with LCSP model would have been more accurate and realistic than the Norton model based analysis. The LCSP calculations are at this moment on-going, and the results from this model will be presented later on. [22,34]

The uniaxial and multiaxial creep testing in sulphide rich groundwater indicated that higher sulphide amount decreased slightly the rupture times of Cu-OFP. But the difference between the results was still within the normal scatter band. In the sulphide exposure project only the effect of sulphide to the creep properties was studied. The

groundwater has many other components too which might affect alone or together with the other components differently. Perhaps in future the effect of the other parameters (pH-level, Cl^-, NH_4^+, and NO_2^-) in creep behaviour could be studied. When comparing the results from in situ sulphide exposure testing with this work results, it can be seen that the results are not very comparable with each other: the difference in specimen geometry, testing temperature (room temperature versus 152- 350 °C) and stress (20 MPa vs. 40-110 MPa) were quite large. Indications of possible sulphur ingress to Cu-OFP grain boundaries from sulphide containing groundwater were found, which initiated further studies on the possibility of grain boundary embrittlement through such ingress. But otherwise no solid evidence on that sulphur has actually diffused into Cu-OFP from sulphide containing groundwater during the exposure was found. [18]

7 SUMMARY

In this Master of Science thesis the possibility to use a new testing approach for multiaxial creep testing of Cu-OFP was investigated. The new testing approach included a square shaped testing bar manufactured completely by wire-erosion to minimize the effect of cold work. The square bar had two octagon shaped notches. The testing programme included ten multiaxial tests: four square specimens and six round specimens manufactured by turn-milling. The manufacturing history of the first three round specimens was unclear, and the last three round specimens were "gently" turn-milled in order to keep the amount of cold work as low as possible. The results indicate that the amount of additional cold work from manufacturing in square specimens seems to be lower than in the round specimens or non-existent. The amount of cold work can be observed by the amount of initial plastic and primary creep strain after loading: if the measured plastic strain is lower, the specimen has experienced cold work before the creep testing. However, the difference in initial plastic and primary creep strain between the square and last three round bars is not large. The first round specimens had more variation in results, which is probably due to the undefined manufacturing history. No significant difference in creep life between square and round bars existed, suggesting comparable mechanisms of creep damage and failure. Wire-eroded specimen could be recommended to be used when the exact amount of initial plastic and primary creep strain has to be measured.

When comparing the multiaxial creep results to the Swedish SKB study, the presumption is that the results behave quite similarly. Of course, the small amount of tests doesn't give an extensive view. The Larson-Miller parameter and the Wilshire model were applied for the results, and it appears that the results fit well to the models. *Z*-factor for the Wilshire model was 3.20, which is satisfactory. From the FE analysis and post-metallurgical evaluation it can be seen that the highest values of strain and stress focuses on the area near notch bottom. The FE analysis shows that the highest level of multiaxiality and maximum principal stress are located not exactly at the notch root, but 0.5-1 mm away from it to the middle. Though the definition of the skeletal point for sharp notches is not straightforward, a suitable skeletal zone in which the stresses could be identified was determined. The FE analysis suggests that for sharp notches, the distributions of maximum principal stress rather than the von Mises stress are applicable to define the skeletal point.

In the future more testing with the square geometry is needed. As an option for the square bar, a round bar made completely by wire-erosion could be a good choice. However, the manufacturing of a round bar by wire-erosion is challenging and needs further practise. More precise FE results could be achieved by the LCSP method, which is on-going at this moment. An update of the code of practise concerning the determination of skeletal points for sharp notches could be useful in the future.

REFERENCES

[1] Posiva Oy, “General Time Schedule for Final Disposal,” 2013. [Online]. Available: http://www.posiva.fi/en/final_disposal/general_time_schedule_for_final_disposal. [Accessed: 21-Mar-2013].

[2] A. Knuutila, “Long-term creep of nuclear fuel disposal canister shroud,” Finland, 2001.

[3] H. Rydén and M. Johansson, “Design analysis report for the canister,” pp. 1–80, 2010.

[4] J. Rantala, J. Salonen, P. Auerkari, A. Laukkanen, and S. Holmström, “Material integrity of welded copper overpack – Final report 2012,” Helsinki, 2012.

[5] A. Martinsson and H. C. Andersson, “The Effect of Cold Work on the Creep Properties of Copper,” *MRS Proceedings*, vol. 1193, p. 8, Feb. 2011.

[6] Posiva Oy, “The Principles for Final Disposal,” 2013. [Online]. Available: http://www.posiva.fi/en/final_disposal/the_principles_for_final_disposal. [Accessed: 21-Mar-2013].

[7] L. Nolvi, “Manufacture of disposal canisters,” Posiva Oy, 2009.

[8] H. Andersson, F. Seitisleam, and R. Sandström, “Creep testing of thick-wall copper electron beam and friction stir welds at 75, 125 and 175 C,” 2005, p. 37.

[9] Svensk Kärnbränslehantering AB, “Nuclear Waste Containment Materials,” Stockholm, 2001.

[10] H. Andersson-Östling and R. Sandström, “Survey of creep properties of copper intended for nuclear waste disposal,” 2009.

[11] B. Pastina and P. Hellä, “Expected evolution of a spent nuclear fuel repository at Olkiluoto,” vol. 31, no. December 2006, p. 405, 2006.

[12] R. Wu, F. Seitisleam, and R. Sandström, “Creep properties of phosphorus alloyed oxygen free copper under multiaxial stress state,” no. October. 2009, p. 42.

[13] F. King, C. Lilja, K. Pedersen, and P. Pitkänen, “An update of the state-of-the-art report on the corrosion of copper under expected conditions in a deep geologic repository,” no. December. Svensk Kärnbränslehantering AB, 2010, p. 180.

[14] F. King, “Critical review of the literature on the corrosion of copper by water,” no. December. Integrity Corrosion Consulting Limited, 2010, p. 51.

[15] B. Rosborg and L. Werme, “The Swedish nuclear waste program and the long-term corrosion behaviour of copper,” *Journal of Nuclear Materials*, vol. 379, no. 1–3, pp. 142–153, Sep. 2008.

[16] F. King, “Corrosion of copper in alkaline chloride environments”. Integrity Corrosion Consulting Ltd, 2002, p. 78.

[17] L.-Z. Jin and R. Sandström, “Creep of copper canisters in power-law breakdown,” *Computational Materials Science*, vol. 43, no. 3, pp. 403–416, Sep. 2008.

[18] E. Arilahti, T. Lehtikuusi, T. Saario, K. Sipilä, and P. Varis, “Sulphide-induced embrittlement of CuOFP– Final Report 2012,” Espoo, Finland, 2012.

[19] K. Pettersson, “Development of a constitutive model for the plastic deformation and creep of copper and its use in the estimate of the creep life of the copper canister,” Stockholm, 2006.

[20] P. Auerkari and S. Holmstrom, “Creep performance of OFP copper for the overpack of repository canisters,” *Materials Research Society*, vol. 932, p. 8, 2006.

[21] G. W. Greenwood, “Comparisons and contrasts in creep behaviour,” *Materials Science and Engineering: A*, vol. 463, no. 1–2, pp. 166–170, Aug. 2007.

[22] S. Holmström, Engineering tools for robust creep modelling. Espoo, Finland: VTT Publications 728, 2010.

[23] M. E. Kassner, Fundamentals of Creep in Metals and Alloys. 2009.

[24] W. Bowyer, “Creep of the Copper Canister,” April, p. 39, 2003.

[25] J. Rösler, H. Harders, and M. Bäker, Mechanical behaviour of engineering materials: metals, ceramics, polymers, and composites, pp. 384–406, 2007.

[26] R. C. Hurst and J. H. Rantala, Influence of Multiaxial Stresses on Creep and Creep Rupture of Tubular Components, ASM Handbook vol 8, pp. 405-411, ASM International 2000.

[27] CEN, Metallic materials- Uniaxial creep testing in tension- Method of test. 2000, p. 31.

[28] P. Auerkari, S. Holmström, and J. Veivo, “Uniaxial and multiaxial creep testing of copper, ” no. December. Finland: SKI, 2003, p. 33.

[29] G. Webster, “A Code of Practice for conducting notched bar creep tests and for interpreting the data,” *Fatigue & Fracture of Engineering Materials & Structures*, pp. 319–342, 2004.

[30] R. Wu, L. Jin, and R. Sandström, “Influence of Multiaxial Stresses on Creep Properties of Phosphorus Alloyed Oxygen Free Copper,” pp. 1–8, 2009.

[31] ASM Handbook Committee, ASM Handbook Volume 8, Mechanical Testing. USA, 1985, p. 778.

[32] V. M. Martins and S. Holdsworth, “The LICON methodology for predicting the long term service behaviour of new steels,” *Materials at high temperatures*, pp. 99–103, 2002.

[33] J. H. Rantala (Ed). Task 6 Final report: Summary of results and development of the methodology LICON project BE95-3019, Doc. nr. LICON/JRC022/TLR/12, 21 Sept 2001

[34] G. a. Webster, K. M. Nikbin, and F. Biglari, “Finite element analysis of notched bar skeletal point stresses and dimension changes due to creep,” *Fracture of Engineering Materials and Structures*, vol. 27, no. 4, pp. 297–303, Apr. 2004.

[35] E. Arilahti, T. Lehtikuusi, T. Saario, and P. Varis, “Sulphide-induced embrittlement of CuOFP – Intermediate Report 1,” Espoo, Finland, 2011.

[36] E. Arilahti, T. Lehtikuusi, T. Saario, and P. Varis, “Sulphide-induced embrittlement of CuOFP – Intermediate Report 3,” Espoo, Finland, 2012.

[37] K. Sipilä, “Sulfidipitoisen pohjaveden vaikutus kuparin virumiseen,” *dspace.cc.tut.fi*, p. 101, 2012.

[38] P. Auerkari, “Robust prediction of full creep curves from minimal data and time to rupture model,” *Energy Materials, Materials Science & Engineering for Energy Systems*, vol. 1, pp. 249–255, 2006.

[39] H. Andersson, R. Sandstrom, and F. Seitisleam, “Influence of phosphorous and sulphur as well as grain size on creep in pure copper”, Svensk Kärnbränslehantering AB, 1999, p. 40.

APPENDIX 1

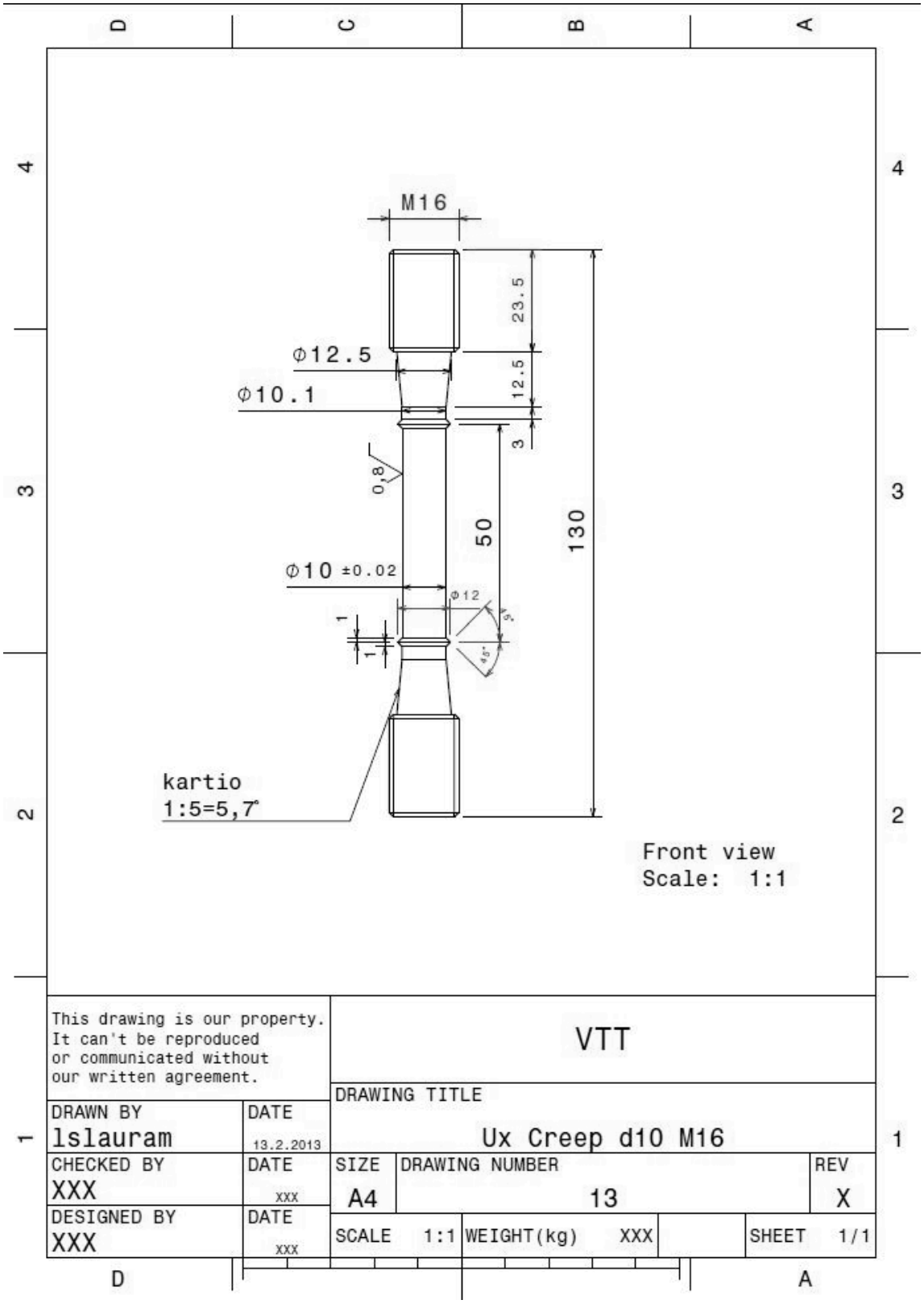

Figure 65. Uniaxial creep testing bar.

APPENDIX 2

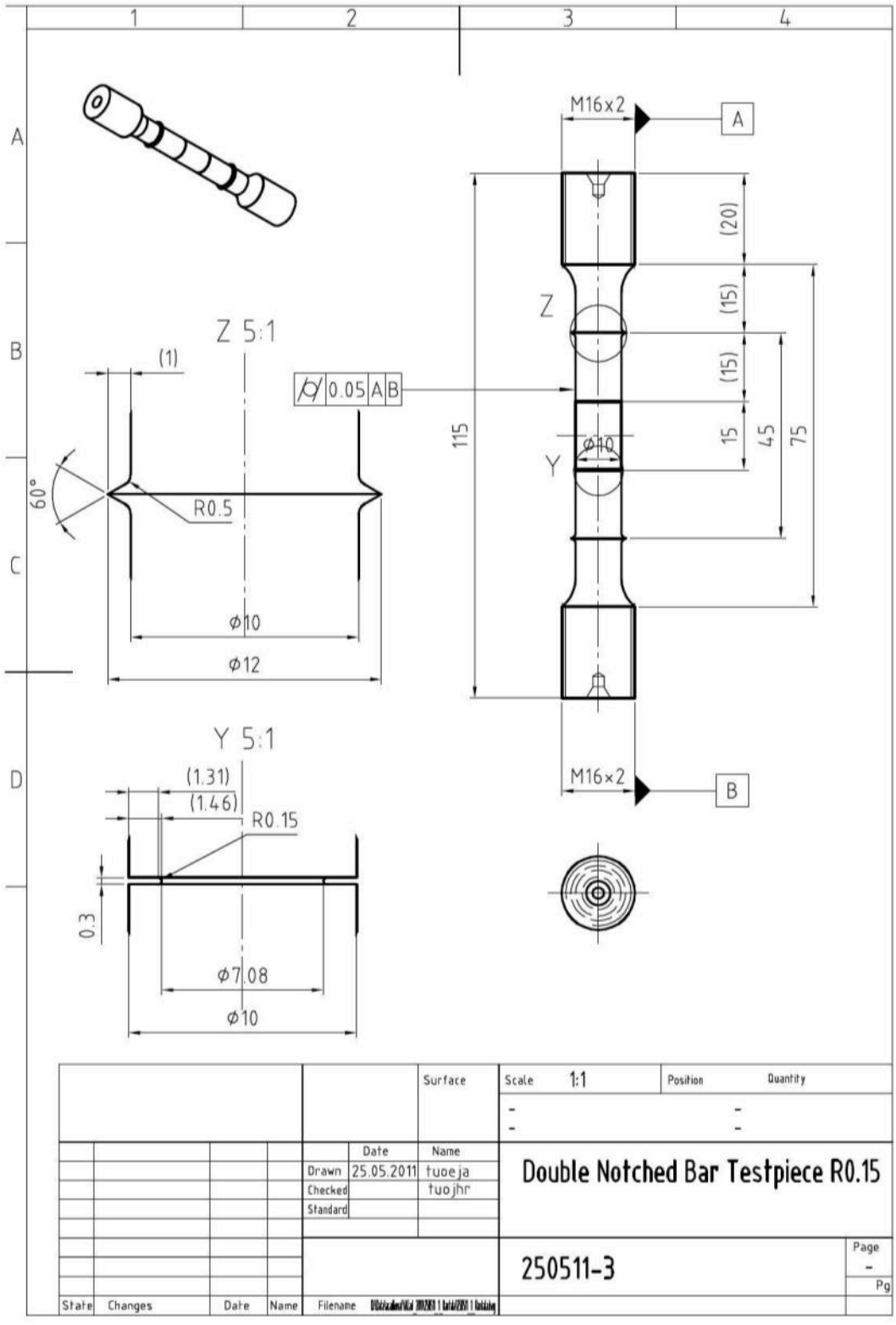

Figure 66. Double notched round multiaxial creep testing bar.

APPENDIX 3

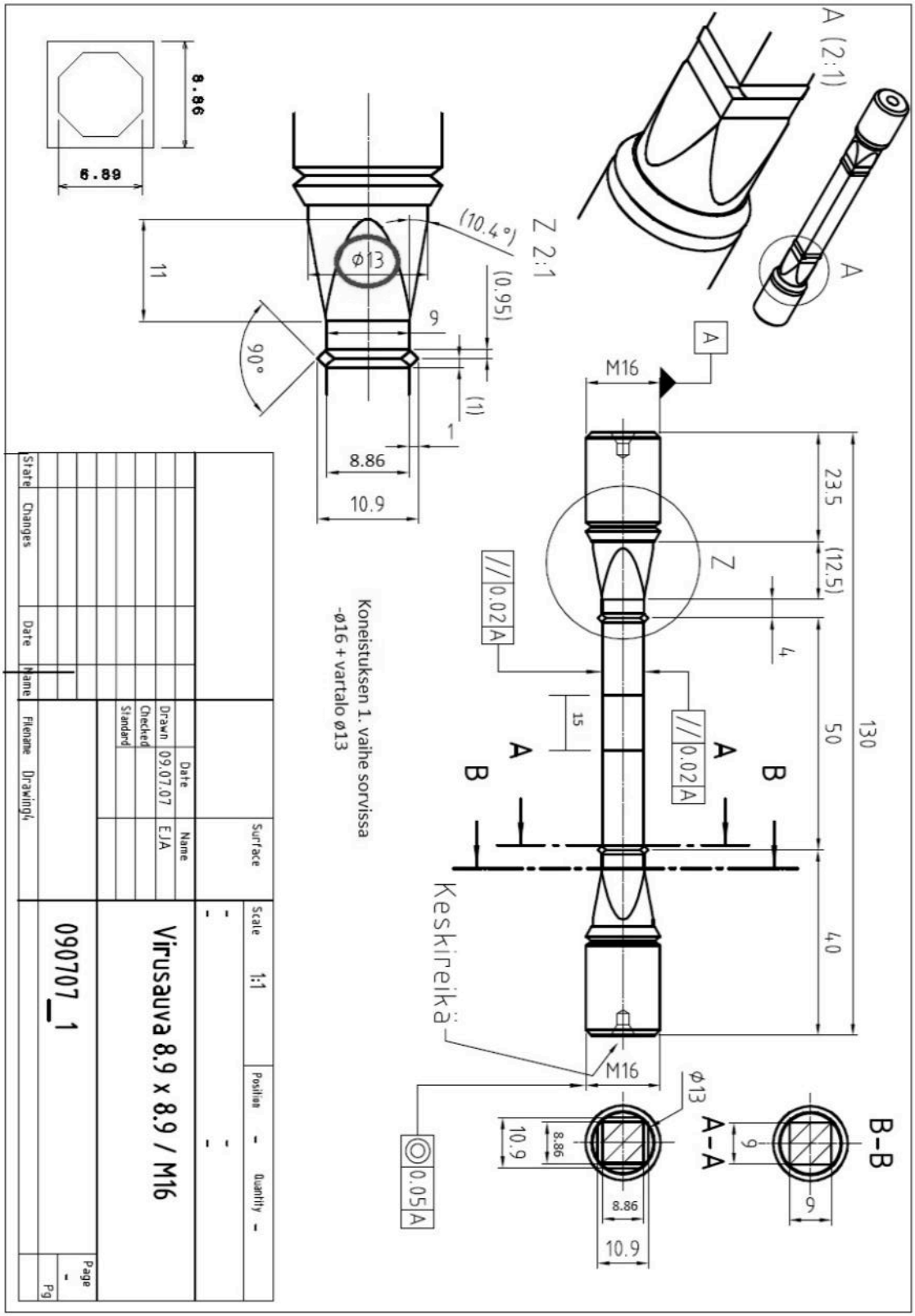

Figure 67. Double notched square shaped multiaxial testing bar.

APPENDIX 4

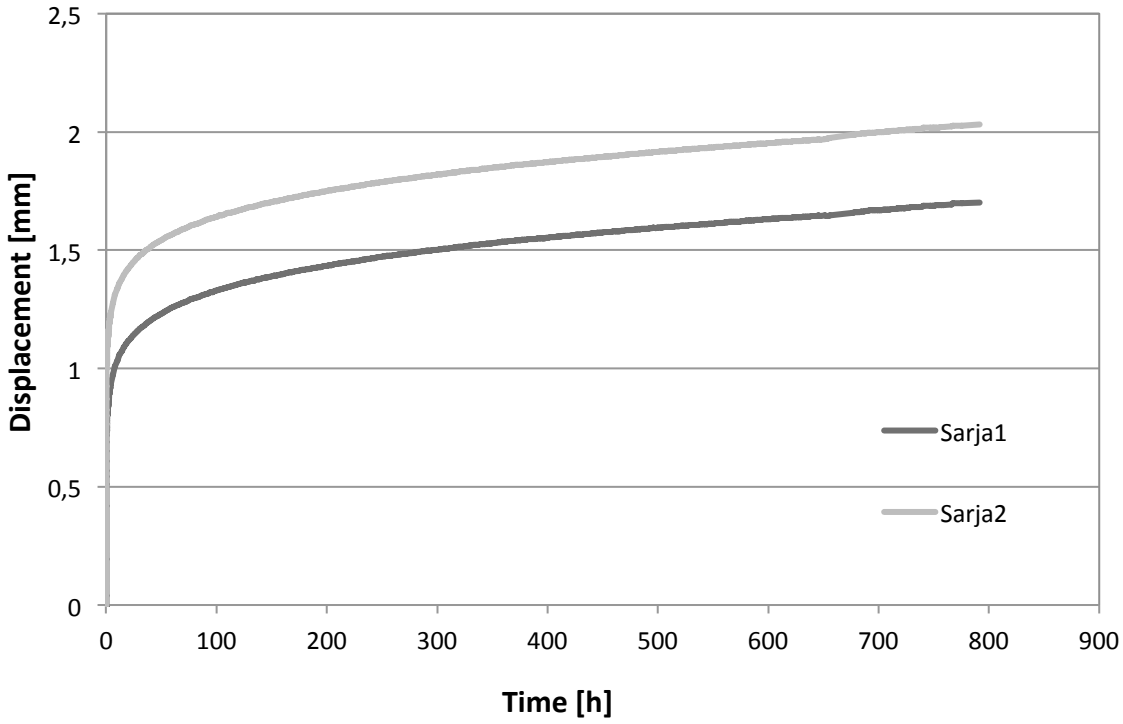

Figure 68.Displacement-time diagram for test y385.

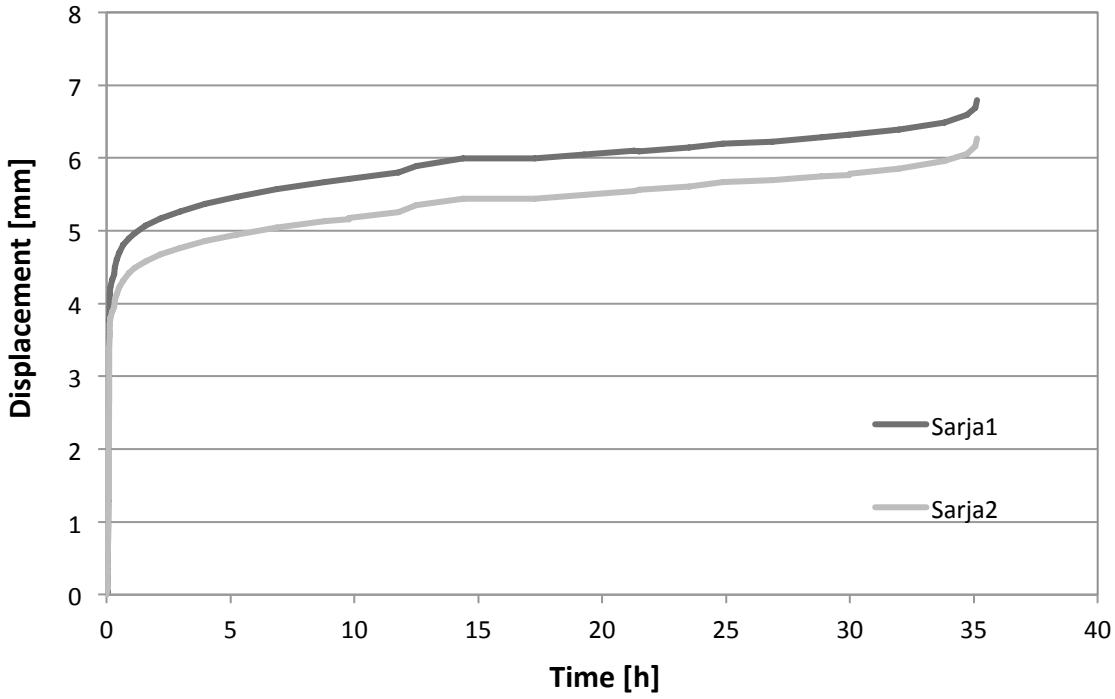

Figure 69.Displacement-time diagram for test y391.

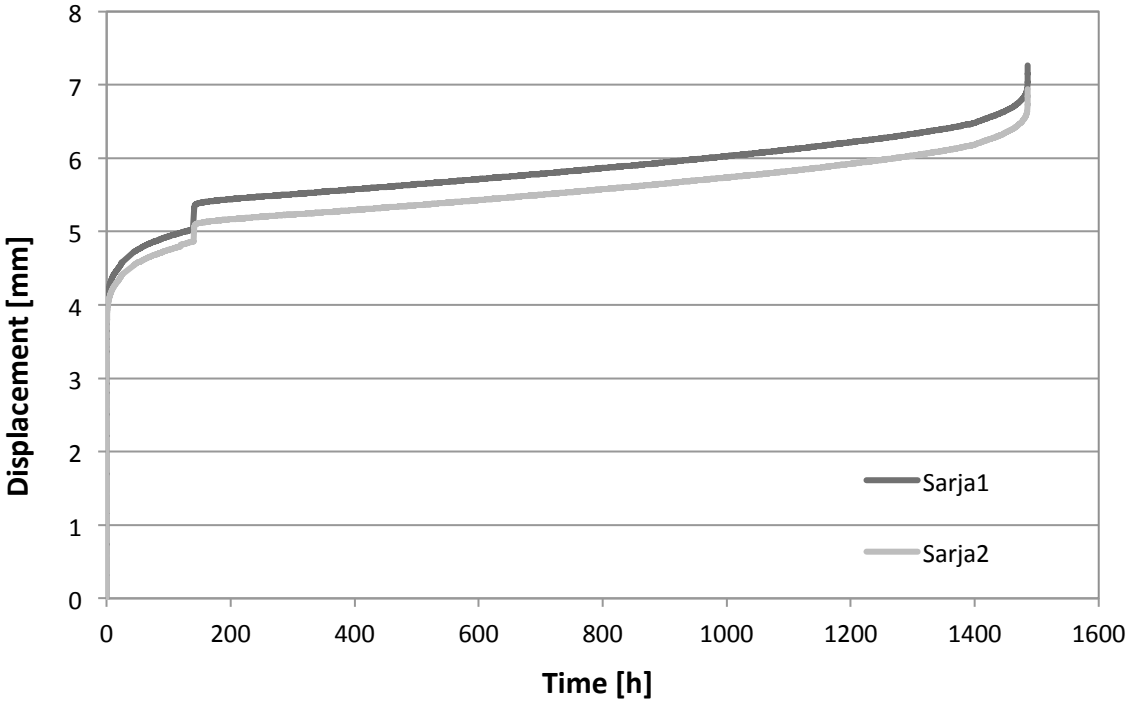

Figure 70.Displacement-time diagram for test y396.

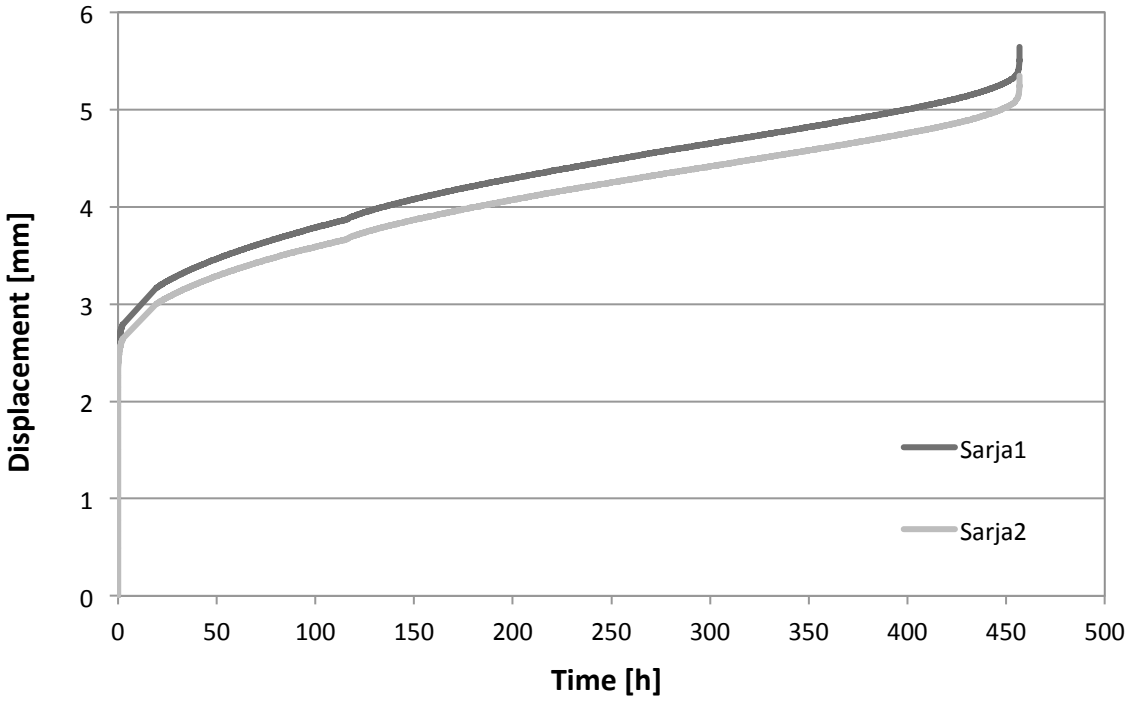

Figure 71.Displacement-time diagram for test y397.

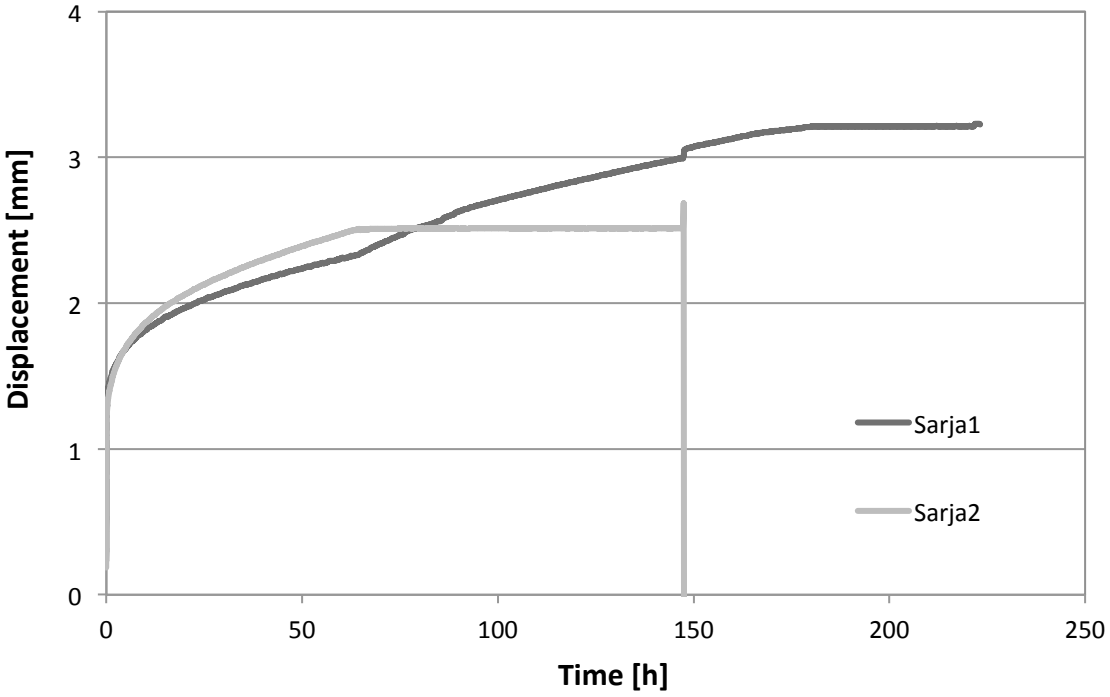

Figure 72.Displacement-time diagram for test y400.

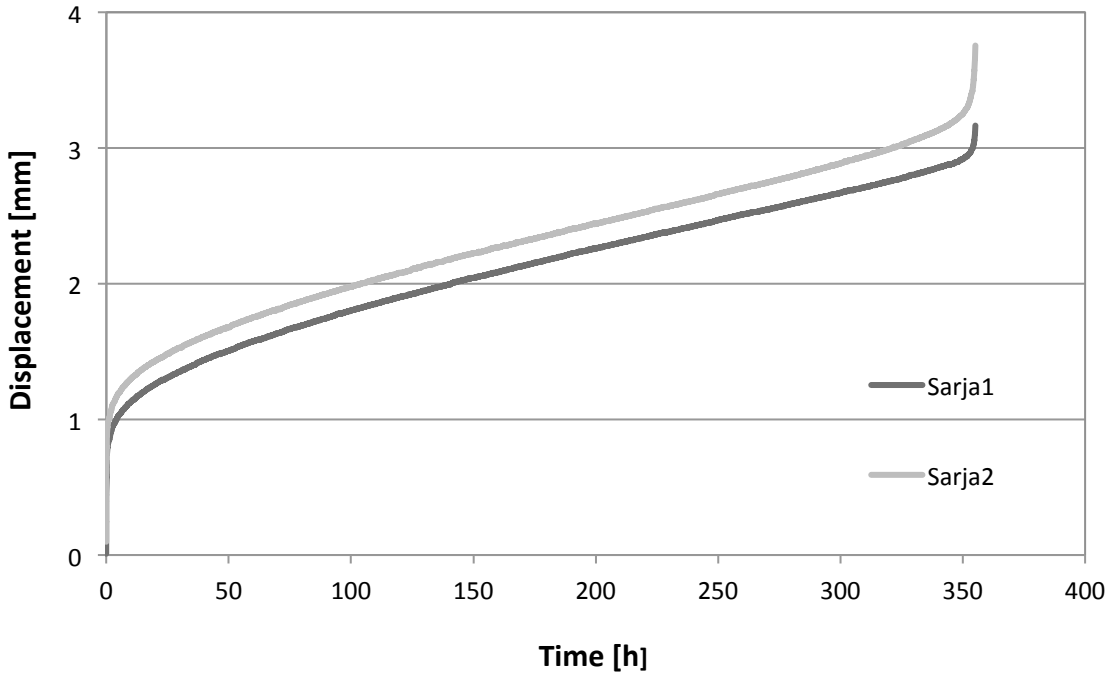

Figure 73.Displacement-time diagram for test y405.

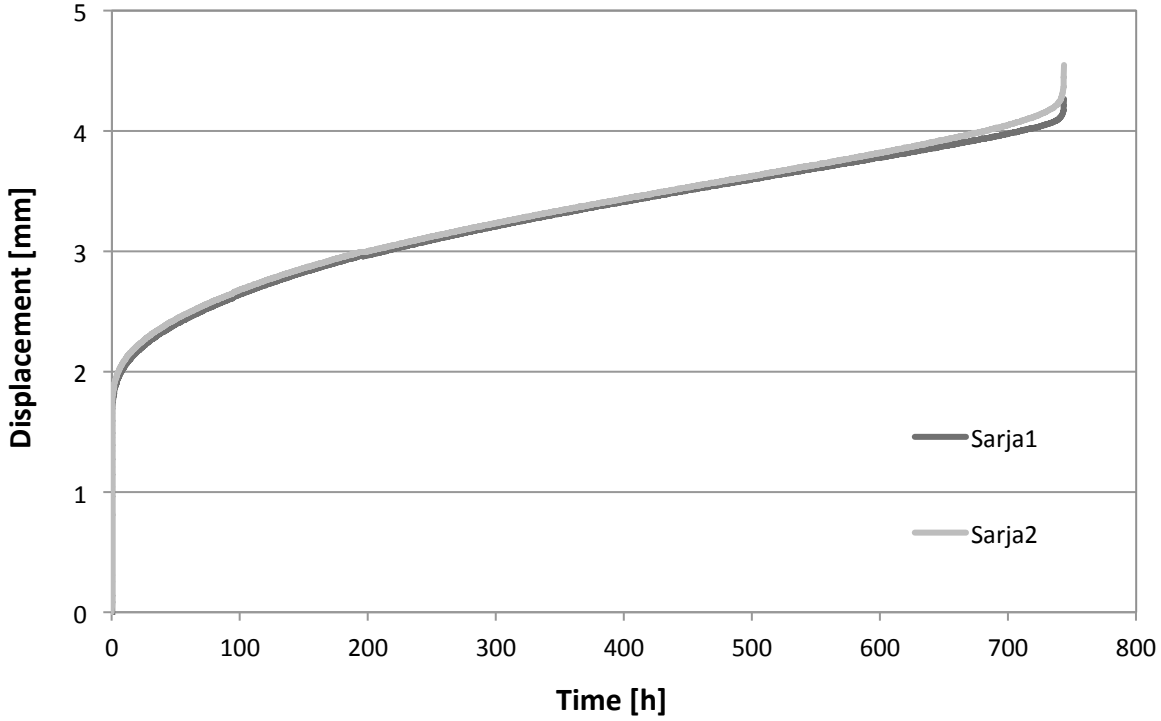

Figure 74.Displacement-time diagram for test y418.

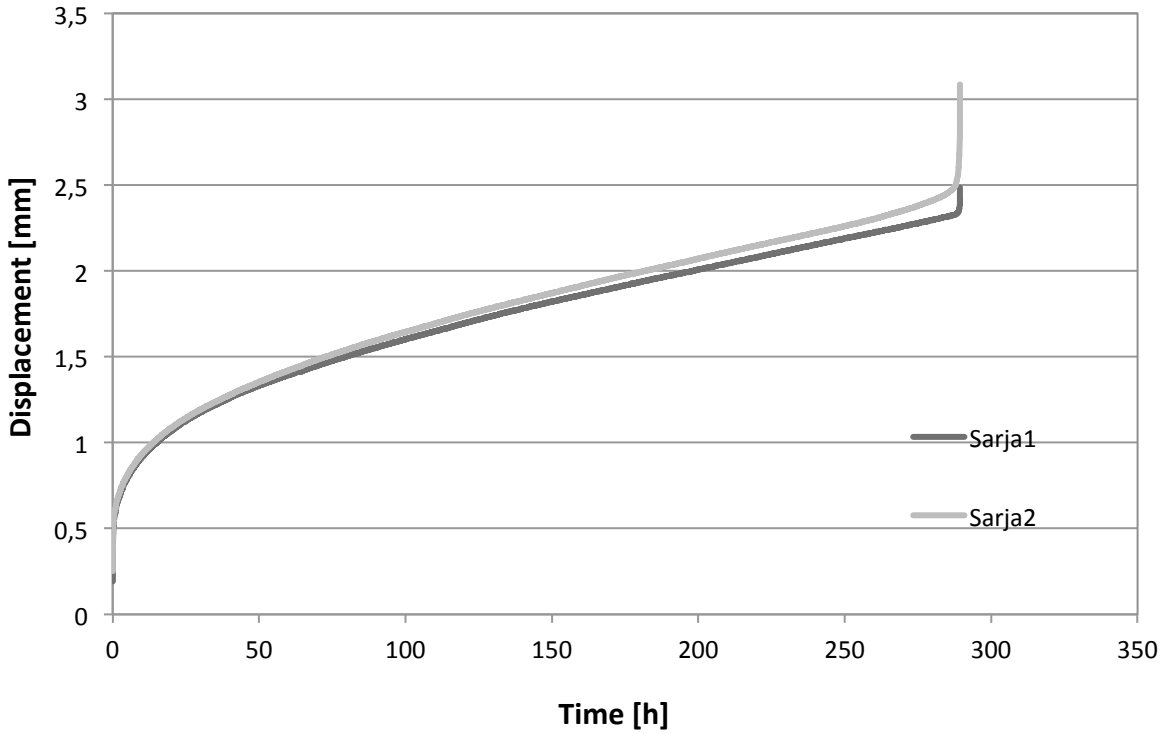

Figure 75.Displacement-time diagram for test y419.

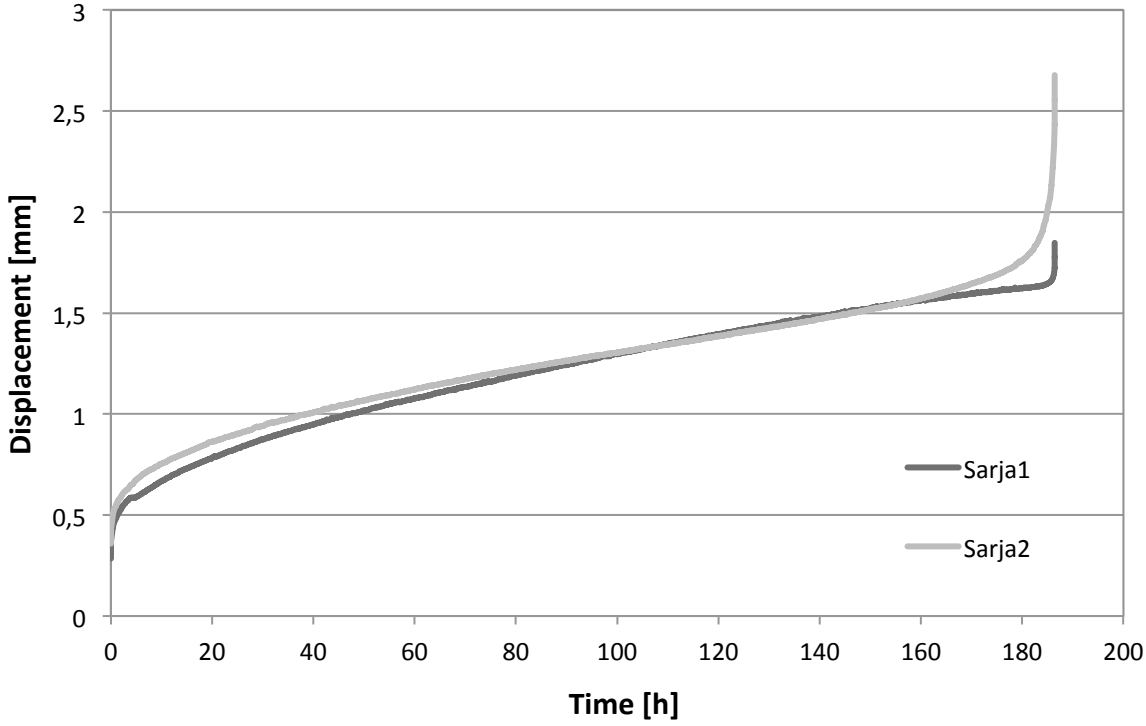

Figure 76.Displacement-time diagram for test y420.

APPENDIX 5

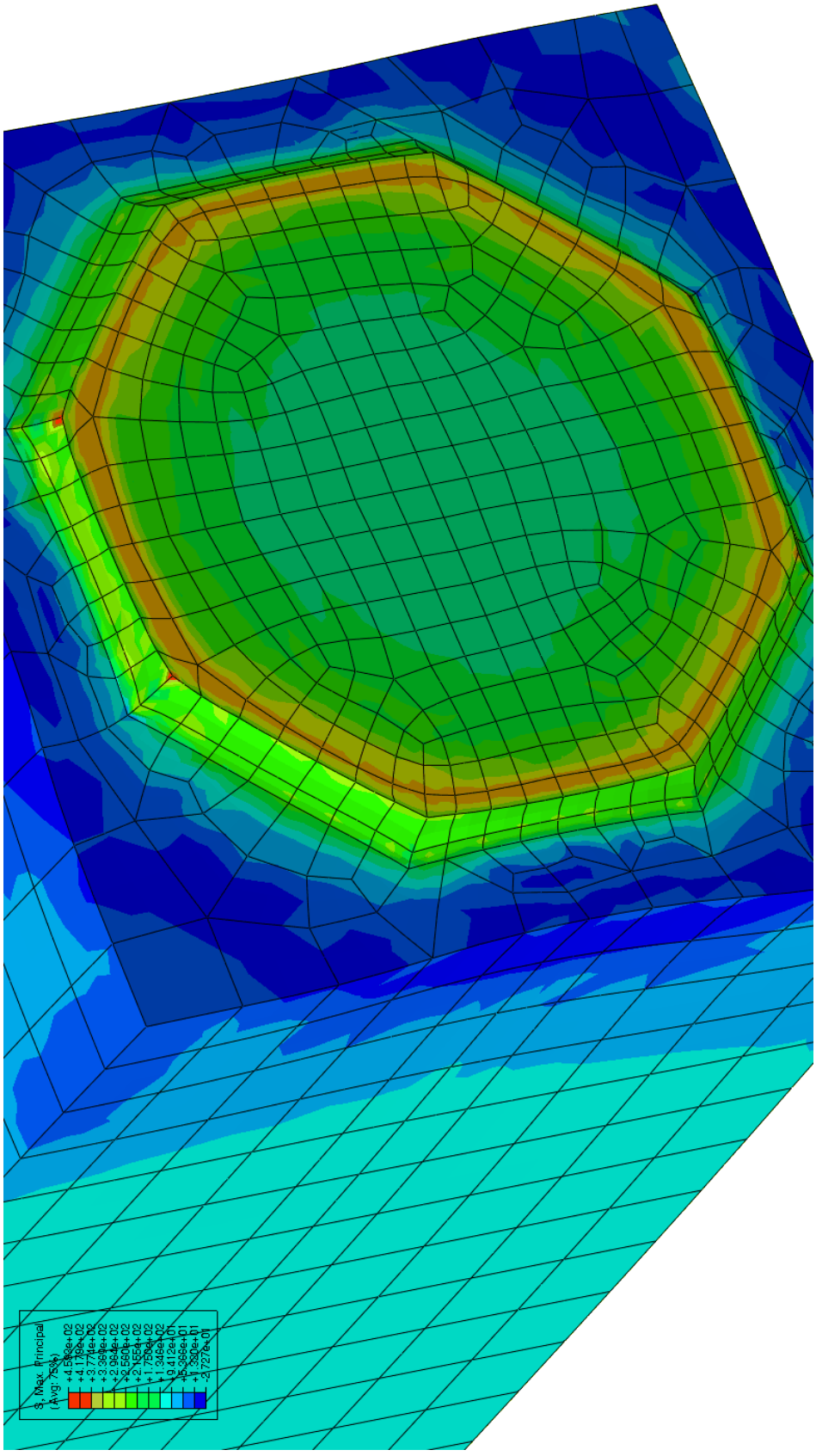

Figure 77. The maximum principal stress distribution for square bar (t=660 h).